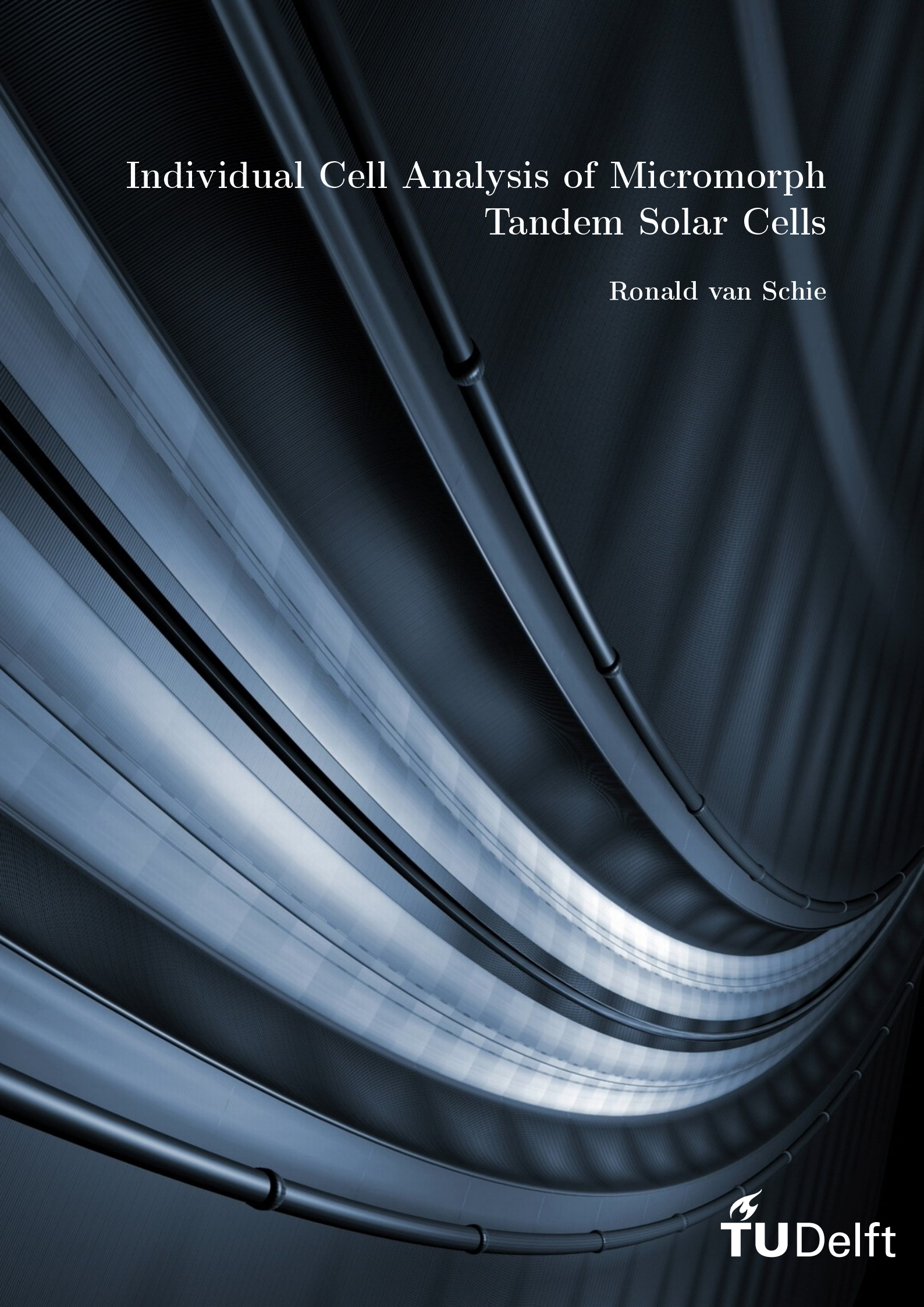

Individual Cell Analysis of Micromorph Tandem Solar Cells

Ronald van Schie

TU Delft

Delft University of Technology

Faculty of Electrical Engineering, Mathematics and Computer Science

Individual Cell Analysis of Micromorph Tandem Solar Cells

in partial fulfilment of the requirements for the degree of

Master of Science
in Sustainable Energy Technology

to be defended publicly on September 16, 2016 at 9:30 AM

Author:
R.S. van Schie

Student Number:
4153766

Master Programme:
SET, Solar Energy

Supervisor:
dr. R.A.C.M.M. van Swaaij

Thesis Committee:
prof. dr. ir A.H.M. Smets
dr. E. van der Kolk
dr. R.A.C.M.M. van Swaaij
F. T. Si, MSc.

TU Delft

PVMD
Delft University of Technology

Preface

The work presented in this report finalises my masters thesis project conducted at the research group Photovoltaic Materials and Devices (PVMD), as a part of the Electrical Sustainable Energy department at the faculty Electrical Engineering, Mathematics and Computer Science at Delft University of Technology. The masters thesis project partially fulfils the requirements for the degree of Master of Science in Sustainable Energy Technology.

I would like to take the opportunity to thank the people involved in my project. First of all I would like to thank my supervisor dr. René van Swaaij. I was very enthusiastic about the research topic he proposed, and although we deviated from the initial plan as the time past, we can be satisfied with the achieved progress and results. Secondly I would like to thank every member of the PVMD group for supporting the master students with their research and make them part of the bigger picture. Specifically I would like to thank Olindo Isabella and Fai Tong Si, for assisting me with optical simulations and the optimisation of several PV active layers that I used in my devices. I fabricated the solar cells for this study under partial supervision and with lots of advise from Fai Tong Si. Furthermore I want to thank Guangtao Yang for explaining me how to prepare microtextured glass and for assisting me with the first batch. This was a critical step, reasoned by prof. dr. ir. Arno Smets, that led to a properly functioning three-terminal solar cell. I would also like to thank the technicians Martijn Tijssen, assisting me with device depositions, Stefaan Heirman that helped me solve problems with the measurement setups and Remko Koornneef, even though not a member of the PVMD group he still found the time to give the dark conductivity setup a software update that made specific measurements possible for me.

I also want to thank Jim Quik, our friendship grew over the last three years from the point where we started the minor on Sustainable Energy Technology and by coincidence carried out our bachelors projects at the same research group. We were both inspired by the opportunities of solar energy and convinced each other to continue our studies with the masters program on Sustainable Energy Technology.

Finally I would like to thank my friends and family that supported me throughout the project and kept me motivated.

Ronald van Schie
September 2, 2016

Abstract

The aim of this study is to analyse the individual cells of a micromorph tandem solar cell by dark current-voltage characteristics and to study the effect of temperature on the individual subcells of the device, being amorphous silicon and microcrystalline silicon. Special focus is placed on studying the temperature-dependent voltage distribution between the subcells. Furthermore, a short study will be performed on the effect of bias voltage on the EQE characterisation of tandem solar cells.

Three-terminal tandem solar cells have been fabricated by sputtering a 200 nm aluminium doped zinc oxide (AZO) layer between the tunnel recombination junction and the bottom subcell through a specially designed mask. The middle AZO contact allows for separate characterisation of the tandem subcells on various measurement setups. Precise dark JV measurements are carried out in a temperature range of 100 °C to 30 °C to reveal the dependency on temperature and find values for ideality factor, dark saturation current and mobility gap for both the individual subcells and the tandem cell.

The mobility energy gap of the three-terminal (3t) a-Si:H top subcell was determined at 1.62 ± 0.02 eV, which is lower than the mobility gap of 1.70 ± 0.01 eV for the single-junction (sj) cell from the same deposition run. It is possible that thermal annealing of the i-a-Si:H layer occurred by the deposition of the middle AZO contact and bottom cell. If hydrogen is effused by thermal annealing of these further process steps, this would increase the defect density of the intrinsic a-Si:H layer, lowering its mobility gap. A similar drop in mobility gap was observed for the 3t µc-Si:H bottom cell, with 1.08 ± 0.01 eV for the 3t bottom subcell and 1.17 ± 0.01 eV for the sj cell from the same deposition run. A slight increase of crystallinity was observed for the 3t bottom subcell with Raman spectroscopy, as compared with the sj µc-Si:H cell. This difference in crystallinity is, however, not significant enough to explain the obtained decrease in mobility gap [51, 59]. The three-terminal tandem cell shows a mobility gap energy of 1.77 ± 0.01 eV, which is close to the mobility gap of the sj a-Si:H cell of 1.70 ± 0.01 eV. However, it is likely that this mobility gap belongs to the tunnel recombination junction, as it was determined in the high forward voltage region where the dark JV curve is suppressed by a non-ideal operation of the TRJ [39].

The temperature-dependent voltage distribution study on the sj dark JV curves revealed that by increasing the temperature, the onset potential for the µc-Si:H subcell decreases, which indicates a higher increase of dark current as a function of temperature for the a-Si:H top cell. Furthermore, it has been demonstrated with light JV measurements that the added series resistance of the middle AZO contact is significantly large. Characterisation methods that involve high current densities will therefore become more complicated when measured through the middle AZO contact. Finally it has been demonstrated that the EQE measurement method for tandem solar cells with bias illumination and bias voltage can not exactly reproduce the true EQE curves of the subcells by applying the V_{oc} of the non-measured subcell.

Nomenclature

Abbreviations

AM	air mass
AC	alternating current
AQE	apparent quantum efficiency
AZO	aluminium doped zinc oxide
DC	direct current
DPC	deposition chamber
E-beam	electron beam
EQE	external quantum efficiency
HF	high frequency
IR	infrared
ITO	indium doped tin oxide
JV	current density - voltage
LLC	load lock chamber
MJ	multi-junction
PECVD	plasma-enhanced chemical vapour deposition
PV	photovoltaic
PVD	physical vapour depostion
QE	quantum efficiency
RF	radio frequency
RIE	reactive ion etching
SCLC	space charge limited current
SE	spectroscopic ellipsometry
SJ	single-junction
SR	spectral response
SRH	Shockley-Read-Hall
STC	standard test conditions
SQ	Shockley-Queisser
TC	transport chamber
TO	transverse optic
TRJ	tunnel recombination junction
UV	ultraviolet
VHF	very high frequency
VIM	variable intensity measurement
ZIT	AZO induced texturing

Physical Constants

c	speed of light in vacuum, $299\,792\,458\,\mathrm{m\,s^{-1}}$
h	Planck constant, $6.626\,069 \times 10^{-34}\,\mathrm{m^2\,kg\,s^{-1}}$
k_B	Boltzmann constant, $1.380\,649 \times 10^{-23}\,\mathrm{J\,K^{-1}}$
q	elementary charge, $1.602\,18 \times 10^{-19}\,\mathrm{C}$
σ	Stefan-Boltzmann constant, $5.670\,367 \times 10^{-8}\,\mathrm{W\,m^{-2}\,K^{-4}}$

Latin symbols

A	area, $\mathrm{m^2}$
A	absorptance, -
D	diffusion coefficient, $\mathrm{m^2\,s^{-1}}$
E	energy, J
FF	fill factor, -
I	current, A
I	intensity, -
i	intrinsic concentration, $\mathrm{m^{-3}}$
J	current density, $\mathrm{A\,m^{-2}}$
L	diffusion length, m
m	mass, kg
m	ideality factor, -
$m*$	effective mass, kg
N	particle density, $\mathrm{m^{-3}}$
n	electron concentration, $\mathrm{m^{-3}}$
P	power, W
p	hole concentration, $\mathrm{m^{-3}}$
R	recombination rate, $\mathrm{m^{-3}\,s^{-1}}$
R	resistance, Ω
R	reflectance, -
T	temperature, K
T	transmittance, -
t	thickness, m
V	electric potential, V
v	velocity, $\mathrm{m\,s^{-1}}$
W	space charge region width, m

Greek symbols

γ	Raman scattering cross-section of c-Si TO mode to a-Si TO mode, -
η	efficiency, -
θ	angle, rad
λ	wavelength, m
μ	mobility, $\mathrm{m^2\,V^{-1}\,s^{-1}}$
λ	wavelength, m
σ	capture cross-section, $\mathrm{m^2}$
σ	conductivity, $\mathrm{S\,m^{-1}}$
ϕ	work function, V
ω	angular frequency, $\mathrm{rad\,s^{-1}}$

Subscripts

0	dark saturation	ph	photogenerated
a	activation	R	recombination
C	conduction band	rec	recombination
D	donor	ref	reference
D	dark	σ	capture cross-section
E	exponential	s	series
e	electron	SC	space charge
F	Fermi	sc	short-circuit
f	quasi Fermi	sig	signal
G	bandgap	sh	shunt
gen	generation	TO	transverse optic
h	hole	t	trapped
i	intrinsic	th	thermal
in	incident	V	valence band
lock	lock-in amplifier	vac	vacuum
μ	mobility		
max	maximum		
mob	mobility		
mpp	maximum power point		
oc	open-circuit		
out	output		

Table of Contents

1 | Introduction

The closest and by far largest energy source in the Earth's proximity is the Sun. Increasing the collection of solar energy is a straightforward approach to release ourselves from the current carbon locked-in economy. A large contribution to sustainable energy could potentially be delivered with direct conversion of solar irradiance to electricity by use of the photovoltaic effect. There are many different technologies available for this application, such as silicon wafer based, thin-film, multi-junction or organic solar cells. The most important advantage of multi-junction solar cells is the potentially higher conversion efficiency through stacking of different absorber layers in series. This leads to a better spectral utilisation, since each of the layers is designed to absorb a specific part of the solar spectrum. In this way thermalisation losses can be reduced. Thin-film silicon, such as amorphous- and microcrystalline silicon, is quite often adopted in many different compositions and alloys to achieve this.

This introductory chapter will start with a motivation for doing research in photovoltaics, followed by a discussion of the basic properties of solar radiation that reaches the Earth and how it can be converted directly to electrical energy. Thin-film amorphous- and microcrystalline silicon materials will be discussed, followed by the concept of multi-junction solar cells and their cell structure. Finally, the outline of this thesis will be presented.

1.1 Motivation: Repairing the way of Life

Saving the environment has been a hot topic since the end of the 20th century. Human activity will have to change dramatically this century in order to create a global sustainable way of living. Reducing the use of fossil fuel resources and increasing the number of recyclable products are key aspects to reach this goal. It implies that alternative energy sources need to be employed more intensively.

Climate negotiation in 2015 led to the Paris Agreement [1], which aims to limit the increase of the average global temperature to below 2 °C. The focus is on development with low greenhouse gas emissions by mainly the developing countries. The concept of leapfrogging is applicable here, which means that developing countries can skip more polluting development steps and directly implement highly sustainable technologies. Furthermore the agreement encourages large-scale investments in sustainable development by the industrialised countries. In contrast, institutions and individuals started to divest in companies involved in the fossil fuel industry, such as coal, oil and natural gas extractors. Based on the reserves and resources that these companies claim to have, burning all of it would by far exceed the 2 °C temperature increase limit of the agreement. Removing investments in these companies might force them to adapt their policy and start investing in renewable energy sources.

When we look at the alternatives to fossil fuels, there are not many options to choose from. Most of the renewable energy technologies originate from solar energy, being transformed to other forms. Temperature differences on earth are the driving force for wind flows, biomass is formed by plants or small organisms under illumination of the sun and

a part of hydropower originates from potential energy of water being brought to higher ground by evaporation.

Figure 1.1 shows a graphical representation of the annual energy potential that renewable sources have, compared to the annual energy demand in 2006. It also includes the estimated global reserves of the predominantly used fossil fuels: coal, natural gas and crude oil.

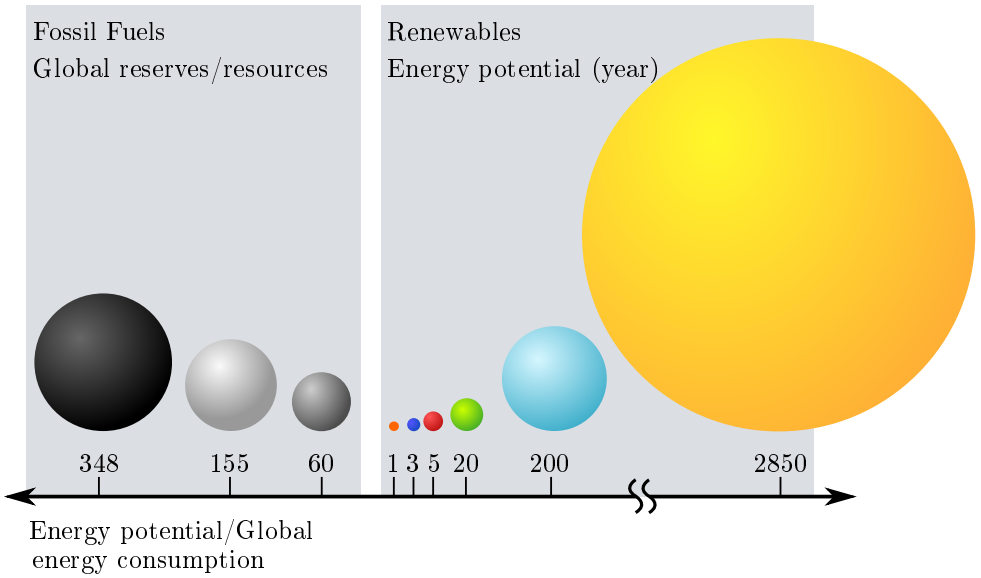

	Global reserves
Coal	~135 000 EJ
Natural gas	~60 400 EJ
Crude oil	~23 000 EJ
Global demand 2006	~470 EJ

	Energy potential
Solar radiation	~1 111 500 EJ
Wind energy	~78 000 EJ
Biomass	~7800 EJ
Geothermal	~1950 EJ
Hydro/tide power	~1170 EJ

Figure 1.1: Global annual potential of available renewables and total reserves of fossil fuels, scaled to the global energy demand in 2006. Adapted from [2].

Even when the global energy demand keeps increasing at the current rate, solar energy on its own could provide us with enough energy for decades. 'Potential', however, means that we must act quickly and adequately to improve the way of extracting energy from the sun. It is estimated that the amount of extractable solar energy with current state of the art technologies is ~1482 EJ, which is only 0.13% of the energy potential [2].

Apart from efficiently extracting energy, research is required to improve storage. Especially wind and solar energy are not continuously present due to weather conditions. Thus the ultimate goal is to combine a mix of different renewables and highly efficient storage to meet the energy demand of the future, releasing the lock of our current carbon system.

1.2 Solar energy

We on planet Earth are very lucky to have our own star at a relatively small distance. A distance perfect enough to support the creation and evolution of life under optimal conditions. The Sun was formed more than 4.5 billion years ago, pulling enormous amounts of mass to its centre. The total mass of this yellow dwarf is approximately 333.000 times that of the Earth, which creates a large gravitation towards its core. High pressure and temperature lead to nuclear fusion of hydrogen atoms to form helium, which releases a huge amount of energy by the mass defect of the fusion reaction. The helium product has a smaller mass than the 4 protons that collided together to form it. Following Einstein's special relativity mass-energy equivalent, $E = mc^2$, it can be calculated that the loss of mass from one reaction is converted to approximately 27 MeV. Together with the fact that the Sun converts 600 million tons of hydrogen each second [3], it is evident that the Sun produces an enormous amount of energy.

A large part of this solar energy is released in the form of radiation from the surface. The average surface temperature of the Sun is 5780 K, which translates to the blackbody radiation spectrum calculated with Planck's Law in figure 1.2. Using the Stefan-Boltzmann law to calculate the power radiated from a black body, $P = \sigma T^4$, and multiplying this value with the surface area of the Sun, one finds a power of $3.9 \times 10^{26}\,\mathrm{W\,m^{-2}}$. Since the Earth only intercepts a small fraction of this power at the orbits distance away from the Sun, we on average receive $1361\,\mathrm{W\,m^{-2}}$ at the top of our atmosphere.

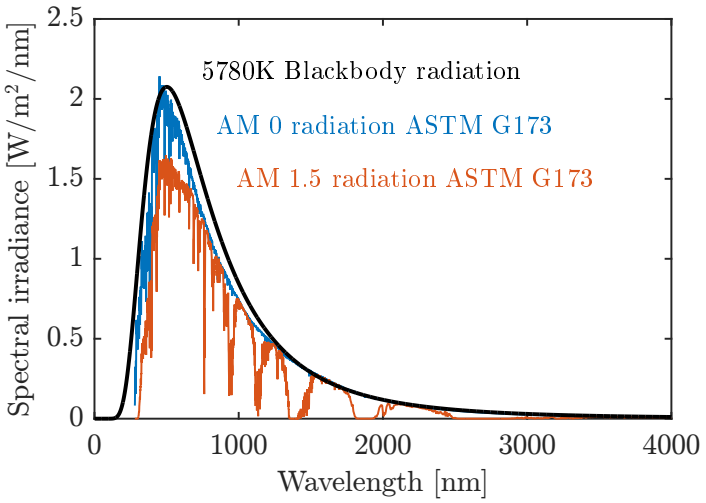

Figure 1.2: Spectral irradiance of a blackbody at 5780 K together with the ASTM G173 extraterrestrial AM 0 and Global tilt AM 1.5 spectra. Spectrum data retrieved from [4].

Before sunlight reaches the Earth's surface, it travels through the atmosphere, where it will be partially absorbed and scattered by gas molecules. The longer it travels through the atmosphere, the higher the attenuation will be. The Air Mass coefficient gives the ratio between the optical path length through the atmosphere and the vertical path length at the zenith. Air Mass zero (AM 0) refers to the spectral irradiance just outside the atmosphere and AM 1.5 refers to a path length 1.5 times the vertical thickness of the atmosphere. This corresponds to light hitting the Earth's surface at a zenith angle of

48.2°. The AM 1.5 spectrum is used as a reference for terrestrial solar cell characterisation and is one of the three conditions to meet standard test conditions (STC). The other two being a total intensity of $1000\,\mathrm{W\,m^{-2}}$ and a solar cell temperature of 25 °C. The AM 1.5 spectrum defines the photon flux density, which is the number of photons or intensity at every wavelength, by dividing with the photon energy $E = hc/\lambda$.

1.2.1 Semiconductors and electronic bands

All crystalline materials are classified in three groups; metals, insulators and semiconductors. This classification is based on the electrical conductivity of a material, which is a measure for the number of free charge carriers and their mobility. For a detailed description on semiconductors and the derivation of relevant physics, the reader is referred to literature on solid state physics [5].

When atoms are brought together in a crystal structure, so called bonding and antibonding energy states are formed. From the many atoms in a material together, these states form two distinct energy levels which are called valence band and conduction band. Electrons will preferably occupy the lowest energy state in the material, this is in the valence band where the electrons are bound to atoms and therefore being immobile. Electrons in the higher energy conduction band are mobile and will act as charge carrier. In metals the valence band and conduction band are overlapping, which means that the electrons in the valence band can easily be excited to the conduction band. The electrical conductivity of metals is therefore higher than other materials, since there are many free charge carriers. The valence and conduction band can also be slightly apart, creating an energy difference between the bands that is called the bandgap. The bandgap of an insulating material is too large for electrons to be excited from valence to conduction band. This results in very few or even zero electrons in the conduction band which means poor electrical conductivity. Between metals and insulators there is a group of materials where the bandgap energy is small enough such that an electron can be excited to the conduction band by thermal energy or photon energy. These materials are called semiconductors and have a bandgap of around 1 eV, which is much higher than room temperature thermal energy of $E = k_B T \approx 0.026\,\mathrm{eV}$. This implies that it will only be electrical conductive with increased temperature or under illumination.

The conductivity of a semiconductor material can be influenced by doping, i.e. the incorporation of other element atoms with a different number of valence electrons in a pure semiconductor material. In crystalline silicon, which has 4 valence electrons per atom, doping can either be achieved by including atoms with 3 valence electrons (e.g. Boron) or by atoms with 5 valence electrons (e.g. Phosphorus). The thermal energy in the lattice at room temperature is high enough to ionise the doping atoms, i.e. the doping atom will either *accept* the missing electron from surrounding silicon atoms or it will *donate* the excess electron to the lattice. Acceptor type atoms with less valence electrons per atom than the host material will increase the concentration of free holes in the semiconductor. The doping atoms will be negatively charged after ionisation and the electrical conductivity is dominated by holes, which is called a p-type semiconductor. Donor type atoms with more valence electrons per atom than the host material will increase the concentration of free electrons in the semiconductor. The doping atoms will be positively charged after ionisation and the electrical conductivity is dominated by electrons, which is called a n-type semiconductor.

Doping changes the Fermi level of the semiconductor material, which is a measure for the chemical potential of electrons in a system. The position of the Fermi level in a semiconductor material depends on temperature, the effective mass of electrons and holes and their number densities [5]. In an intrinsic material at 0 K every electron will be in the valence band, placing the Fermi level exactly in the middle of the bandgap. This is the energy level where the probability on being occupied by an electron is 50%. However, at elevated temperature or when the number of free charge carriers in the system is adapted, the distribution of electrons between valence and conduction band will change according to the Fermi-Dirac distribution and the density of states for both valence and conduction band. By increasing the number of free holes in the material (p-type doping), the position of the Fermi level will move towards the valence band. On the other hand when the number of free electrons is increased (n-type doping), the position of the Fermi level will move towards the conduction band. This is graphically shown in figure 1.3 (a).

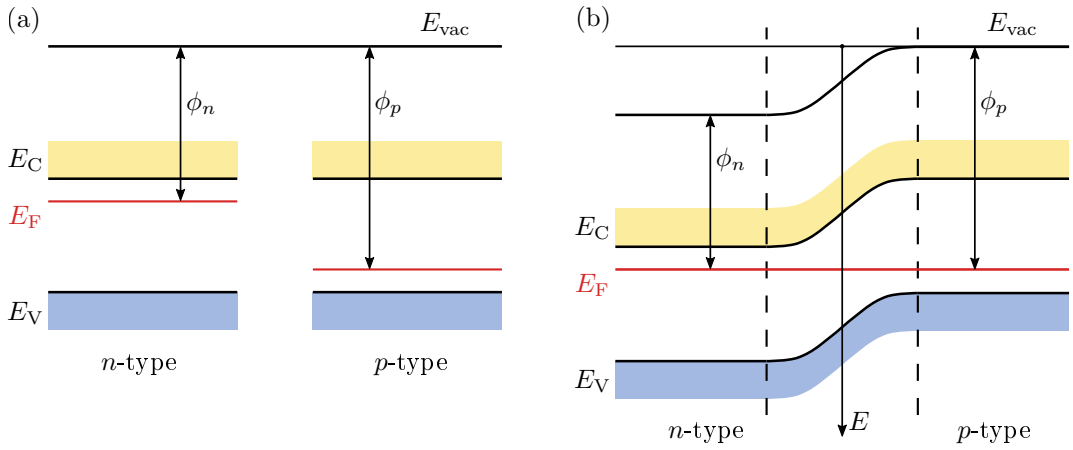

Figure 1.3: (a) Energy band diagrams of n-type and p-type doped semiconductor material including Fermi energy and work functions. (b) p-n junction band diagram under equilibrium. Adapted from [6].

Figure 1.3 includes the vacuum level, E_{vac}, which is the energy level where an electron is free of influence of the atom, and the work functions of both p- and n-type semiconductors, ϕ_p and ϕ_n. The work function is defined as the potential difference between the vacuum level and the Fermi energy and therefore changes with doping type. When a p-n junction is formed between two semiconductors with equal bandgap, the vacuum level and conduction and valence band energies are continuous. This means that through the difference in work function of the p- and n-type materials the bands are bent, indicating the formation of an electric field. The majority charge carriers in both materials will recombine through diffusion, leaving behind the ionised dopants. A drift current induced by the internal electric field opposes the diffusion current and this leads to the formation of a depletion layer, demarcated by the dashed lines in figure 1.3 (b). This is what makes the p-n junction such a valuable structure: charge transport through the depletion layer can be influenced by doping concentrations and by applying a voltage across the junction.

1.2.2 Photovoltaic effect

Solar cell technology is based on a principle where light is directly converted to electrical energy, which is called the photovoltaic effect. This effect was first discovered by Edmond Becquerel in 1839 [7]. It describes the interaction of electromagnetic radiation with materials, where it creates an internal voltage or electric current. This phenomenon is observed in semiconductor materials due to their electronic band structure.

The photovoltaic effect is best explained in three steps, namely absorption of photons, separation of charge carriers and collection of charge carriers. Absorption of light occurs when photons have a higher energy than the bandgap. One photon can promote one electron to the conduction band, simultaneously leaving a hole in the valence band. Separation of the electron-hole pair is required, otherwise the electron would simply fall back to the valence band and release the absorbed energy. Since the electron and hole are of opposite charge, an internal electric field can move the charge carriers in opposing directions. This is achieved with doping as explained in the previous paragraph. When n- and p-type materials are brought into contact, a depletion region is formed by diffusion and recombination of charge carriers. Electrons diffuse into the p-type material, where they recombine with holes and vice versa. The region surrounding the junction is depleted from free charge carriers and this leaves behind the donor and acceptor ions of opposite charge, creating an internal electric field. Figure 1.4 shows a schematic of the equilibrium state, where there is no further diffusion of charge carriers due to the internal electric field barrier.

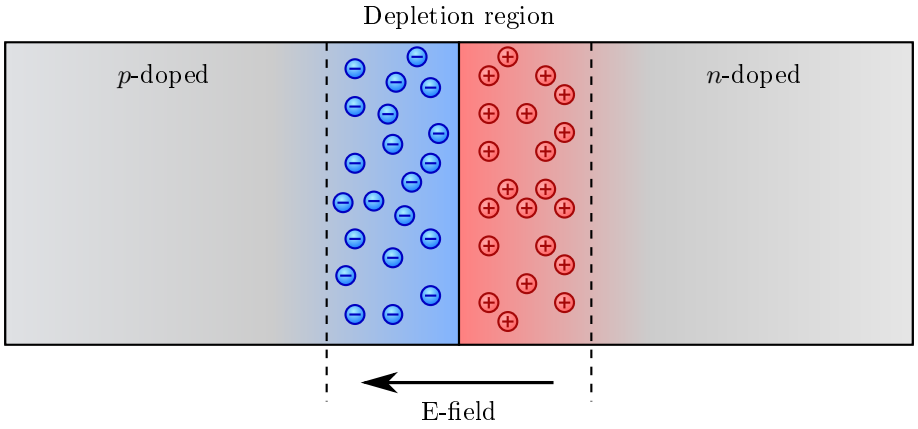

Figure 1.4: P- and n-type doped material forming a p-n junction. Diffusion of charge carriers forms a depletion region. Negatively charged ions (blue) and positively charged ions (red) in the depletion layer create an electric field that opposes the diffusion direction.

Separation of charge carriers generated on either side of the depletion region is driven by diffusion of the minority charge carriers (electrons in p-type and holes in n-type material) towards the depletion region, where they drift to the other side and become majority charge carriers that diffuse further to the contact. Collection of charge carriers is achieved by making contacts of conducting materials such as metals and metal oxides. A potential difference between the two contacts is present, since the electrons are collected at a higher energy state than the valence band. Connecting a load to the contacts closes the electronic circuit and enables to draw power from the solar cell.

1.2.3 Shockley-Queisser limit

William Shockley and Hans Queisser have made their calculation on the maximum theoretical efficiency of a single-junction solar cell back in 1961 [8]. They considered four different loss mechanisms, adding up to an efficiency limit formed by basic physics. The first is related to recombination, since there is always a chance that a formed electron-hole pair recombines and loses its energy. Recombination can be caused by defects in the material (Shockley-Read-Hall), but it can also occur spontaneously via band-to-band recombination under emission of a photon with an energy equal to the bandgap (radiative). A third option is that the energy of recombination is transferred to another electron in the conduction band, which is excited further into the band and relaxes back thermally to the conduction band edge under emission of a photon (Auger). Recombination limits the open-circuit voltage of a p-n junction and consequently the possible amount of energy extracted from each absorbed photon. The Shockley-Queisser (SQ) limit only includes radiative recombination, since this form is present in every solar cell. The second loss mechanism is Black-body radiation, since any device operating at a temperature higher than 0 K emits electromagnetic radiation.

The third and fourth loss mechanism are related to the solar spectrum and the bandgap of the photovoltaic material, together referred to as "spectral mismatch". A single photon carries a fixed amount of energy which depends on the wavelength as in $E = hc/\lambda$. The bandgap of a semiconductor material determines whether a photon can be absorbed or not. If the energy of the photon exceeds the bandgap energy, it might be absorbed by exciting an electron from the valence band to the conduction band. When the photon energy is not sufficient to excite an electron, it will not be absorbed. Absorbed photons can also have excess energy, which will result in thermal relaxation of the excited electron to the conduction band edge. Thermalisation losses and non-absorption losses are visualised in figure 1.5.

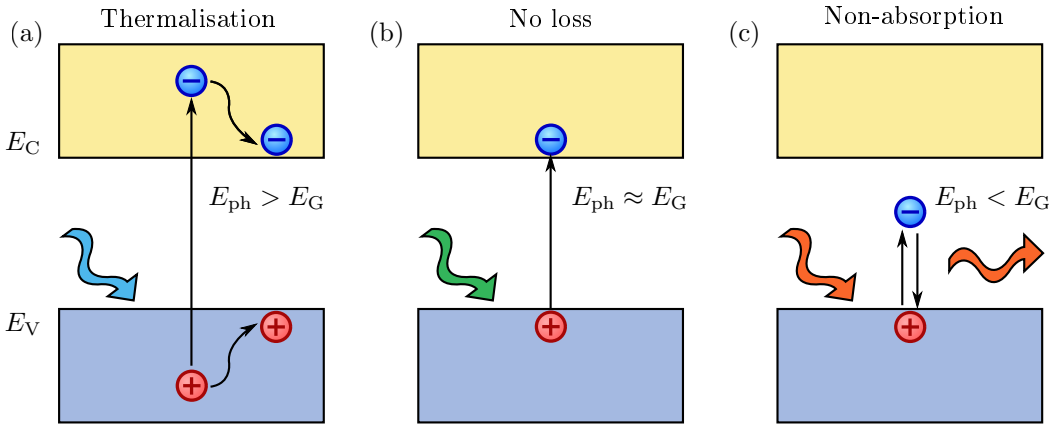

Figure 1.5: (a) Thermalisation loss by excess photon energy. (b) No loss if photon energy equals bandgap energy. (c) Non-absorption loss if photon energy is smaller than bandgap energy.

The SQ limit thus gives the theoretical maximum conversion efficiency of a single-junction solar cell, depending on the bandgap energy of the absorber material. Figure 1.6 shows the SQ limit along with the bandgap energy of several commonly used absorber materials, showing that both crystalline silicon (c-Si) and cadmium tellurium (CdTe)

based solar cells could theoretically lead to a high efficient single-junction device. The optimum bandgap of a single-junction solar cell for AM1.5 irradiation is calculated to be approximately 1.34 eV, with a conversion efficiency of 33.7% [9]. The optimum at the c-Si bandgap of 1.12 eV corresponds to a maximum theoretical conversion efficiency of 32%. Photons with an energy equal to this bandgap of c-Si correspond to a wavelength of approximately 1100 nm. Longer wavelength photons will not be absorbed, where shorter wavelength photons will have excess energy which leads to thermalisation.

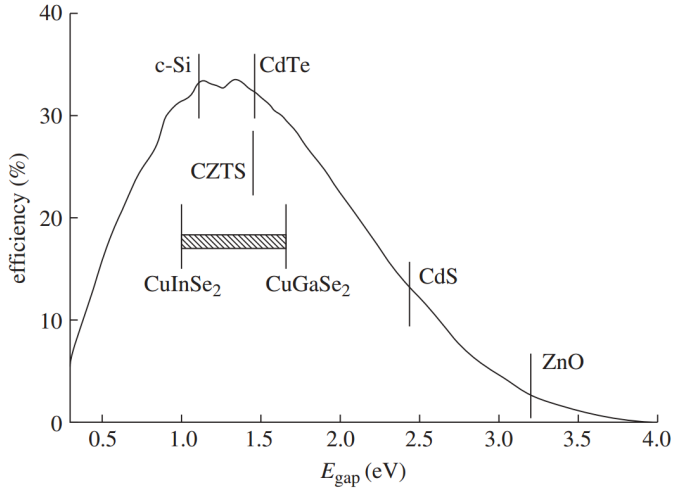

Figure 1.6: Shockley-Queisser limit for single-junction solar cells under AM1.5 illumination, bandgap energies for commonly used absorber materials are included. Figure from [9].

1.3 Thin-film silicon

Thin-film silicon technology is a part of the second generation solar cell technologies, which offers a wider applicability of solar cells. For instance, low process temperatures allow the use of plastic substrates to obtain flexible light-weight solar modules with for instance the Helianthos process [10]. Secondly the higher open-circuit voltage of a-Si:H is widely studied for the direct production of solar fuels [11]. In comparison with first generation silicon wafers, thin-film cells are more than 100 times thinner. In order to absorb enough light in such a thin layer, advanced light trapping methods have to be applied.

This part of the introduction will describe the basic principles and operation of thin-film amorphous silicon (a-Si:H) and microcrystalline silicon (µc-Si:H) solar cells, starting with the properties of the materials itself. Furthermore this section will discuss the concept of multi-junction solar cells and show some examples of basic device structures.

1.3.1 Amorphous silicon

An amorphous material is characterised by being solid without having a long range order, this is the opposite of a perfect monocrystalline structure. Amorphous silicon (a-Si:H) is a random growth structure of silicon atoms, which does not have the perfect tetrahedral crystal structure with bond angles of 109.5° that crystalline silicon has. Instead

the bond angles of each atom have a standard deviation between 6° and 9° from the tetrahedral structure and also the bond lengths will vary around 0.235 nm [12]. Short-range order is present, i.e. the neighbouring atoms are located closely to the tetrahedral crystal structure, but long-range order is disturbed by the deviation in bond angles and bond lengths. Multiple types of defects will be present by missing bonds between silicon atoms, which are called 'dangling bonds', by voids in the lattice and by so called divancancies, which is a missing pair of silicon atoms [13]. Hydrogen is mostly used to passivate the broken bonds in amorphous silicon, being denoted as a-Si:H. Up to 99% of the dangling bonds can be passivated [12], which decreases the defect density of the material. Figure 1.7 shows a schematic representation of the 2D lattice structures of monocrystalline silicon, hydrogenated microcrystalline and amorphous silicon.

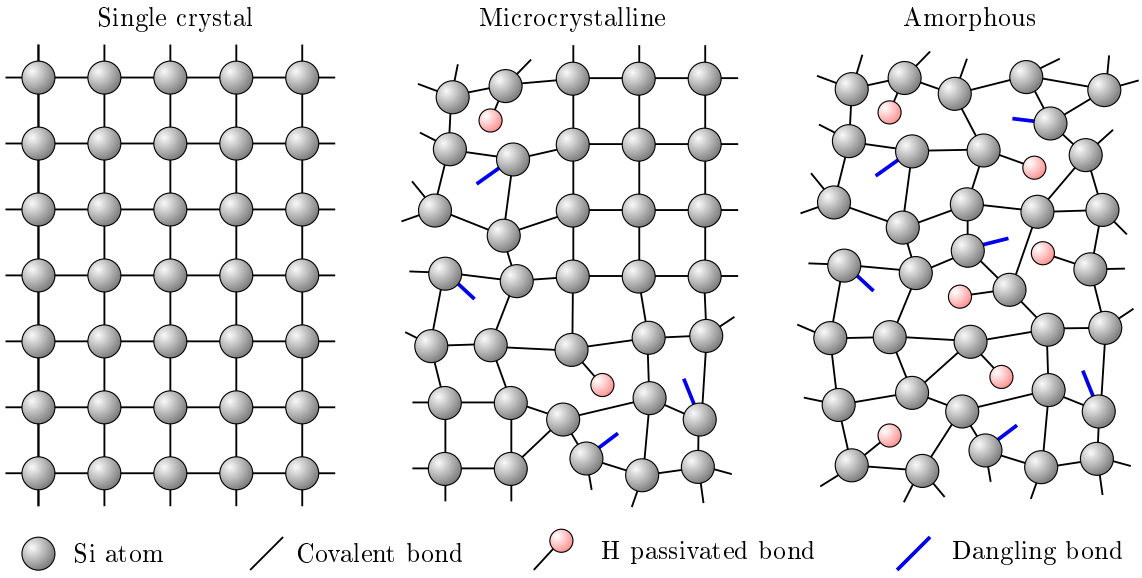

Figure 1.7: Schematic representation of the 2D lattice structures of monocrystalline silicon, hydrogenated microcrystalline silicon and hydrogenated amorphous silicon.

Since the material is defect rich, the diffusion length for both charge carriers is very short and the mobility of the material is low. The density-of-states distribution, which is defined as the volumetric number of states that can be occupied by electrons at every energy level, is affected by the defect rich lattice structure of a-Si:H. While crystalline silicon has a very low defect density and a long range ordered lattice structure, there are no energy states between the conduction and valence band, clearly defining the bandgap of the material. For a-Si:H, the lack of long range order gives rise to band tails extending into the bandgap of the material. Defects such as dangling bonds introduce defect states in the bandgap, extending over the whole range from valence band to conduction band tails. The density of states distribution for both crystalline and amorphous silicon are shown in figure 1.8.

As denoted in figure 1.8, the energy states within the valence and conduction band are called extended states, being present by electron and hole wavefunctions extending over the entire atomic structure [14]. On the other hand, localised states are formed by wavefunctions of tail and defect states. Electrons in localised states are trapped, meaning that the mobility of these charge carriers is strongly reduced. The term mobility gap, E_{mob}, is introduced to define the bandgap of a-Si:H. It defines the energy gap with

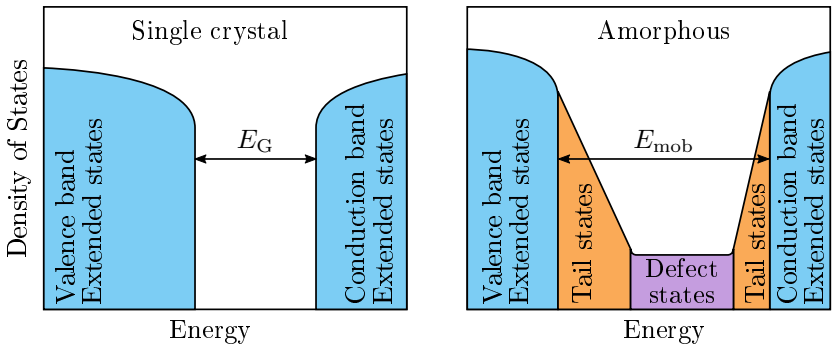

Figure 1.8: Schematic representation of density of states distribution of monocrystalline silicon and hydrogenated amorphous silicon, adapted from [14].

reduced mobility of charge carriers. Usually, a value of 1.8 eV is reported for the mobility gap of a-Si:H, a lower value of 1.69 eV has been reported by Kind *et al.* [15]. Sturiale and Rubinelli [16] demonstrated that the mobility gap of a-Si:H *p-i-n* cells varies with the hydrogen dilution ratio ($[H_2]/[SiH_4]$).

Charge transport must be achieved by applying an electric field such that the carriers are separated and transported by the mechanism of drift. A structure that is commonly used to induce this electric field is by placing an intrinsic (undoped) absorber layer between a layer of *n*-type and a layer of *p*-type material. The difference in work function induces this internal electric field as described in section (1.2.1). The *n*- and *p*-type layers will collect the electrons and holes respectively on either side of the intrinsic absorber material. In common device structures, light will enter from the *p*-side of the cell, receiving the name *p-i-n* device. A simulated band diagram of a typical a-Si:H solar cell is presented in figure 1.9. Band bending at the p/i and i/n interface is caused by positively charged donor-like states at the *p-i* interface and negatively charged acceptor-like states at the *i-n* interface.

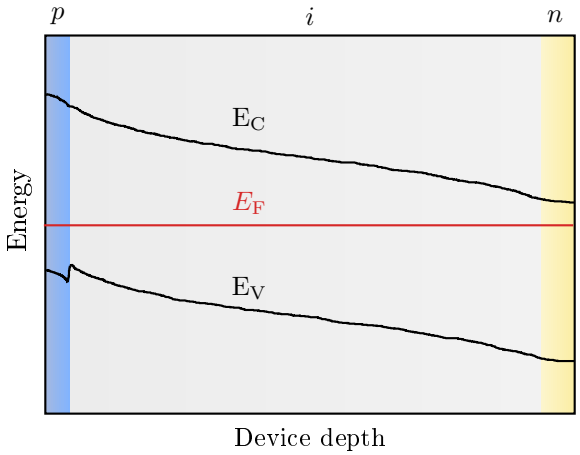

Figure 1.9: A band diagram simulation of a single-junction amorphous silicon *p-i-n* solar cell.

Light will enter from the *p*-side of the device, but light absorption in this layer will not contribute much to the total current generation of the cell. This *p*-layer thus needs to have a wide bandgap, such that it is as transparent as possible. A wider bandgap is achieved by introducing oxygen atoms (a-Si_xO_{1-x}:H) or carbon atoms (a-Si_xC_{1-x}:H), which is then

called a window layer [17]. The wider bandgap of the p-layer is included in figure 1.9.

Finally, a-Si:H cells suffer from light induced degradation, referred to as the Staebler-Wronski effect [18]. Under influence of light the bonds between hydrogen and silicon atoms can be broken, resulting in an increased dangling bond density. Especially thick a-Si:H cells suffer from this type of performance degradation. There will be a trade-off between improving the absorption of the a-Si:H cell by using a thicker intrinsic layer and the level of performance degradation [12].

1.3.2 Microcrystalline silicon

Similar to amorphous silicon, microcrystalline silicon (µc-Si:H) is a growth structure of silicon atoms, but, depending on the deposition parameters, crystalline silicon grains will be formed in the amorphous material. The first working solar cell based on µc-Si:H was demonstrated by Meier et al. [19]. An advantage of µc-Si:H is that the material is not vulnerable to light-induced degradation, as is the case with a-Si:H. On the other hand it is more difficult to deposit, which is why stable results could only be published after improvements to deposition techniques, such as plasma-enhanced chemical vapour deposition [20].

Deposition parameters that are tuned to start the formation of silicon crystals are plasma power, chamber pressure and most important the hydrogen to silane (SiH_4) gas flow ratio. If the silane gas is diluted with hydrogen, c-Si cones will form in the amorphous matrix. Deposition of the intrinsic layer is preceded by an incubation layer at a lower hydrogen dilution level to initiate the formation of these cones [20].

A new source of defects compared to a-Si:H originates from grain boundaries where c-Si cones touch. Additionally, such grain boundaries are formed when the material is deposited on textured substrates [21]. The material thus still has too many defects, although being hydrogenated, and is therefore fabricated in a p-i-n structure. Similar to amorphous silicon, the bandgap of both n- and p-type layers is too low. Again incorporation of oxygen in the material proofs to increase the bandgap and simultaneously lower the refractive index. This results in a p-type window layer and an n-type layer that improves the back reflector.

Values reported for the mobility gap of µc-Si:H are in the order of 1.2 eV [22], lower and higher values are also reported depending on the amorphous and crystalline volume fractions in the material. Similarly, the optical bandgap can be varied between 1.1 eV and 1.6 eV [20], although lower values are often preferred to improve long wavelength (IR) light absorption. Typically, µc-Si:H is used in multi-junction solar cells in combination with a-Si:H to form a so called 'micromorph' solar cells [23], a name that is formed by a combination of Micro-crystalline silicon and aMorphous silicon. The higher optical bandgap a-Si:H material absorbs predominantly the UV and visible part of the spectrum, while the µc-Si:H cell extends the absorption up to deep IR light (1100 nm).

1.3.3 Multi-junction solar cells

Multi-junction solar cells have been developed to improve the spectral utilisation by stacking thin-film absorber layers in a single device. By doing this, it is possible to have an efficiency greater than the Shockley-Queisser limit. Currently, there is only a small

market for thin-film and multi-junction solar cells.

Directly depositing two or more solar cells in series is called monolithic integration. Each junction can be a different material with a different bandgap, such as amorphous silicon, micro-crystalline silicon, germanium and all kinds of semiconductor alloys. The highest bandgap layer forms the top cell, absorbing the highest energetic photons. Lower energetic photons will not be absorbed in the top cell and pass through to enter the next cell and so on. This makes it possible to have an efficiency beyond the SQ limit, by reducing non-absorption losses with two or more different bandgap materials, together with lower thermalisation losses in each of the subcells.

There are two main challenges in designing such a solar cell: first is to match the current generation in both junctions and second is to connect them internally without much electrical and optical loss [6]. Matching the current is necessary to avoid internal conduction losses by connecting two current sources in series. It can be achieved by tuning the thickness of the absorbed layers, looking at the generation probability and spectral response. Connecting the individual cells directly would lead to a loss in voltage, since it will create a *p*-*n* diode in the opposite direction. The *n*-layer of the top cell would then be directly connected to the *p*-layer of the bottom cell. In order to create an ohmic contact, the layers are connected with a tunnel-recombination junction (TRJ), visualised in figure 1.10. This junction is essentially a very thin and highly doped conductive layer which has defect states for very effective recombination. The holes from the bottom cell recombine with the electrons from the top cell, which is equivalent to conducting electrons from top to bottom cell. There are many different types of recombination layer materials, such as a-SiC:H, *n*+ microcrystalline, *n*+/*p*+ layers [24] and various metal oxides [25].

1.3.4 Device structure

Two different device structures of thin-film solar cells are possible, either in substrate (*n*-*i*-*p*) or superstrate (*p*-*i*-*n*) configuration. Figure 1.10 shows the different configurations,

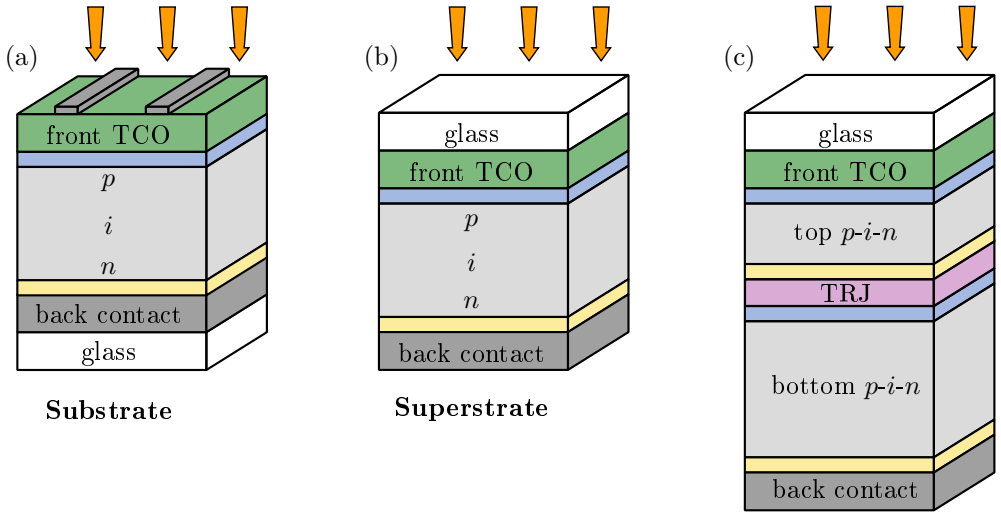

Figure 1.10: (a) single-junction substrate *n*-*i*-*p* cell, (b) single-junction superstrate *p*-*i*-*n* cell, (c) double-junction superstrate *p*-*i*-*n* cell. The thickness of the layers are not to scale.

where substrate solar cells are deposited from the back-contact side up and superstrate solar cells from the glass-side down. As this study focusses on superstrate configuration solar cells, the glass side of the cell is textured prior to deposition of the PV active layers in order to enhance the optical path length through the absorber layers. The contact side where the light will enter the solar cell will have to be transparent, materials that can be used here are called a transparent conductive oxide (TCO). Glass can also be exchanged by a flexible plastic substrate, since the production temperature of thin-film silicon is relatively low. This can simplify the production process and flexible light-weight solar cells can be obtained. In the case of a double-junction or tandem solar cell structure, which is shown in figure 1.10 (c), the top cell and bottom cell are internally connected in series through the TRJ.

1.4 Outline

The performance of monolithic multi-junction solar cells depends equally on each subcell in the structure, since they all should produce the same photocurrent. At any point of operation, the performance is limited by the subcell that produces the lowest current. However, the spectral irradiance and operating temperature of an installed solar cell varies with time and location by weather variation and position of the sun [26]. Especially temperature has a negative effect on the electrical parameters of a solar cell. Temperature mainly affects the open-circuit voltage and conversion efficiency, caused by an increase in intrinsic carrier concentration that leads to a higher level of recombination in the cell. Since the electrical performance of each subcell is affected on a different level, the performance of the total device is affected in a more complicated way [27], being limited in current by just one of the subcells.

In this thesis the electrical performance of micromorph tandem cells is studied and particularly the effect of temperature on the individual subcells, being amorphous silicon and microcrystalline silicon. Three-terminal solar cells are fabricated in order to characterise each cell individually and compare the findings with the total device performance. Precise dark JV measurements are carried out in a temperature range from 30 °C to 100 °C to reveal the dependency on temperature and find values for ideality factor, dark saturation current density and mobility gap. The evolution of open-circuit voltage and short-circuit current as a function of illumination intensity is obtained by measuring current-voltage curves at varying light intensities by using neutral density filters, obtaining so called pseudo JV curves.

Another motivation to individually characterise the subcells of the micromorph tandem structure is to investigate possible differences in material properties compared to single-junction cells with the same deposition parameters. A change in material properties might destabilise the current-matching condition of a tandem solar cell. It is therefore interesting to locate possible differences and investigate where they originated from.

2 | Theoretical Considerations

This section will discuss the theory that supports the analysis of the experimental results. First the working principle of monolithic multi-junction solar cells is explained. Since we are interested in the dark current-voltage characteristics of micromorph tandem solar cells and how temperature affects the individual subcells, the section continues with a detailed description of dark current-voltage characterisation. The last part of this section will discuss external quantum efficiency (EQE) measurements and how bias voltage can influence the obtained measurement curves. This is particularly important when the EQE of a multi-junction device is measured as this requires the application of bias voltage.

2.1 Monolithic multi-junction solar cells

As described in section (1.2.3) the maximum theoretical efficiency of a single-junction solar cell with a certain optical bandgap is given by the Shockley-Queisser limit (figure 1.6). If two or more absorber materials with different optical bandgaps are joined together in one device, however, the losses caused by spectral mismatch can be reduced. Each material can be optimised to absorb a specific part of the solar spectrum, thereby reducing thermalisation losses and non-absorption losses at the same time. Directly depositing two or more solar cells in series is called monolithic integration, the obtained device is called a multi-junction solar cell.

The operating principle of monolithic multi-junction solar cells is based on the addition of two or more single-junction cells, predominantly thin-film materials, where the current flowing through the device is equal in each layer. Such a device will operate most efficient if, for a given temperature and spectral irradiance, each subcell produces the same current. It is therefore very important to match the electrical and optical performance of every subcell at those conditions, taking into account the generation profile of the optical layer stack [6].

The electrical performance of a solar cell can be simplified with a single diode model that also includes series (R_s) and shunt resistance (R_sh):

$$J = J_0 \left(\exp\left(\frac{V - JR_\mathrm{s}}{mk_\mathrm{B}T} \right) - 1 \right) + \frac{V - JR_\mathrm{s}}{R_\mathrm{sh}} - J_\mathrm{ph} \tag{2.1.1}$$

where J_0, V, J, m, k_B, T and J_ph are the dark saturation current density, voltage and current density at the contacts of the cell, ideality factor, Boltzmann constant, cell temperature, and photocurrent density. Very often a shifting assumption is applied to find the electrical performance of a solar cell at any given photocurrent density. This is done by taking the dark current-voltage characteristics and simply adding the photocurrent density. For thin-film solar cells, which usually are made in a *p-i-n* configuration, this assumption is dismissed for various reasons [28], including the presence of recombination centres in the intrinsic layer. Measuring the dark current-voltage characteristics is, however, still valuable to determine the temperature dependence of the recombination current [15, 22, 29].

With a change of temperature, deviating from standard test conditions, the multi-junction cell will not be optimally matched. As the effect of temperature can be different

for each subcell, the combined effect on the multi-junction cell is more complex [27]. While the V_{oc} of each cell is affected individually, the V_{oc} of the multi-junction cell is the sum of all subcell voltages. The effect of temperature on the V_{oc} of a solar cell is caused by an exponential increase of the dark saturation current density J_0 [30] with temperature as:

$$V_{oc} = \frac{k_B T}{q} \ln\left(\frac{J_{sc}}{J_0} + 1\right). \tag{2.1.2}$$

V_{oc} will therefore drop with increasing temperature, which has a significant influence on the efficiency of the cell. The J_{sc} of a solar cell will only marginally increase with temperature at the same light intensity, since more photons will have enough energy to excite an electron from valence to conduction band by the decrease in bandgap energy [30]. The smaller bandgap of the subcells in a multi-junction device will cause a shift in spectral absorption towards lower energy photons. The top cell will absorb longer wavelength photons that would normally be absorbed in the bottom cell, while at the same time there is more thermal relaxation of high energetic photons caused by the decrease in bandgap energy. This ultimately may destabilise the current-matching condition from standard test conditions, as each subcell will not operate at its maximum power point.

2.2 Dark JV

This section will discuss the forward dark current-voltage transport mechanisms of a-Si:H, µc-Si:H and micromorph tandem solar cells. First of all the measurement of dark current-voltage characteristics will be discussed, followed by the solar cell parameters and electrical quality information that can be derived from it. The section will include a discussion and derivation on current spreading, which is an effect that complicates dark JV measurements for low forward bias voltages and is observed for p-i-n silicon solar cells [31].

2.2.1 Measurement principle

In equilibrium conditions at 0 V bias, the dark current of a p-i-n solar cell is essentially the current by recombination of thermally generated charge carriers (generation current density J_{gen}) in the depletion region of the cell. Electrons in the conduction band recombine with holes in the valence band in order to be collected at the p-type doped contact. Since there is no current running externally, one can state that without applying a bias voltage, the diffusion current of minority carriers is equal to the drift current in the direction of the internal electric field.

When a forward voltage is applied to the cells contacts, charge carriers are injected and the built-in potential of the doped layers across the intrinsic layer is lowered. A forward voltage is, by definition, directed opposite to the internal electric field. This favours diffusion of charge carriers through the depletion layer, while it decreases the drift current of the injected charge carriers in the opposite direction. For bias voltages below the built-in potential of the cell, diffusion of charge carriers will be the dominant transport mechanism. Since the travel time of minority carriers is larger than the capture time at localised states, charge carriers will be trapped, which limits the injection of carriers from the contacts [32]. Recombination helps reducing the number of trapped charges and will therefore increase the dark current by improving injection. The minority carrier

densities introduced by injection through the contacts increases exponentially with voltage, according to the Boltzmann approximation which states that the current by diffusion (recombination current density J_{rec}) increases exponentially with applied voltage V as:

$$J_{\mathrm{rec}}(V) = J_{\mathrm{rec}}(0) \exp\left(\frac{qV}{k_{\mathrm{B}}T}\right). \tag{2.2.1}$$

This leads directly to the Shockley equation for the net dark current density through a p-n junction as a function of applied voltage, assuming that the generation current is not a function of applied voltage [6]:

$$J(V) = J_{\mathrm{rec}}(V) - J_{\mathrm{gen}}(V) = J_0 \left[\exp\left(\frac{qV}{k_{\mathrm{B}}T}\right) - 1\right]. \tag{2.2.2}$$

Under high forward bias, the built-in potential of the diode can be completely diminished and if the applied voltage is high enough the internal electric field will reverse direction [32]. At this point the diffusion current and drift current will both add to a positive dark current, with the drift current being the dominant contributor.

Saturation current density and Ideality factor

The measurement of dark current-voltage is often performed to obtain values for the dark saturation current density J_0 and the ideality factor m. The current density in dark conditions J_{D} will have an exponential dependency on applied voltage in the moderate forward voltage region, being well described by the single diode equation, or Shockley equation (2.2.3), under the assumption that the generation current is negligible.

$$J_{\mathrm{D}}(V) = J_0 \left[\exp\left(\frac{qV}{mk_{\mathrm{B}}T}\right) - 1\right] \tag{2.2.3}$$

A least-squares fit to the exponential region of the JV curve data to the Shockley equation can be used to obtain values for both saturation current density J_0 and ideality factor m.

The dark saturation current density is most often described as the parameter that quantifies carrier recombination in a solar cell under illumination [33]. A leakage current of minority carriers will cause this recombination, which opposes the photogenerated current. A low value for J_0 will therefore lead to a better performing solar cell. The dark saturation current density will increase with temperature since it depends on the minority carrier concentration, which are thermally generated [30]. For a p-n junction the dark saturation current density due to recombination in the quasi-neutral regions $J_{0,\mathrm{q}}$ can be modelled as [6, 30]:

$$J_{0,\mathrm{q}} = qn_i^2 \left(\frac{D_n}{L_n N_{\mathrm{A}}} + \frac{D_p}{L_p N_{\mathrm{D}}}\right), \tag{2.2.4}$$

where D and L are the diffusion coefficient and diffusion length for electrons (subscript n) and holes (subscript p) respectively, and N_{A} and N_{D} are the concentrations of acceptors and donors. For a p-i-n solar cell, there will be a significant contribution to the saturation current density by recombination in the depletion region. The entire intrinsic layer thickness is now part of the depletion region [34]. The contribution to the dark saturation current by the depletion region $J_{0,\mathrm{d}}$ is given as [34, 35]:

$$J_{0,\mathrm{d}} = q\frac{W_{\mathrm{d}} n_i}{\tau_{\mathrm{d}}}, \tag{2.2.5}$$

where W_d is the depletion region width and τ_d is the effective minority carrier lifetime in the depletion region. As both contributions depend on the intrinsic carrier concentration, an increase in temperature will lead to an increased thermal generation of intrinsic carriers as [6]:

$$n_i^2 = N_\mathrm{C} N_\mathrm{V} \exp\left(\frac{E_\mathrm{V} - E_\mathrm{C}}{k_\mathrm{B}T}\right) = 4\left(\frac{2\pi k_\mathrm{B}T}{h^2}\right)^3 (m_e^* m_h^*)^{3/2} \exp\left(-\frac{E_\mathrm{G}}{k_\mathrm{B}T}\right), \tag{2.2.6}$$

where N_C and N_V are the effective densities of the conduction and valence band states, and m_e^* and m_h^* are the effective masses for electrons and holes respectively.

The m in equation (2.2.3) is the ideality factor of the p-n diode. It is added to the Shockley equation to stretch the validity to fit with experimental data [33] and to gain more understanding in the recombination processes in a solar cell. An ideal diode, where only band-to-band recombination in the bulk is present, will have an ideality factor of 1. The ideality factor of real solar cell devices can be higher than unity through other recombination processes. In thin-film silicon p-i-n solar cells, Shockley-Read-Hall (SRH) recombination via dangling bonds and tail states is the dominant recombination mechanism for dark current [22], which leads to an ideality factor of 2 at high level injection and through midgap defects [12]. A combination of different recombination processes will, however, lead to a non-integer value for m [36]. Kroon and van Swaaij add that a non-integer ideality factor can be attributed to an inhomogeneous distribution of defects, which leads to a different shift in quasi-Fermi level for electrons than for holes [37].

Since the recombination rate in a device depends on applied voltage, Deng and Wronski [38] introduced the voltage-dependent ideality factor as:

$$m(V) = \left[\frac{k_\mathrm{B}T}{q}\frac{d\ln\left(J_D(V)\right)}{dV}\right]^{-1}. \tag{2.2.7}$$

It was shown by van Swaaij *et al.* that the voltage-dependent ideality factor can be interpreted as the concentration of active recombination centers [29]. The temperature dependency of the ideality factor was attributed to the recombination efficacy, which is the recombination rate per trap state.

Voltage-dependent activation energy

The temperature dependency of the dark current density can be expressed in terms of the activation energy. Using the Arrhenius equation which relates thermal energy to the "rate" of a certain physical or chemical process, the activation energy of the dark current can be expressed as [22]:

$$E_\mathrm{a} = -\frac{\partial[\ln\{J_\mathrm{D}[(k_\mathrm{B}T)^{-1}]\}]}{\partial[(k_\mathrm{B}T)^{-1}]}. \tag{2.2.8}$$

where E_a is the activation energy. Since experimental measurements of the dark current represent the total recombination rate in the cell, applying equation (2.2.8) to a dark JV curve will give the activation energy of the total recombination. The dark current of a-Si:H and µc-Si:H p-i-n cells in low forward voltage is dominated by SRH recombination. Pieters *et al.* [22] derived an analytical expression for the thermal activation energy of the SRH process. The total recombination rate R of the device, which is assumed to

be dominated by recombination in the intrinsic layer only, depends on the spatial and energetic distribution of trap states [15] and the recombination efficacy as:

$$R = \int_0^W v_{\mathrm{th}} \sigma_n \frac{np}{R_\sigma n + p} \left(\int_{E_{fp_t}}^{E_{fn_t}} N_t(E_t) dE_t \right) dx, \tag{2.2.9}$$

where W is the thickness of the intrinsic layer, v_{th} is the thermal velocity, σ_n is the capture cross section for electrons, R_σ is the ratio between the capture cross sections for electron and hole trapping, n and p are the concentrations of free electrons and holes respectively, E_{fn_t} and E_{fp_t} are the quasi-Fermi levels for trapped electrons and holes and $N_t(E_t)$ is the concentration of active recombination centers [15, 22, 29]. An analytic expression for the activation energy of the SRH recombination process was determined [22], which relates to the mobility gap E_{mob} and the thermal ideality factor m_{th} of the *p-i-n* cell as:

$$E_{\mathrm{a}}^{\mathrm{R}} = \frac{E_{\mathrm{mob}} - V}{m_{\mathrm{th}}} + 3k_{\mathrm{B}}T. \tag{2.2.10}$$

The thermal ideality factor was introduced by Pieters *et al.* [22]. It replaces the normal ideality factor in a way that is characterises the dark current independent of the effect of applied voltage on the concentration of active recombination centers [15]. It has been demonstrated that for both a-Si:H [15] and µc-Si:H [22] cells this thermal ideality factor is 2.

2.2.2 Current Spreading

Current spreading or leakage current is a frequently observed phenomenon in the low forward voltage region of dark current-voltage measurements of thin-film *p-i-n* solar cells. The current collection through the metal contact area of a single cell is observed to be significantly higher than can be expected from the Shockley equation. Willemen determined that the effect is caused by a combination of lateral conduction in the *n*-layer and a possible shunt path connecting the *n*-layer and the front TCO [31]. Upon placing a bias voltage over the contacts of a *p-i-n* cell, a current is expected to flow from the equipotential TCO layer to the metal contact dot. This contact dot would ideally limit the area of the cell. However, the conductive *n*-layer below the contact can place a bias voltage in the periphery of the metal contact and thereby create a current flow outside the contact area. This current will be laterally conducted through the *n*-layer and ultimately be collected through the metal contact, hereby essentially increasing the active cell area (see figure 2.1 (a)).

When the applied voltage increases, the resistance of the *n*-layer will cause the voltage to gradually drop with increased distance from the metal contact. The current that has to be conducted laterally will exponentially increase with applied voltage, which is why at some point the current spreading effect will be completely diminished. Willemen stated that this point lies around 0.60 V for a-Si:H cells, this however depends heavily on the thickness and composition of the *n*-layer. When measured at a higher temperature, the current spreading effect will also fade out by the exponential increase of dark saturation current density with temperature. A lower applied voltage would already result in a generated current that is too high for lateral conduction through the *n*-layer.

One solution to prevent lateral current collection is to remove the peripheral *n*-layer with reactive ion etching (RIE), using the metal contact dot as a mask. Figure 2.1 (a)

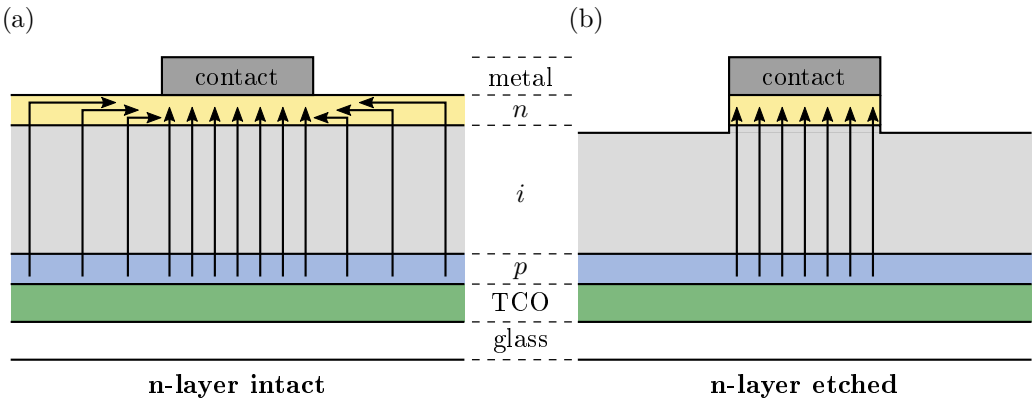

Figure 2.1: (a) Current spreading effect by lateral conduction through n-layer (b) Removal of n-layer by etching prevents lateral current collection. Adapted from [31].

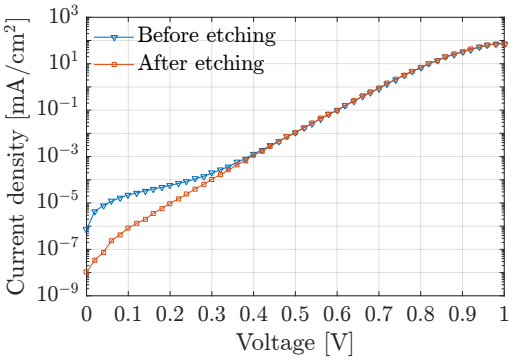

Figure 2.2: Current spreading effect observed in a dark JV measurement of an a-Si:H single-junction cell with an intrinsic layer thickness of 200 nm. Etching the peripheral n-layer removes the effect.

shows the current paths in 2D for a normal p-i-n cell, where the n-layer is at a bias voltage and conducts current towards the metal contact. Figure 2.1 (b) shows the situation where the n-layer has been removed with RIE, effectively preventing the current spreading effect.

Willemen further discussed that the collected current without etching the n-layer was in some measurements over 4 orders of magnitude larger than after etching. This could not be attributed to lateral conduction of current through the n-layer only, since the sample substrate area was not 4 orders of magnitude larger than the contact dot area. Willemen therefore assumed there had to be a shunt between the n-layer and the front TCO, most probably close to the edges of the sample where the deposition quality was lower. Removal of the n-layer would, however, remove this shunt as well.

In an attempt to quantify the effect of lateral current collection, we tried to understand the physics behind current spreading. For simplicity, the contact is assumed to be a circle with radius r (see figure 2.3) in the centre of a circular substrate with a radius of 12.5 mm.

For a distance $r + x$ from the centre of the contact, the resistance R of the n-layer can be calculated as

$$R(x) = \int_r^{r+x} \frac{1}{\sigma} \frac{1}{2\pi r t} dr = \frac{\ln\left(\frac{r+x}{r}\right)}{2\pi\sigma t}, \tag{2.2.11}$$

where σ and t are the conductivity an thickness of the n-layer. The applied voltage has

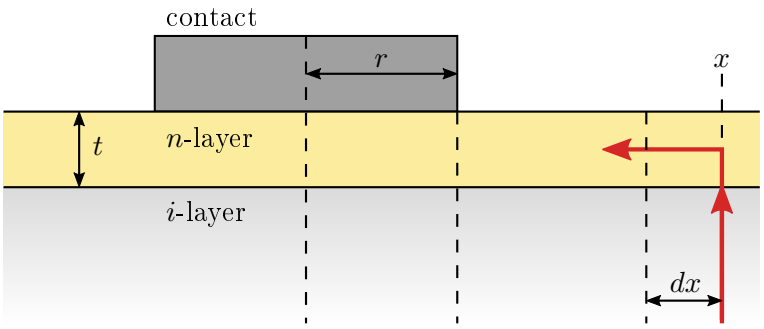

Figure 2.3: Detailed sketch to support the current spreading model.

dropped with ΔV at position x, depending on the current generated by the p-i-n cell at position x and applied voltage $(V - \Delta V)$. This current is assumed to follow the single-diode equation, which is justified in the low forward voltage region for both a-Si:H and µc-Si:H [22, 37, 39].

$$\Delta V(x) = I(x) \times R(x); \quad I(x) = J_0 \exp\left(\frac{q\,[V - \Delta V(x)]}{m k_\mathrm{B} T}\right) \times 2\pi(r + x)dx \tag{2.2.12}$$

It is evident that the voltage drop over the n-layer depends on the current generated at position x, however, this current depends on the applied voltage minus this voltage drop $(V - \Delta V)$. This leads to the following equation for ΔV:

$$\Delta V(x) = V - \frac{m k_\mathrm{B} T}{q}\left(\ln\left[\frac{\Delta V(x)}{2\pi(r + x)dx R(x) J_0}\right]\right). \tag{2.2.13}$$

By numerically solving the voltage drop ΔV for a range of applied voltages, the effect of current spreading in the low forward voltage region could be visualised. An example is included in appendix (6.3).

2.2.3 Characteristics of a-Si:H and µc-Si:H single-junction cells

The forward dark current-voltage curve of an a-Si:H single-junction cell can be divided into three voltage regions as was proposed by Sturiale *et al.* [39], this is shown in figure 2.4. The voltage regions are obtained from simulations and depend on the intrinsic layer thickness, the midgap state density and the free carrier mobilities [39]. In each region the current is dominated by a single conduction mechanism or a combination of mechanisms acting in series. The first region from 0 V to V_R, where the "R" stands for recombination, is determined by SRH recombination. Injected holes from the front and electrons from the back contact will diffuse through the intrinsic layer. The doped layers will prevent the carriers from passing the entire structure by an increased potential barrier, therefore they will have to recombine in the bulk intrinsic layer through midgap states [39, 40]. The recombination rate usually has its maximum located near the p-i interface due to an increased local defect density [29, 40], which lowers the mobility of holes [39]. The second region is referred to as the exponential region. It reaches from V_R to V_E, where the "E" stands for exponential. The current in this region is controlled by diffusion and recombination, dominated by diffusion as the applied voltage increases. The last region is recognisable by a more slowly increasing current, which is called the electron space charge limited current (SCLC) region. The conduction mechanisms are now the injection

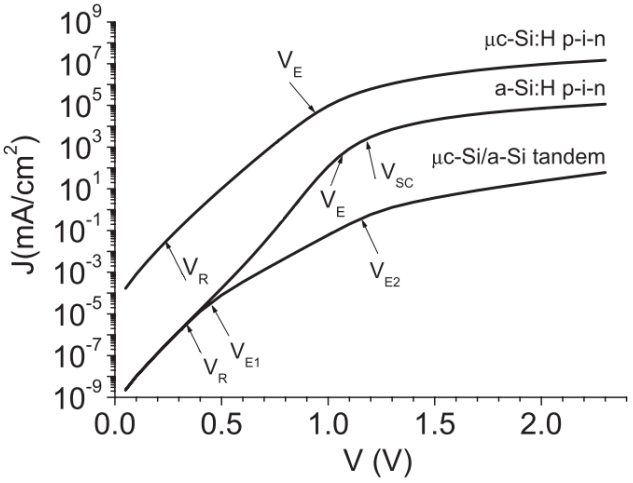

Figure 2.4: Dark current-voltage simulation curves of two single-junction solar cells, a-Si:H and µc-Si:H, and a micromorph tandem cell based on these SJ cells. Thicknesses of the intrinsic layers are 200 nm and 1500 nm respectively. Indications of V_{R}, V_{E} and V_{SC} to define the regions controlled by a combination of different conduction mechanisms, demonstrated by Sturiale *et al.* [39].

of both charge carriers, drifting through the intrinsic layer of both charge carriers and recombination in the bulk intrinsic layer. The high density of charge carriers being injected into the cell causes trapping of charge carriers at localised states near the *i*-*n* interface, creating a potential barrier (a virtual cathode) for injection of more electrons [40]. A similar barrier is formed at the *p*-*i* interface, this time a virtual anode, but the current is limited by injection of electrons through the *i*-*n* interface. The voltage V_{SC}, where "SC" stands for space charge, is related to the voltage where the virtual cathode at the *i*-*n* interface is formed.

Similar to the a-Si:H single-junction cell, the applied voltages V_{R} and V_{E} can be used to define the first two regions of the µc-Si:H single-junction dark *JV* curve [39]. The current will again increase more slowly in the high forward voltage region, but this is attributed to series resistance. The higher dark current density for µc-Si:H is clearly visible in figure 2.4, caused by the smaller mobility gap of this material which favours band-to-band recombination.

2.2.4 Characteristics of micromorph tandem cells

In micromorph tandem cells an a-Si:H cell is connected in series with a µc-Si:H cell. This creates a *p*-*n* diode in opposite direction to the top and bottom cell. In order to sustain the current through the cell, charge carriers from the top and bottom cell will have to recombine at this junction through tunnelling in the so-called tunnel recombination junction (TRJ). Under illumination the photogenerated charge carriers will become trapped at gap states on either side of TRJ, placing the *n*-*p* junction in forward bias [39]. In dark conditions, however, the junction will be placed in reverse bias by the externally applied forward voltage. Sturiale *et al.* determined that thermal generation of electron-hole pairs in the TRJ is required at a high forward voltage over the tandem cell to facilitate the dark recombination current through the tandem cell. When the thermal generation of carriers in the TRJ is not sufficient to sustain this current, a larger part of the applied voltage will

be used to place the TRJ in reverse bias to increase generation of e-h pairs [39]. This will ultimately lead to a loss of voltage in the TRJ, lowering the voltage drops over the top and bottom cell.

The dark current-voltage curve of a micromorph tandem cell can be divided into three regions, as is shown in figure 2.4. The first exponential region between $0 < V < V_{E1}$ is limited by recombination, and at higher applied voltage also by diffusion, in the intrinsic a-Si:H bulk layer. There is only a very small voltage drop over the µc-Si:H bottom cell, caused by the difference in current generation through applied voltage. The second exponential region between $V_{E1} < V < V_{E2}$ is controlled by recombination in the intrinsic layers of both the a-Si:H top cell and the µc-Si:H bottom cell, along with diffusion in the a-Si:H top cell. The third region is determined by diffusion in the µc-Si:H bottom cell intrinsic layer, combined with electron SCLC in the a-Si:H top cell intrinsic layer and thermal generation of e-h pairs in the TRJ [39].

2.2.5 Pseudo JV

The dark current-voltage characteristics can also be obtained through variable intensity measurements (VIM). This is a method that determines the open-circuit voltage and short-circuit current from illuminated JV measurements at different light intensities, resulting in a J_{sc} - V_{oc} graph, called a pseudo JV curve. The relation of V_{oc} and J_{sc} in the intermediate illumination regime, where practical operation of a solar cell is recommendable [41], is described by the single diode equation (2.2.3) with voltage and current density replaced with V_{oc} and J_{sc}:

$$V_{oc} = \frac{mk_BT}{q} \ln\left(\frac{J_{sc}}{J_0}\right). \tag{2.2.14}$$

This implies that the saturation current density J_0 and ideality factor m under illumination can be derived from pseudo JV curves, demonstrated by Kroon *et al.* [37]. Moderate values for series resistance will not influence the high voltage region of this curve, where it would influence the dark JV curve. This is because at open-circuit voltage, there is no current running through the cell, meaning that series resistance does not influence the value of open-circuit voltage. The J_{sc} will only be influenced at high values for series resistance, since then R_s might increase the slope of the illuminated JV curve close to the J_{sc}.

2.3 Quantum efficiency

Characterisation of short-circuit current density and spectral utilisation of solar cells is often performed with a quantum efficiency measurement, which gives the wavelength dependent ratio between the collected current and photon flux. Measurement procedures for multi-junction solar cells are more complicated than for single-junction cells, since separate measurements of each absorber layer are desired. This introduces some difficulties in obtaining quantum efficiency data without measurement artefacts.

The QE is often related to the spectral response, which is a measure of current produced per unit power [42]:

$$QE(\lambda) = \frac{SR(\lambda)hc}{\lambda q} = \frac{SR(\lambda)E_{ph}(\lambda)}{q}. \tag{2.3.1}$$

Here $SR(\lambda)$ is the spectral response, q is the electron charge, λ is the wavelength, h is Planck's constant, c is the speed of light, and $E_{\mathrm{ph}}(\lambda)$ is the photon energy as a function of wavelength. When the spectral response of the solar cell is measured under short-circuit conditions, integrating over wavelength of the spectral response multiplied with the spectral power density at AM 1.5 will give a value for J_{sc}, which should be in agreement with measuring the same current density under 1 sun solar irradiation:

$$J_{\mathrm{sc}} = \int_{\lambda} \mathrm{AM1.5}(\lambda) \cdot SR(\lambda) d\lambda = \int_{\lambda} \mathrm{AM1.5}(\lambda) \cdot QE(\lambda) \frac{q}{E(\lambda)} d\lambda. \tag{2.3.2}$$

The EQE can also be used to determine optical and electronic losses, which can even be separated by measuring the EQE at different voltage bias [43], [44].

2.3.1 Voltage bias dependence

In many thin-film devices, the collection of charge carriers is voltage dependent [42, 45] and this will result in a measurement artefact if the voltage over the cell is wavelength dependent. Considering amorphous silicon (a-Si:H) as the absorber material, one needs to look at the ambipolar photocarrier collection behaviour. In a-Si:H cells, the absorption of electrons and holes is established by sandwiching an intrinsic layer between a thin p- and n-layer. This generates an internal electric field that results in field-driven collection. By applying an external voltage bias, the internal electric field can be changed, which will result in a change of collection efficiency. The basic structure of a-Si:H cells is p-i-n, starting with the layer where light will enter. Since the collection is ambipolar, the travel distance for collection depends on the location in the i-layer where the charge carriers are generated, which is depending on wavelength. For short wavelengths, charge carriers are generated close to the p-i interface, which makes that the electrons need to drift across the entire i-layer in order to be collected. The long travel distance results in higher recombination, making electrons the limiting charge carrier for short wavelength photons. Long wavelength photons are absorbed more homogeneously in the intrinsic layer. The voltage dependence is therefore different for long and short wavelength illumination. The dependence on voltage in the EQE can be used to measure collection problems at the p- or n-layer by measuring the EQE at different bias voltage. For example, a decrease in EQE for long wavelengths at a forward bias with respect to a EQE at 0 V indicates poor hole transport [44, 46].

For correctly measuring the spectral response of the individual subcells of a multi-junction solar cell, applying bias illumination and bias voltage is required. The measured subcell should be current-limiting over the entire spectral range, while at the same time being at short-circuit conditions [45]. This will be explained on a tandem cell using figure 2.5. The bottom subcell in figure 2.5 is measured with a low intensity probing light source, while the non-measured top subcell is saturated with a high intensity short-wavelength bias illumination. The Fermi level of the top subcell will split into quasi-Fermi levels $E_{F,p}$ and $E_{F,n}$, resulting in a forward bias operation. While the applied voltage in figure 2.5 (a) is 0 V, the bottom cell is pulled in reverse bias by the same potential difference, $E_{F,n} - E_{F,p} \approx qV_{\mathrm{oc}}$, of the top subcell. The bottom cell will therefore not be operating at short-circuit conditions. Instead the internal electric field of the bottom cell is enhanced, resulting in more effective charge carrier separation and collection.

In figure 2.5 (b) the V_{oc} of the top subcell is applied as bias voltage. The top subcell will still operate at a forward bias approximately equal to its V_{oc}. The reverse bias in the

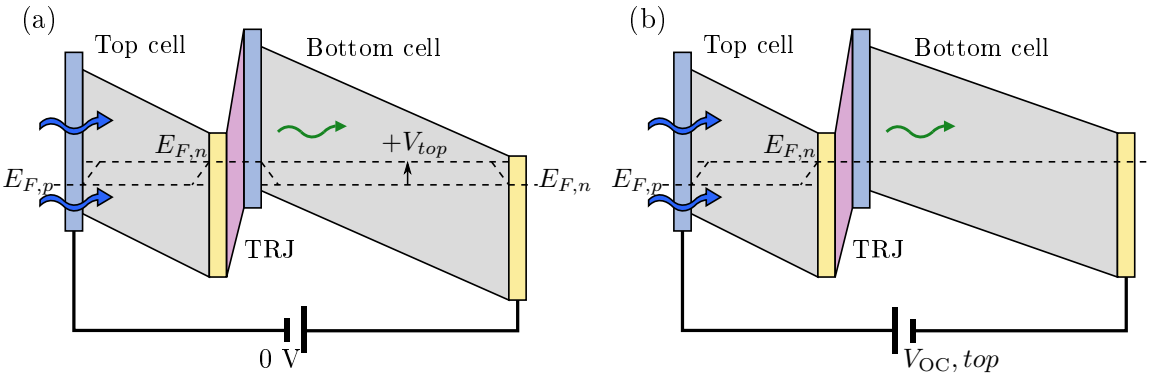

Figure 2.5: Schematic representation of an energy band diagram of a tandem solar cell while the bottom subcell EQE is measured under bias illumination and bias voltage. Figure (a) shows the situation where 0 V bias is applied, figure (b) shows the situation where the approximate V_{oc} of the top subcell is applied. Note that the coloured area represents the bandgap of the tandem subcells.

bottom cell will, however, be neutralised by the applied voltage. This way the bottom subcell can be measured at short-circuit conditions.

3 | Experimental

The experimental section of this study will elaborate on the preparation methods and the setups used for characterisation of the prepared samples. All equipment used for device preparation is located in the class 10.000 cleanroom area of the Else Kooi Laboratory in Delft. The last part will give an overview of the device structures used in this thesis and the specific steps taken to fabricate these devices.

3.1 Device preparation

The three main processes used for device preparation are described in this section, starting with thin layer deposition for solar cell materials, transparent conductive oxides (TCO's) and metal contacts, and finally the removal of undesired layers. Each process will be described, followed by the actual system used for device preparation of this project.

3.1.1 Radio Frequency Plasma Enhanced Chemical Vapour Deposition

The most commonly used method for the deposition of thin layers of amorphous silicon is Radio-Frequency Plasma-Enhanced Chemical Vapour Deposition (rf-PECVD). This process can be operated at relatively low temperatures (~200 °C), since most of the energy that drives the chemical reactions will be provided by a plasma. Figure 3.1 shows a 2D schematic of a typical rf-PECVD deposition chamber (DPC), including a pump system, a gas system and a radio frequency generator. The chamber itself consists of two electrodes, one of which is the substrate holder. The substrate holder is located closest to the heater that regulates the substrate temperature and is grounded.

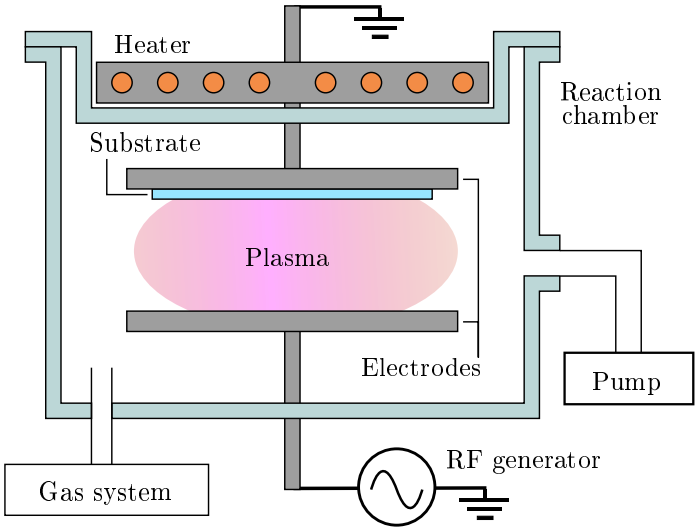

Figure 3.1: Schematic representation of an rf-PECVD reaction chamber, adapted from [6].

Prior to deposition, the chamber will be pumped to vacuum in order to remove present

gasses that could possibly interfere. A plasma will then be initiated between the electrodes by an oscillating electric field, originating from the RF generator at a typical frequency of 13.56 MHz for a-Si:H and doped layers and 40 MHz very-high frequency (VHF) for intrinsic µc-Si:H layers [20]. Process gasses that enter the chamber, such as SiH_4, CH_4, H_2 and CO_2, will react by interaction with high energetic electrons in the plasma and form reactive molecules that deposit on any nearby surface. The composition and growth rate of the layer that is formed depends on substrate temperature, chamber pressure, plasma power and gas flow rates. The thickness of the layer is controlled by the deposition time.

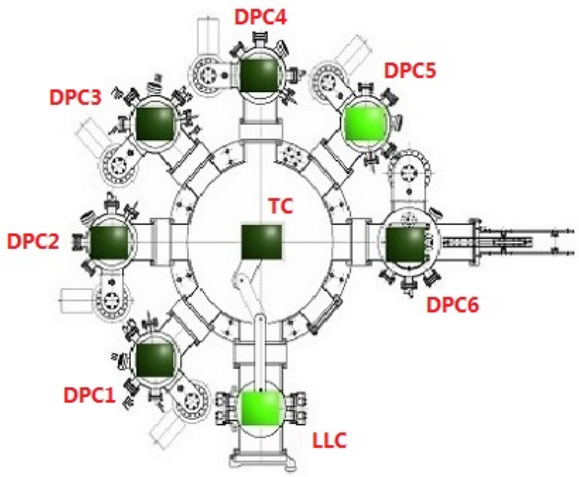

Figure 3.2: Schematic overview of AMIGO, a PECVD cluster tool owned by the PVMD group with 4 rf-PECVD chambers, 1 VHF-PECVD chamber and 1 sputtering chamber for TCO depositions.

Depositions of this project were performed in AMIGO (figure 3.2), a multi-chamber rf-PECVD system by Elettrorava. The substrate can enter the cluster tool through the load-lock chamber (LLC) and the main transport chamber (TC) with a robotic arm that can further distribute it to the six adjacent process chambers. The reactors are 4 rf-PECVD processing chambers, 1 VHF processing chamber and 1 magnetron sputtering chamber (DPC6). This system is automated and can be controlled through a `LabVIEW` program that can run recipes with up to 1000 processing steps.

3.1.2 Physical Vapour Deposition

Physical Vapour Deposition (PVD) is a range of purely physical processes to create thin films in a high vacuum environment. This is achieved by producing a vapour from a certain target material, which deposits on substrates and surroundings. Two different methods of PVD are described in this section, Radio Frequency Magnetron Sputtering and Electron Beam PVD. For each method the vapour is produced in a different way.

Radio Frequency Magnetron Sputtering

In the sputtering process a plasma is used to accelerate gas atoms with high velocity towards a target. The target material is struck with enough force to loosen atoms from its surface, which condense on surfaces in its proximity such as the vacuum chamber walls and the substrate. The sputtering gas is most commonly an inert gas with atomic weight close

to the atomic weight of the target material, in order to achieve efficient energy transfer. RF magnetron sputtering increases the probability for sputter gas atoms to be ionised by using strong electric and magnetic fields to trap charged plasma particles near the target. The path length of electrons is increased, since they circle around the magnetic field lines and thereby have a higher chance to strike a gas atom. This ultimately increases the deposition rate and makes it possible to sustain the plasma at a much lower pressure [47].

Depositions of this project were performed in deposition chamber 6 (DPC6) of AMIGO, owned by the PVMD group, which is an RF magnetron sputtering chamber designated for zinc oxide ZnO depositions at temperatures ranging between 50 °C and 400 °C. The sputter gas is argon, Ar, and the target for aluminium-doped zinc oxide has 2 wt. % Al_2O_3 and 98 wt. % ZnO. DPC6 includes a shutter that allows for pre-sputtering the chamber with a fresh layer of ZnO before exposing the substrate.

Electron Beam Physical Vapour Deposition

Electron beam (E-beam) PVD is a physical process where high energetic electrons from an electron gun are used to evaporate a material, predominantly metals, which condense on any surface in a vacuum chamber. These are mostly the metals with a high melting temperature, like chromium and titanium, since low melting temperature metals, like silver, can be evaporated by a thermal process. Aluminium is an exception since it can form alloys with a tungsten boat, which is why it is evaporated by an electron beam in a ceramic crucible.

The metal depositions for this project were performed in the Provac PRO500S system, owned by the PVMD group, which allows for both e-beam and thermal evaporation in the same vacuum chamber. Silver is thermally evaporated on a tungsten boat heated by a current source, while a rotating set of four crucibles holds the high melting temperature metals like Cr and Ti. The electron gun has a charged tungsten filament that generates an electron beam in high vacuum. Substrates are placed in a rotating stage in special holders that define the desired metal contact pattern or grid.

3.1.3 Reactive Ion Etching

Reactive Ion Etching (RIE) is a dry etching technique that uses a plasma to create ions and radicals that remove material from the substrate by collision or chemical reaction. The etchant is chosen based on the material that has to be removed. For instance, sulphur hexafluoride, SF_6, is used to etch silicon. A plasma is initiated from the etchant gas with an RF signal and collision with electrons creates ions and radicals. The substrate is placed in the bottom of the vacuum chamber with the etching layer facing the plasma. The main advantage over wet etching is that RIE will only etch the exposed surface of the substrate anisotropically, which means that it will etch in a straight line. Areas covered, by for instance metal contacts, will therefore be protected, while wet-etching would damage the layer underneath it. This is called undercutting.

Reactive ion etching for this project is performed with an Alcatel plasma etcher. The available process gasses are CF_4, SF_6, CHF_3, BCL_3, Cl_2, N_2 and He. The system can etch wafer or glass sizes up to 4".

3.2 Characterisation

This section will describe the measurement setups used for optical and electronic characterisation. First the setups used for material characterisation will be discussed, such as Raman spectroscopy, spectroscopic ellipsometry, four-point probe and dark conductivity. Secondly the setups used for device characterisation are discussed, which includes the dark and light current-voltage and external quantum efficiency setups.

3.2.1 Raman spectroscopy

Raman spectroscopy is a characterisation method which is based on inelastic scattering of photons with vibrational modes in a sample material. This is called the Raman effect. In a Raman microscope, samples are illuminated with focussed monochromatic light. Only a small fraction of the incident photons scatter inelastically and will undergo a frequency change. The energy change accompanied with the interaction of photon and material depends on the atomic mass and bond strength inside the sample, since these determine the vibration frequency. The energy and thus frequency shift is very specific for each bond, which makes it a suitable interaction for structure characterisation. Since the occurrence of Raman scattering is more than a million times smaller than regular Rayleigh scattering, one needs a very sensitive detector. The output of a spectral acquisition is most commonly given in a spectrum of Raman shift [cm^{-1}] versus intensity in arbitrary units. The inverse length unit is originating from the photon wavenumber, which is directly related to energy.

In this work, Raman spectroscopy is used to determine the crystalline fraction of the microcrystalline silicon layers. This is done by looking at the transverse optic (TO) phonon modes for amorphous silicon (a-Si:H) and crystalline silicon (c-Si). They have a peak Raman shift of 480 and 520 cm^{-1} respectively. The crystallinity is defined as [48]:

$$I_c = \frac{I_{\mathrm{TO,c-Si}}}{\gamma I_{\mathrm{TO,a-Si:H}} + I_{\mathrm{TO,c-Si}}}. \tag{3.2.1}$$

The factor γ represents the Raman scattering cross-section of the c-Si TO mode compared to the a-Si:H TO mode [48] and is set to 0.8. An argon laser with a wavelength of 514 nm is used as monochromatic light source and a Renishaw InVia Raman microscope is used for Raman spectrum acquisition. The spectra are fitted to the optical and acoustical modes with a `MATLAB` code which outputs the crystallinity of the samples.

3.2.2 Four-point probe

A four-point probe or four-terminal probe is a device that is used to determine sheet resistance of thin films. It gives more accurate values than conventional two-terminal measurement systems by eliminating contact and current lead losses. Separate pairs of wires and probes are used for current supply and voltage sensing, the source and sense pairs respectively. The source pair forces a current to run through the measured layer. The sensing pair is located on the inside of the source pair and measures the voltage drop over a short distance. The current through the voltage sensing wires is negligible, which makes this type of measurement very accurate.

An Advanced Instruments Technology CMT-SR2000NW four-point probe was used to measure the sheet resistance of TCO layers with varying thickness and deposited at different temperatures. Values for sheet resistance are a direct output of the setup. Combined with the thickness of the layer, the conductivity can be determined.

3.2.3 Dark conductivity

The dark conductivity setup can be used to measure the conductivity of thin-film layers at different temperatures. This is a widely used technique in photovoltaic research to determine the activation energy of materials which relates to the material quality. Two closely spaced contacts with known dimensions are deposited on the material sample and a voltage is applied with two probes. The current and thus resistance R are measured and together with the layer thickness t the conductivity σ of the material can be calculated:

$$\sigma = \frac{1}{R}\frac{d}{t \times l}. \tag{3.2.2}$$

Here d and l are the spacing between the contacts and the length of the contacts. When this conductivity is measured at various temperatures, the slope of the logarithmic dark conductivity versus $1/k_{\mathrm{B}}T$ equals the activation energy E_{a} following Arrhenius' law:

$$\sigma_D(T) = \sigma_0 \exp\left(-\frac{E_{\mathrm{a}}}{k_{\mathrm{B}}T}\right), \tag{3.2.3}$$

with σ_0 the pre-exponential factor (where $\ln\sigma$ intersects $1/k_{\mathrm{B}}T = 0$), and k_{B} the Boltzmann constant. Activation energy can thus be fitted from the acquired data.

Prior to the measurement, the contacts should be annealed at 130 °C for 30 minutes. This can be done on the thermal chuck in the setup, but when multiple samples are measured at ones, it saves time to anneal the contacts in a laboratory furnace all at ones.

3.2.4 Spectroscopic ellipsometry

A frequently used method to determine optical constants and the thickness of thin-films is spectroscopic ellipsometry (SE). The surface of a sample is illuminated with a light spot under different angles and a detector is positioned on the opposite side. It measures the phase difference and the amplitude ratio of both p- and s-polarised light for a range of different wavelengths. Gathered data needs to be fitted with computer models for each of the layers in a sample. For each layer it requires the input of an approximate thickness and optical constants after which it will calculate the measurement values using a least-squares minimisation.

In this project SE was used to determine the thickness of various silicon and TCO layers to find the deposition rate for each material. The measurement setup was an M-2000DI J.A. Woollam Co., Inc. Spectroscopic Ellipsometer.

3.2.5 Dark JV

Dark JV measurements are most frequently used to find the saturation current density J_0 of solar cells, which is a measure of recombination in the device [33]. By applying a

voltage bias over a solar cell in dark conditions, charge carriers will be injected into the device which will have to recombine in order to generate a current flow. The current flow in forward bias will in theory follow the Shockley equation, which can be used to determine the ideality factor m and dark saturation current density J_0.

When measured at different temperatures, dark JV measurements can also be used to determine the voltage-dependent activation energy and mobility gap of a solar cell [22], as well as to determine the temperature dependence of the ideality factor and dark saturation current density.

The measurement setup of the PVMD group consists of a thermal chuck powered by a Temptronic ThermoChuck® TP 03000 and a very precise electrometer, a Keithley 6517A, all controlled by a `LabVIEW` program. The accuracy of the current readings is better than 0.01%. The voltage is set with an accuracy of 0.15%, the temperature with an accuracy of $\pm$ 0.5 °C [29]. After every voltage setting, the system waits for a controllable amount of time to let the current stabilise before it measures the current and sets the next voltage. On top of that, it measures the current 10 times and checks if the difference between two subsequent data points is lower than 10%, thereby ensuring that the measured current has been stabilised. The measurement setup is protected to excessive currents by limiting the maximum current to approximately 12 mA. A higher current could potentially damage the setup but also the solar cell itself.

3.2.6 Illuminated JV

An illuminated JV measurement is performed to examine the current-voltage behaviour of a solar cell under exposure of light. Typically the spectral irradiance of the light source(s) is matched to the AM 1.5 spectrum with an intensity of 1000 W m^{-2} in order to meet standard test conditions. While the solar cell undergoing the measurement will heat

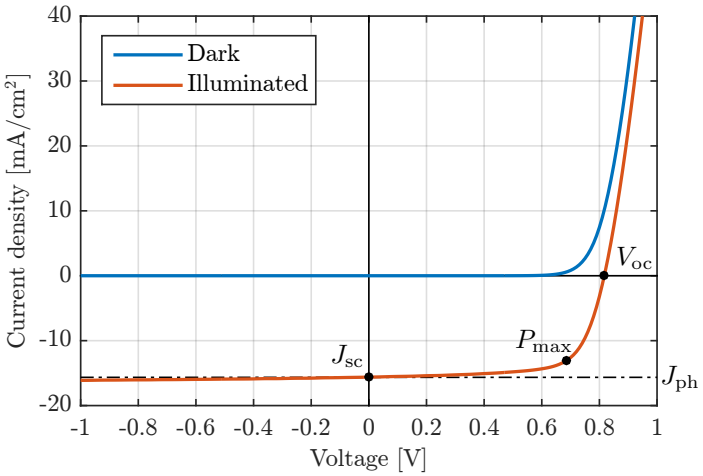

Figure 3.3: JV characteristics of a solar cell in the dark and under illumination, locating V_{oc}, J_{sc}, P_{max} and J_{ph}.

up under illumination, it is often cooled to 25 °C on the substrate holder.

For an ideal diode, the illuminated JV curve is a superposition of the dark JV curve and a photocurrent density J_{ph}. An illuminated JV measurement, shown in figure 3.3, is

used to find values for open-circuit voltage (V_{oc}), short-circuit current density (J_{sc}) and maximum power point (P_{max}). Other parameters such as fill factor (FF), reflecting the shape of the curve, and efficiency (η) can be deduced from these parameters. The efficiency of a solar cell is defined as the ratio of the generated power and the power coupled into the device as:

$$\eta = \frac{P_{max}}{P_{in}} = \frac{J_{mpp}V_{mpp}}{P_{in}} = \frac{J_{sc}V_{oc}FF}{P_{in}}. \tag{3.2.4}$$

The measurement setup of the PVMD group consists of a Wacom class AAA solar simulator, with a helium and a xenon light source. JV curves are measured with an Agilent Technologies 34980A voltage bias supply and a Keithley 2601B sourcemeter, controlled with a `LabVIEW` program. This program also controls the stage temperature by activating a liquid cooling system (Julabo F25) that can range in temperature from 15 °C to 55 °C.

3.2.7 External quantum efficiency

An external quantum efficiency (EQE) measurement is a characterisation method of a solar cell that gives the relation between the flux of photons coupled into the device and current collected at the terminals, per wavelength. It can be used to determine optical and electronic losses, which can also be separated by measuring the EQE with different voltage bias [43, 44]. The EQE is determined by measuring the spectral response with a home-built setup, shown in figure 3.4.

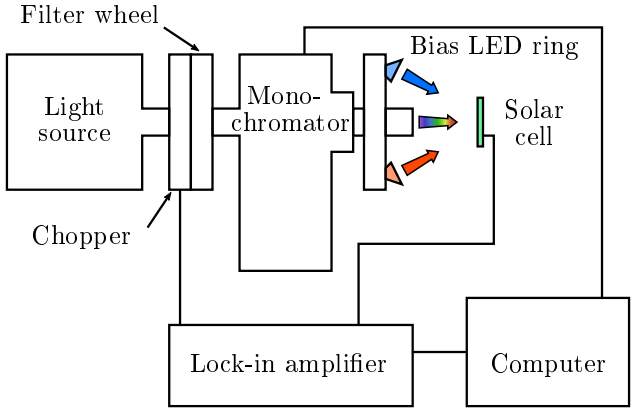

Figure 3.4: Schematic representation of the home-build EQE measurement setup owned by the PVMD group.

This setup uses a Xenon lamp as a light source (Oriel Apex, Newport), which has a fairly homogeneous spectral intensity between 300 nm and 800 nm. A chopper wheel modifies the light to a frequency of 123 Hz, which makes it possible to retrieve the spectral response signal from the solar cell by a lock-in amplifier (EG&G Instruments 7260 DSP). This particular frequency is chosen at an arbitrary value, being not a higher order of a frequency containing noise, such as the 50 Hz frequency of artificial light. The modified light is entering a monochromator (Oriel 1/8 m Cornerstone), containing two gratings that are optimised at a blaze wavelength of 350 nm and 750 nm respectively. In order to have the highest output of the monochromator, the gratings are switched at a wavelength of 540 nm. The monochromatic light is then focussed on the sample with a lens.

Every measurement is preceded by a calibration with a Hamamatsu silicon reference

diode. The quantum efficiency of this diode is known, which makes it possible to translate the current of this diode to the photon flux of the modified monochromator light. A bias LED ring is located around the output light beam of the monochromator. It contains 8 groups of LED's ranging from UV to deep IR and the intensity of each type is individually controllable. These LED's can be used to saturate subcells in multi-junction solar cells with DC light.

The measurement is controlled by a computer running a `LabVIEW` program. It controls the monochromator wavelength settings, the sensitivity and time constant of the lock-in amplifier, the chopper speed and the voltage bias of the measurement. A larger time constant helps to decrease the error of the measurement, but it will also extend the measurement time.

The most important part of the setup is the lock-in amplifier, which is used to measure the voltage drop over a shunt resistor, where the current generated by the solar cell passes through. This is a device that can isolate a low-amplitude signal on a given frequency from a noisy input signal. This is particularly important to find the response of the solar cell to the chopped monochromator light and filter it from the response of the cell to surrounding light and bias illumination.

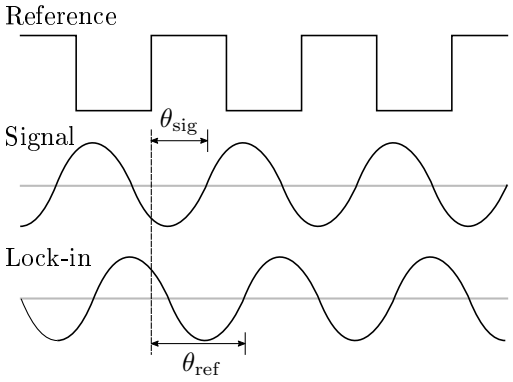

Figure 3.5: Method of Phase-Sensitive Detection with a lock-in amplifier in order to distinguish a signal at a specific frequency from a noisy signal, adapted from [49].

It requires the input of a reference signal with a given frequency, see figure 3.5, in this case the block-wave signal of the chopper wheel with a frequency of 123 Hz. This block-wave is internally transformed into a sinusoidal signal (Lock-in) with the same frequency. By multiplying the noisy measurement signal with this sinusoidal Lock-in signal, it is possible to retrieve the signal from the noise [49]:

$$\begin{aligned} V_{\text{out}} =& V_{\text{sig}} V_{\text{lock}} \sin\left(\omega_{\text{ref}} t + \theta_{\text{sig}}\right) \sin\left(\omega_{\text{lock}} t + \theta_{\text{ref}}\right) \\ =& \tfrac{1}{2} V_{\text{sig}} V_{\text{lock}} \cos\left(\left[\omega_{\text{ref}} - \omega_{\text{lock}}\right] t + \theta_{\text{sig}} - \theta_{\text{ref}}\right) - \\ & \tfrac{1}{2} V_{\text{sig}} V_{\text{lock}} \cos\left(\left[\omega_{\text{ref}} + \omega_{\text{lock}}\right] t + \theta_{\text{sig}} + \theta_{\text{ref}}\right) \end{aligned} \tag{3.2.5}$$

These signals are all AC, except for the signal with $\omega_{\text{ref}} = \omega_{\text{lock}}$. This is the only DC signal that is formed in this multiplication. By leading the output signal through a low-pass filter, only this DC signal will pass:

$$V_{\text{out}} = \tfrac{1}{2} V_{\text{sig}} V_{\text{lock}} \cos\left(\theta_{\text{sig}} - \theta_{\text{ref}}\right), \tag{3.2.6}$$

which is a DC signal proportional to the amplitude of the input signal. All the noise will thus be filtered out, which makes it possible to retrieve very low amplitude signals from a noisy input. This principle is called Phase-Sensitive Detection [49].

3.3 Solar cell device structures

The ultimate goal of this project was to monitor the behaviour of the voltage at the tunnel recombination junction (TRJ) of a monolithic tandem solar cell. This required an adjustment to the basic tandem solar cell structure by incorporating a conductive layer between the top and bottom cell. Solar cells with this feature are usually called 'three-terminal' devices. Micromorph tandem cells with the following layered structures were deposited in superstrate on textured Corning® Eagle XG glass:

AZO / p-µc-Si:H / p-µc-SiO_x:H / i-a-Si:H / n-a-Si:H / n-µc-Si:H / p-µc-SiO_x:H / i-µc-SiO_x:H / i-µc-Si:H / n-SiO_x:H

A special designed shadow mask allowed for a deposition of aluminium-doped zinc oxide (AZO) between the TRJ (n-µc-Si:H) and the *p*-layer of the bottom cell (p-µc-SiO_x:H). This layer serves as the third terminal.

AZO / p-µc-Si:H / p-µc-SiO_x:H / i-a-Si:H / n-a-Si:H / n-µc-Si:H / **AZO** / p-µc-SiO_x:H / i-µc-SiO_x:H / i-µc-Si:H / n-SiO_x:H

The back reflector of each cell consists of three metals, silver, chromium and aluminium, with a thickness of 300 nm, 30 nm and 800 nm, respectively. Figure 3.6 graphically shows the tandem and three-terminal structures that are used for this study.

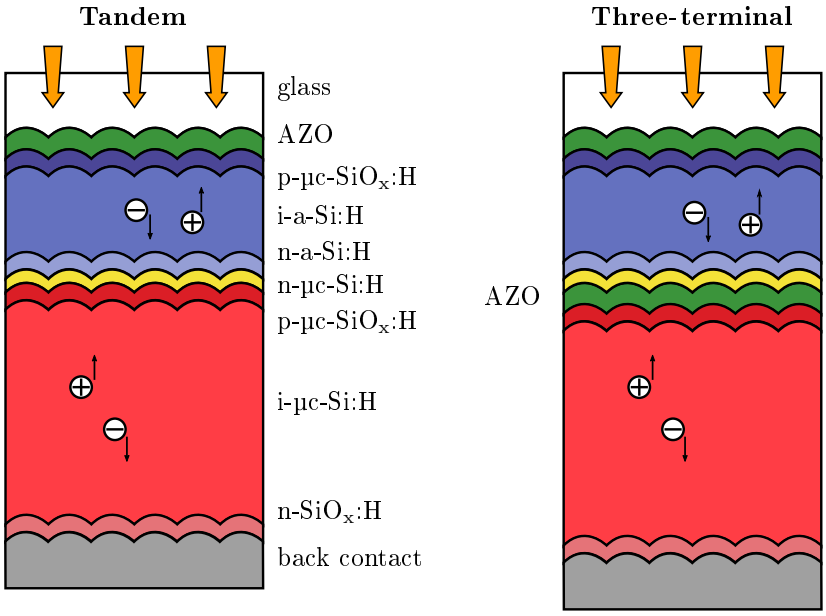

Figure 3.6: Micromorph tandem and three-terminal structures deposited on AZO assisted textured glass. The thickness of the layers are not to scale.

This section will further describe the fabrication processes of the substrate, the PV active layers, the third-terminal and the metal contacts.

3.3.1 Substrate preparation

Substrates for thin-film solar cells often include textured surfaces that enhance light scattering. A frequently used type of glass substrate is Asahi U-type, which features a

pyramidal textured SnO_2:F transparent conductive oxide (TCO) layer. The tips of these pyramids are sharp and the feature size is relatively small, in the order of a few hundred nanometres [50]. While this is ideal for most of the thin-film devices, it is also known to cause cracks and shunts in thicker microcrystalline silicon cells [21, 51]. The three-terminal cells deposited on Asahi U-type showed a decrease in shunt resistance, which was most probably caused by shunts being interconnected by the lateral conductive third terminal. Shunts in the top cell and bottom cell normally only interconnect if they are located very close to each other. It was therefore decided to use a substrate with a smooth and large feature size texturing, with round features rather than pyramids, to reduce particularly the number of shunts in the µc-Si:H bottom cell.

AZO Induced glass Texturing (ZIT), a glass texturing process developed at Delft University of Technology [20], was adopted to make substrates with these properties. The process is based on inhomogeneous wet-etching of a sacrificial ZnO:Al layer with a solution of HF and HNO_3. Detailed information of this process and atomic force microscope pictures of the obtained textured glass can be found in the work of G. Yang [20].

Corning® Eagle XG glass was first cut into pieces of 25 by 100 mm, after which they were thoroughly cleaned in an ultrasonic bath with acetone and isopropanol. The sacrificial AZO layer was deposited with magnetron sputtering (described in section 3.1.2) at a heater temperature of 400 °C and a power of 400 W. The layer was then completely removed by wet-etching in a solution of HF and HNO_3 with a concentration ratio of $[HF]/[HNO_3] = 0.58$. This ratio was chosen after etching with a series of concentration ratios and examining the feature size and distribution. The feature size of the glass texturing was in the order of 10 µm. The AZO front TCO was deposited after another thorough cleaning of the textured glass in the ultrasonic bath.

3.3.2 Third terminal fabrication

Micromorph tandem cells were prepared for this project with a specially designed mask to make conventional and three-terminal solar cells on the same substrate at the same time. This allows for close comparison between the two types of cells and determination of the influence of the third terminal. The mask was designed for solar cells with an area of 16 mm^2, deposited in sets of 30 on a substrate size of 25 by 100 mm. It was designed to have 15 conventional cells and 15 cells with an intermediate conductive layer, of which 10 actually have a contact point. A second mask was designed to position small metal contacts on the middle contact leads.

The middle contact material must be conductive and as transparent as possible, since absorption of light in this layer is a parasitic loss and would thereby influence the performance of the tandem cell. The first material we investigated was indium tin oxide (ITO), chosen for its very high conductivity [52]. A thin layer of ITO, approximately 50 nm, would be sufficient to reach a high enough level of conductivity for the purpose of the contact. After fabrication of the devices, however, the performance of the tandem cells was very poor. The *JV* curve had an S-shape with an approximate voltage barrier of 0.9 V which is shown in figure 3.8. This barrier was most likely caused by band misalignment with the high workfunction of the ITO layer, causing a voltage barrier against the collection of charge carriers [53]. The solution was found by changing to a different TCO material. AZO has proven itself to work as intermediate reflector in micromorph tandem cells [23, 54], while at the same time having an acceptable conductivity. The work

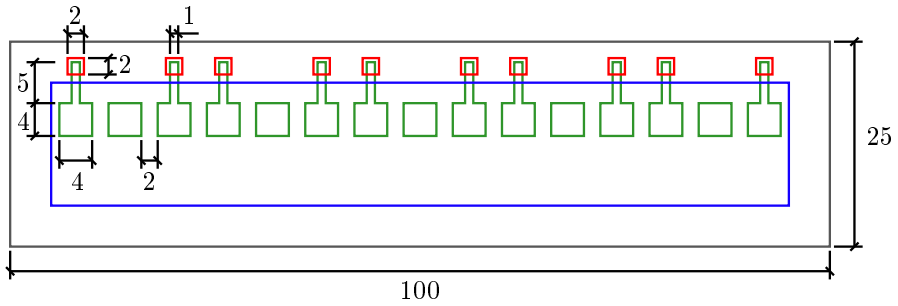

Figure 3.7: Schematic of the intermediate contact shadow masks, marking areas for the middle contacts itself (green), the metal contact mask (red) and the existing mask for depositing any subsequent layers protecting the contact points (blue). Scales in mm.

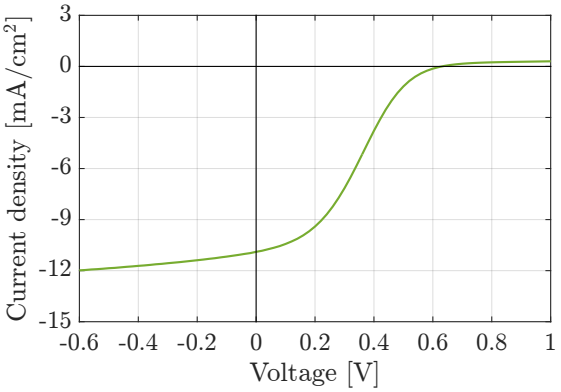

Figure 3.8: S-shaped illuminated JV curve of a tandem cell with intermediate ITO layer.

function of AZO is significantly lower, at 4.1 eV [55], which is why we expected to reduce the voltage barrier. On top of that a thin n-µc-Si:H layer ($\sim$ 6 nm) was included in the structure to serve as a dedicated tunnel recombination junction. This layer was deposited on the a-Si:H top cell before the AZO layer was sputtered, such that it helps to protect the top cell from being damaged by the sputtering process.

For the sputtering process, the heater temperature in the sputtering chamber was decreased to 250 °C with a power density of 1.39 W cm^{-2}, which is halve the power that is used for the front contact. These settings were chosen after a series of test depositions in order to reduce the amount of damage to the samples and still have an acceptable level of conductivity. Aiming for a thickness of 200 nm, the sheet resistance was determined with the 4-point probe to be 46.2 Ω/□.

The AZO layer reflects light back to the a-Si:H cell, the thickness of the a-Si:H top cell can therefore be reduced. Since each sample contains cells including the intermediate contact and normal tandem cells, the thickness of the µc-Si:H bottom cell cannot assure a current-matched cell for both. To overcome this problem a range of cells with different bottom cell thickness was prepared. Approximate thicknesses for each layer were modelled with optical simulations based on GENPRO4. It takes into account the wavelength dependent refractive index and extinction coefficient of every optical layer, as well as the interface roughness and layer thickness. Predicted light absorption in the intrinsic layers

was matched by iteratively changing the thickness of the µc-Si:H bottom cell.

3.3.3 Deposition details

Front TCOs were sputtered at a heater temperature of 400 °C to have the best possible crystallisation and conductivity. The deposition time was set to 3600 s to aim for a thickness of 800 nm. Chamber pressure and deposition power density were set to 2.5 µbar and 2.78 W cm^{-2} respectively. An aluminium bar with a thickness of 500 nm was used as front contact, condensed with a deposition rate of 1 nm s^{-1} with E-beam PVD.

The amorphous and microcrystalline layers were deposited with rf-PECVD in AMIGO, deposition parameters can be found in table 3.1. The thickness of the bottom cell absorber layer (i-µc-Si:H) was varied to find the optimal current-matching of a three-terminal solar cell.

Table 3.1: Deposition parameters used for the intrinsic and doped amorphous and microcrystalline silicon layers with rf-PECVD.

Layer	Heater Temp. [°C]	Power [mW cm^{-2}]	Pressure [mbar]	Process gases	Aimed thickness [nm]
p-µc-Si:H	300	243	2.2	SiH_4, B_2H_6, H_2	4-6
p-µc-SiO_x:H	300	76.4	2.2	SiH_4, B_2H_6, H_2, CO_2	10
i-a-Si:H	200	21.5	0.7	SiH_4	200
n-a-Si:H	300	27.8	0.6	SiH_4, PH_3	20
n-µc-Si:H	300	69.4	1.5	SiH_4, PH_3, H_2	6
p-µc-SiO_x:H	300	76.4	2.2	SiH_4, B_2H_6, H_2, CO_2	15
i-µc-SiO_x:H	300	76.4	2.2	SiH_4, H_2, CO_2	4
i-µc-Si:H seed	170	278	4.0	SiH_4, H_2	50-150
i-µc-Si:H	170	278	4.0	SiH_4, H_2	varying
n-SiO_x:H	300	55.6	1.5	SiH_4, PH_3, H_2, CO_2	60

The back contact was composed of three layers, first 300 nm of silver, secondly 30 nm of chromium and finally 800 nm of aluminium. All metals were condensed with a deposition rate of 1 nm s^{-1} using PVD. The obtained substrates with solar cells looked like the example in figure 3.9. Each strip of tandem cells consisted of 15 normal tandem cells, 10 three-terminal tandem cells and 5 cells with just the middle AZO layer.

In this project several *n*-type doped silicon layers were removed with the plasma etcher, since they can significantly contribute to lateral current collection for dark *JV* measurements. This was explained in section (2.2.2).

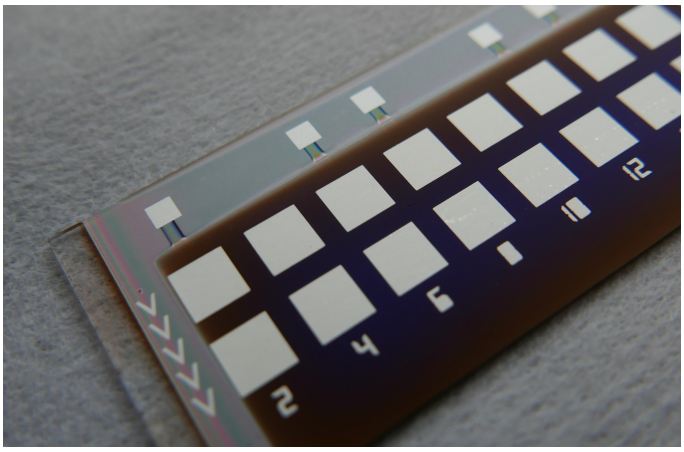

Figure 3.9: Photograph of normal and three-terminal micromorph tandem cells on a microtextured glass substrate.

4 | Results and Discussion

The results and discussion section will present the outcome of measurements and elaborate on the obtained insights and figures from this study. Detailed characterisation of a closely current-matched three-terminal cell will be performed by looking at dark current-voltage measurements over a range of temperatures. Results for the individual junctions of the three-terminal solar cell will be compared with single-junction devices with the same process and deposition parameters. The ideality factor, dark saturation current density and activation energy will be determined for each three-terminal subcell, single-junction cell and micromorph tandem cell, giving insight in the temperature dependence of the recombination current of the micromorph tandem cell. Secondly, the performance of tandem and three-terminal solar cells with the same absorber layer thickness is compared through EQE and light JV, in order to assess the influence of the middle contact. It will be discussed that the middle AZO contact resulted in characterisation difficulties. Some suggestions will be given to improve the three-terminal solar cell design.

For convenience, the different types of solar cell structures will be referred to as: three-terminal (3t) tandem (including a middle AZO contact), 3t subcells (measured through the middle AZO contact), normal tandem (without middle AZO contact), and single-junction (sj) cells.

4.1 Dark JV

The measurement of dark current-voltage characteristics is a widely used method to characterise the electrical performance of solar cells in dark conditions. This section will elaborate on the results obtained with dark JV measurements at different temperatures. The subcells of the 3t tandem cell will be characterised through the middle contact and be compared with sj devices. Following the detailed study of Sturiale *et al.* [39], the experimental results on subcell measurements and three-terminal measurements will be evaluated. The voltage distribution over the a-Si:H and µc-Si:H subcell will be investigated for multiple measurement temperatures and compared with the distribution found in computer simulations as shown by Sturiale *et al.*. This will ultimately give insight in the temperature effect on the electrical performance of the subcells and on the tandem solar cell while measuring dark JV characteristics.

4.1.1 Amorphous silicon

This section will discuss the basic characterisation methods on dark JV measurements of a sj a-Si:H cell and a 3t a-Si:H top subcell with the same intrinsic layer thickness. Differences in the deposition process between the two cells can be found only at the back contact. The sj cell has a standard metal back contact with an area of $16\,\mathrm{mm}^2$. The n-layer was removed with reactive ion etching (RIE) to reduce current spreading in the peripheral of the back contact. The generated current of the 3t top subcell was collected through the middle AZO contact with an area of $23\,\mathrm{mm}^2$. The obtained current density values were corrected to the standard test solar cell area of $16\,\mathrm{mm}^2$. In this case, n-layer removal was not possible since it is covered underneath the 3t bottom subcell. Current spreading

is therefore expected to show up in the measurements, making it more complicated to characterise with good accuracy [31].

Dark JV curves of the sj a-Si:H cell with an intrinsic layer thickness of 200 nm are shown in figure 4.1 (a). Measurements were taken over a voltage range of 1.0 V to −1.0 V, starting at the highest positive value. The reverse bias characteristics will not be discussed in this study, but figures can be found in appendix (6.1). Each measurement was repeated at different temperatures over a range of 100 °C to 30 °C in steps of 10 °C, starting with the highest temperature. Figure 4.1 (a) includes least squares fits to the single diode equation in the exponential region of the curve, see figure 2.4, which is indicated by the vertical dashed lines at 0.20 V and 0.60 V.

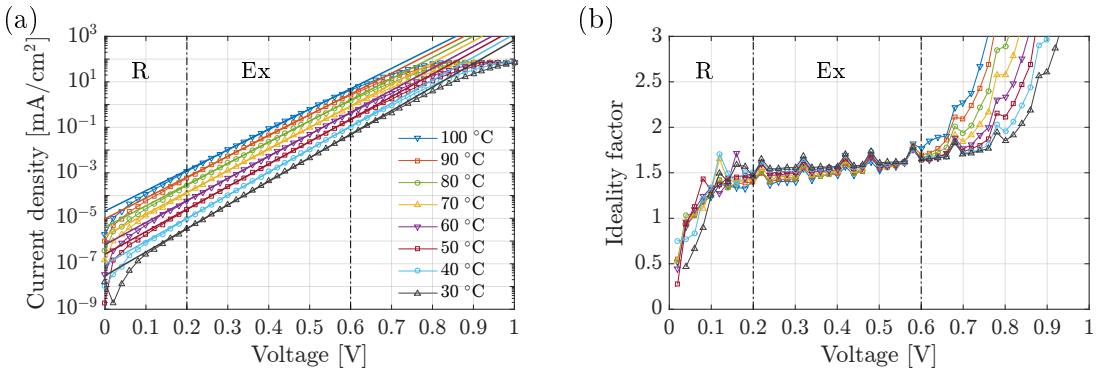

Figure 4.1: Dark current-voltage curves for a sj a-Si:H cell with an intrinsic layer thickness of 200 nm, measured at different temperatures (a). The fitting interval to the exponential region (Ex) of each curve is located between vertical dashed lines, the region indicated with R is controlled by recombination. Figure (b) shows the voltage-dependent ideality factors calculated from the dark JV curves in (a).

Figure 4.1 (b) shows the voltage dependent ideality factor, calculated with equation (2.2.7). In the exponential region (Ex), it increases slightly until $V = 0.60$ V, after which it increases rapidly. For an even higher forward voltage the temperature dependence of the ideality factor becomes significant, which is in agreement with the results reported by van Swaaij *et al.* [29]. The concentration of active recombination centres is therefore assumed to be constant with temperature for the low forward voltage region.

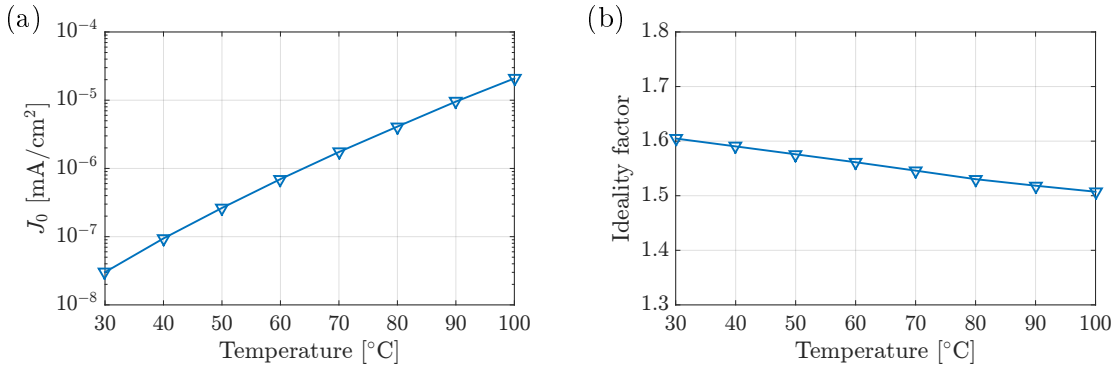

Figure 4.2: Dark saturation current density (a) and ideality factor (b) versus temperature for a sj a-Si:H cell with an intrinsic layer thickness of 200 nm.

The dark saturation current density J_0 obtained from the least-squares fits to the

measurement curves as a function of temperature, see equation (2.2.3) is shown in figure 4.2 (a). An exponential increase with temperature is observed, which is in agreement with the trend reported by Kind *et al.* [56]. While the temperature increases with 70 °C, J_0 will increase over three orders of magnitude. Ideality factors obtained from the same fits show a slight decrease with temperature, also in agreement with [15].

Activation energy as a function of voltage can be derived from the dark JV curves by fitting the current density for various temperatures at a specific applied voltage to the Arrhenius equation. Following equation (2.2.10) the obtained curve in figure 4.3 should have a linear dependency on voltage, which in turn can be used to calculate the mobility gap of the solar cell. For the sj a-Si:H cell this mobility gap was determined at 1.70 ± 0.01 eV, using a thermal ideality factor of 2 which was validated by Kind *et al.* [15]. Note that the derivation of the standard deviations of the mobility energy gaps can be found in appendix 6.2.

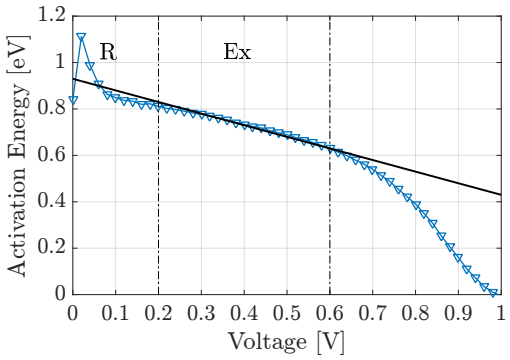

Figure 4.3: Voltage dependent activation energy of the sj a-Si:H solar cell, including a least-squares fit to obtain the mobility gap $E_{\mathrm{mob}} = 1.70 \pm 0.01$ eV.

Characterisation of the three-terminal a-Si:H top subcell proved to be more complicated. The low forward voltage region was heavily affected by current spreading (CS). For the lowest temperature of 30 °C this effect is visible up to a voltage of 0.40 V. As was discussed in section (2.2.2), measurements at a higher temperature are less influenced by current spreading since the generated current is approximately two orders of magnitude larger. This becomes particularly clear when looking at the voltage-dependent ideality factor in figure 4.4 (b). The large peak in ideality factor between 0 and 0.50 V is caused by current spreading, the effect being larger on the lowest temperature curve.

In the higher forward voltage region in figure 4.4 (a), we observe a slowly levelling off current. This can be attributed to the increased series resistance caused by the middle AZO layer, which will be discussed in section 4.2. The measurement curve at the highest temperature is most influenced, where the exponential region stops at a voltage as low as 0.50 V. This confirms that there is indeed an increased resistance, since lower temperature curves will reach the same current level at a higher applied voltage. Looking at figure 4.4 (b) in comparison with the sj a-Si:H cell (figure 4.1 (b)), where the voltage-dependent ideality factor rapidly increases in the higher voltage region, we now observe a gradually increasing ideality factor.

Both the current spreading effect and the slowly levelling-off current density made it impossible to define a reasonably large voltage region where each dark JV curve shows exponential behaviour. It was therefore decided to define such a voltage region for each

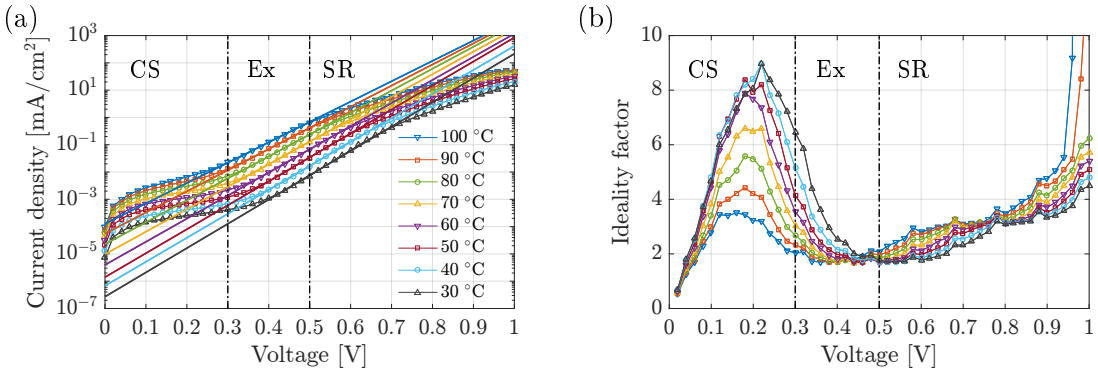

Figure 4.4: Dark current-voltage curves for a 3t a-Si:H top subcell with an intrinsic layer thickness of 200 nm measured at different temperatures (a). Least-squares fits to the single diode equation are included as straight lines with shifting voltage region for each measurement temperature. The fitting interval for the 100 °C curve is included between vertical dashed lines and indicated with Ex (exponential). The regions influenced by current spreading (CS) and series resistance (SR) are also indicated for the highest temperature curve. Figure (b) shows the voltage-dependent ideality factors calculated from the dark JV curves in (a). Note that the y-axis limits of both figures (a) and (b) are chosen differently than for the sj a-Si:H cell.

measurement temperature curve, such that a good least-squares fit to the single diode equation to the exponential region of each curve could be achieved. The exponential region of the dark JV curve translates to a quite stable value for the voltage-dependent ideality factor, whereas the areas influenced by current spreading (CS) and series resistance (SR) show a varying value, which can be observed in figure 4.4 (b). This can be used as a guideline to choose the correct voltage region for each measurement temperature.

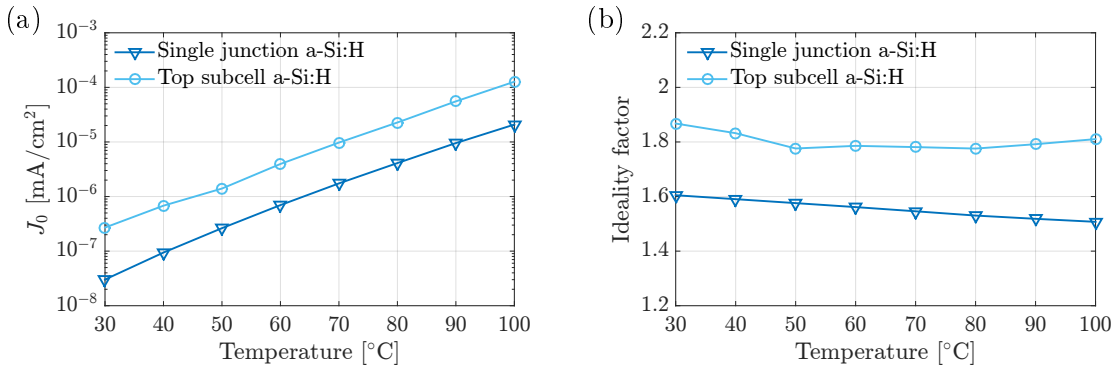

Figure 4.5: Dark saturation current density (a) and ideality factor (b) versus temperature for a 3t a-Si:H top subcell with an intrinsic layer thickness of 200 nm. Both figures include the sj a-Si:H cell curve from figure 4.2.

The dark saturation current density obtained from these least-squares fits to the measurement curves as a function of temperature is shown in figure 4.5 (a). It shows again an exponential increase with temperature. However, in comparison with the sj a-Si:H cell it is one order of magnitude higher over the full temperature range. The ideality factors obtained from the same fits in figure 4.5 (b) show a value close to 1.8, which is also high compared to the single-junction cell.

The voltage-dependent activation energy of the 3t a-Si:H top subcell was also largely

influenced by the above mentioned effects. The linear dependence on voltage will only be visible when the voltage region with exponential behaviour overlaps for each measurement temperature. Given that in the first place this region shrunk to a width of approximately 0.20 V and in the second place this region shifts towards a higher forward voltage for lower measurement temperatures, there is no wide region where each curve shows exponential behaviour. Between 0.44 V and 0.50 V there is a very narrow region of four data points that can be fit to equation (2.2.10) with a least squares function, however this will not lead to a very reliable value for the mobility gap. As a comparison the least squares fit to the activation energy curve of the sj a-Si:H cell is included in figure 4.6.

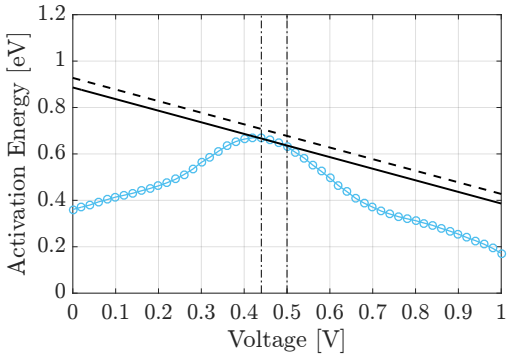

Figure 4.6: Voltage dependent activation energy of the 3t a-Si:H top subcell, including a least-squares fit to obtain the mobility gap $E_{\mathrm{mob}} = 1.62 \pm 0.02\,\mathrm{eV}$ (solid line) and the activation energy fit of the sj a-Si:H cell with $E_{\mathrm{mob}} = 1.70 \pm 0.01\,\mathrm{eV}$ (dashed line).

The mobility gap value of the 3t a-Si:H top subcell is significantly lower than the sj a-Si:H cell. We came up with two possible explanations for this observation. The first explanation is that the obtained mobility gap of the 3t a-Si:H top subcell is influenced by the measurement method, since the activation energy obtained from the dark JV curve measurements is lowered on both sides of the fitting interval. It is not unlikely that the values in the fitting interval are still affected by either current spreading or the increased series resistance by the middle AZO contact. Figure 4.16 (a) in section 4.1.3 confirms that the dark JV measurement curves of the 3t a-Si:H top subcell are influenced by series resistance. It shows that pseudo JV curves could be used to obtain the mobility energy gap free from series resistance effects. Unfortunately, these measurements were only performed at two different temperatures.

The other explanation that we propose is that further process steps on the three-terminal cell, for instance the sputtering process of the middle AZO contact and deposition of the µc-Si:H bottom cell, changed the material properties of the 3t a-Si:H top subcell. The sj a-Si:H cell and the 3t top subcell were both deposited in a single run, i.e. the glass subtrate strips for the cells were in the same substrate holder during the top cell deposition run.

The vacuum break to place the middle contact mask, possible sputtering damage and thermal annealing are potential causes for a change in material properties of the 3t a-Si:H top subcell. Especially thermal annealing of i-a-Si:H layers can influence the optical and mobility gap by effusion of hydrogen, increasing the dangling bond density [57]. This could also explain the observed increase in dark saturation current density for the 3t a-Si:H top subcell in figure 4.5 (a), and the increase of ideality factor in figure 4.5 (b). The recom-

bination profile shifts towards the bulk intrinsic material with increased dangling bond density [12], which ultimately results in an increased ideality factor and dark saturation current density.

4.1.2 Microcrystalline silicon

For the sj µc-Si:H cell with an intrinsic layer thickness of 2500 nm, the dark JV curves at different temperatures including least-squares fits to the single diode equation are shown in figure 4.7 (a). Measurements were taken over a voltage range of 0.70 V to −1.0 V in steps of 0.020 V, starting at the highest positive value, and were repeated at different temperatures over a range of 100 °C to 30 °C in steps of 10 °C, starting at the highest temperature.

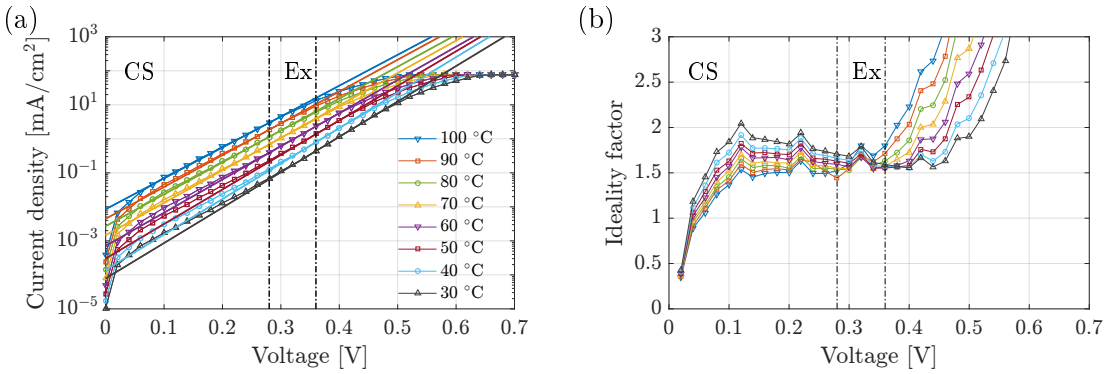

Figure 4.7: Dark current-voltage curves for a sj µc-Si:H cell with an intrinsic layer thickness of 2500 nm measured at different temperatures (a). The overlap of exponential regions (Ex) for each temperature is indicated between vertical dashed lines. Current spreading (CS) is indicated in the low forward voltage region. Least-squares fits to the single diode equation are included as straight lines. Figure (b) shows the voltage-dependent ideality factors calculated from the dark JV curves in (a).

In the low forward voltage region, lower temperature curves show a slight current spreading up to a voltage of 0.28 V for the lowest temperature curve. The voltage-dependent ideality factor is shown in figure 4.7 (b). Again the effect of current spreading is clearly visible in the low forward voltage region. If the n-layer was removed completely with RIE, lateral current collection would have to occur through the intrinsic µc-Si:H material. This material has a significantly higher dark conductivity than i-a-Si:H, since the crystalline volume fraction in the amorphous material that forms µc-Si:H will increase the electron and hole mobilities, μ_n and μ_p [58]. The dark conductivity of the material will thereby also increase following equation 4.1.1:

$$\sigma_D = e(n_0\mu_n + p_0\mu_p) \tag{4.1.1}$$

Reported values for the dark conductivity of i-µc-Si:H are in the order of $1 \cdot 10^{-8}\,\mathrm{S\,cm^{-1}}$ to $1 \cdot 10^{-6}\,\mathrm{S\,cm^{-1}}$. In comparison, the dark conductivity of a-Si:H is in the order of $1 \cdot 10^{-10}\,\mathrm{S\,cm^{-1}}$ and of n-SiO_x:H it is $1 \cdot 10^{-2}\,\mathrm{S\,cm^{-1}}$. We therefore conclude that the observed current spreading can not be caused by the i-µc-Si:H layer, the n-SiO_x:H layer is therefore assumed to not be removed completely.

The highest temperature curve of the voltage-dependent ideality factor, which is least affected by current spreading, shows a similar shape as the sj a-Si:H cell in figure 4.1

(b). It shows a gradually increasing ideality factor, up to a voltage of 0.36 V where it rapidly increases. Similar to the sj a-Si:H cell, the concentration of active recombination centres is therefore assumed to be constant with temperature for the low forward voltage region. From this figure we can also tell that the least-squares fit to the dark JV curve should have a different voltage range for each temperature measurement. The temperature dependency of the dark saturation current density and the ideality factor obtained from the least-squares fits is shown in figure 4.8.

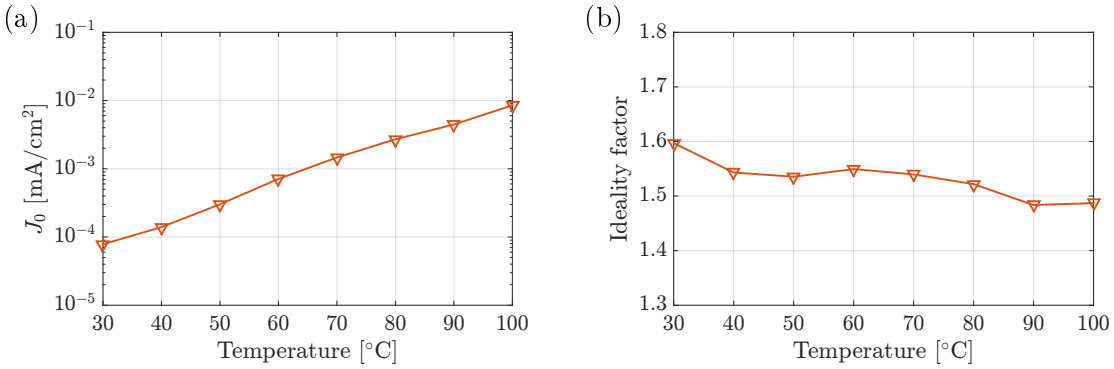

Figure 4.8: Dark saturation current density (a) and ideality factor (b) versus temperature for a sj µc-Si:H cell with an intrinsic layer thickness of 2500 nm.

Similar to the a-Si:H cells, there is an exponential increase with temperature visible for the dark saturation current density. The value increases roughly two orders of magnitude over the measured temperature range of 70 °C. The ideality factor decreases only slightly with temperature. The value between 1.6 and 1.5 is an indication that the recombination at the p/i- or i/n interfaces is dominant, rather than bulk recombination in the i-layer [12].

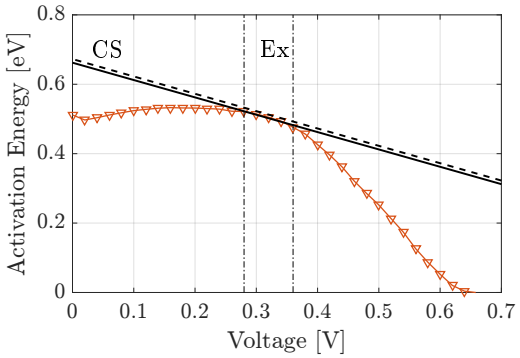

Figure 4.9: Voltage-dependent activation energy of the sj µc-Si:H solar cell, including a least-squares fit to obtain the mobility gap of $E_{\mathrm{mob}} = 1.17 \pm 0.01$ eV (solid line). The figure includes the activation energy fit with a mobility gap value of $E_{\mathrm{mob}} = 1.19$ eV (dashed line) as found by Pieters *et al.* [22].

Activation energy as a function of voltage was again derived from the dark JV curves by fitting the current density for various temperatures at a specific applied voltage to equation (2.2.8). For the sj µc-Si:H cell the mobility gap obtained with equation (2.2.10) was determined at 1.17 ± 0.01 eV, using a thermal ideality factor of 2 which was validated by Pieters *et al.* [22]. This mobility gap is only marginally smaller than the determined value

of 1.19 eV by Pieters *et al.* [22]. The fit with this value is also included as a dashed line in figure 4.9. The voltage region where each dark *JV* curve shows exponential behaviour is limited to 0.28 V to 0.36 V due to current spreading in the low forward voltage region and current limitation by the measurement setup in the high forward voltage region.

In contrast to the 3t a-Si:H top subcell, characterisation of the 3t µc-Si:H bottom subcell was more straightforward. There is no current spreading possible since the front contact area is restricted, which is visualised in figure 4.10. Current spreading at the back

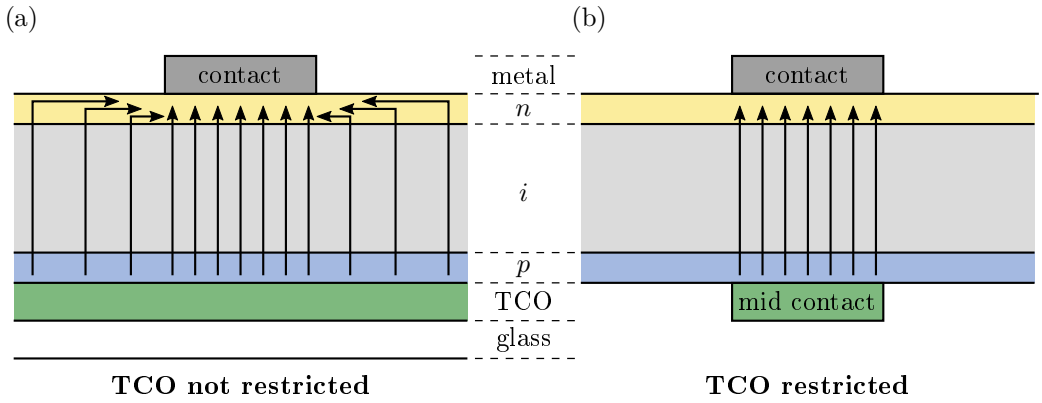

Figure 4.10: (a) Current spreading effect by lateral conduction through *n*-layer, (b) Restricted front TCO area prevents current spreading effect. Adapted from [31].

contact of a *p-i-n* solar cell can only occur if the front contact is not limiting the active surface area of the cell, i.e. when the entire front TCO acts as an equipotential surface. In this particular three-terminal structure however, the middle contact, which acts as front contact for the bottom subcell measurements, has a restricted surface area. Therefore the active surface area of the bottom subcell cannot be increased further than the front contact area by current spreading through the *n*-layer at the back contact. On the other hand, the effect of the high series resistance of the middle contact can be observed in the higher forward voltage region, which is visible in figure 4.11 (a).

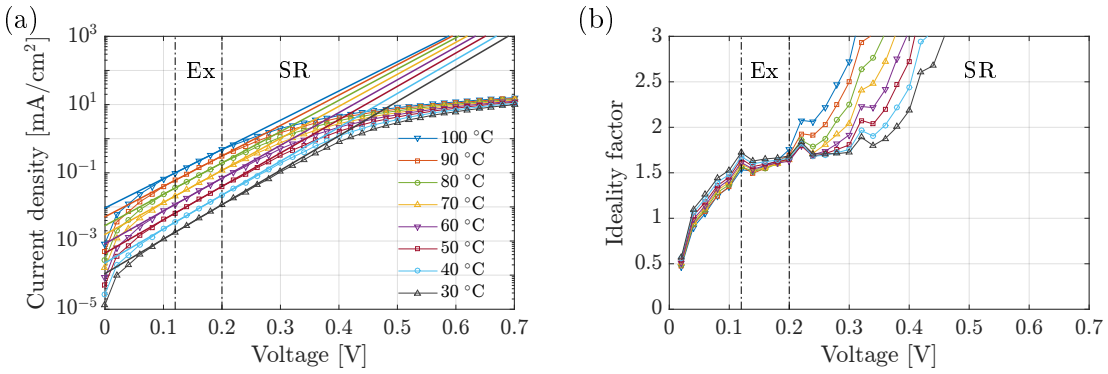

Figure 4.11: Dark current-voltage curves for a 3t µc-Si:H bottom subcell with an intrinsic layer thickness of 2500 nm measured at different temperatures (a). Least-squares fits to the single diode equation in the exponential region (Ex) are included as straight lines. The region influenced by series resistance (SR) is indicated. Figure (b) shows the voltage-dependent ideality factor calculated from the dark *JV* curves in (a).

Figure 4.11 (b) confirms that the 3t µc-Si:H bottom subcell does not suffer from current

spreading. A voltage region can be defined where each dark JV curve shows exponential behaviour, between 0.12 V and 0.20 V. The dark saturation current and ideality factor as a function of temperature are plotted in figure 4.12 together with the values for the sj µc-Si:H cell.

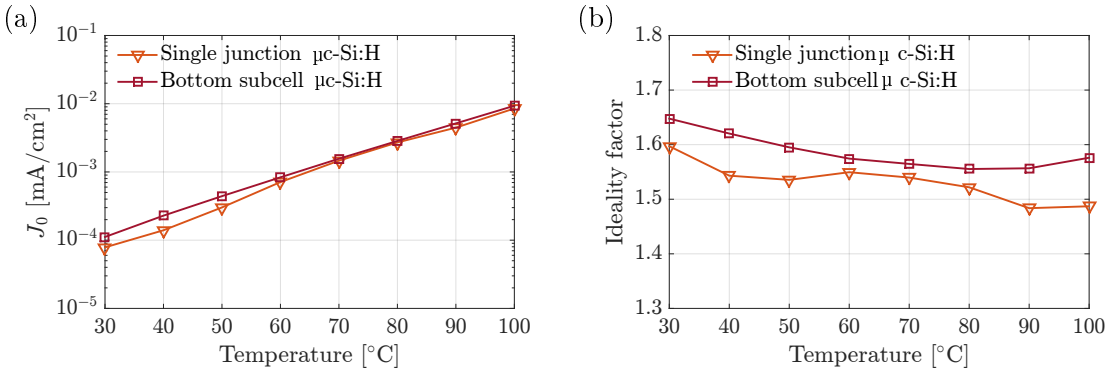

Figure 4.12: Dark saturation current density (a) and ideality factor (b) versus temperature for a 3t µc-Si:H bottom subcell with an intrinsic layer thickness of 2500 nm. Both figures include the sj µc-Si:H cell curve from figure 4.8.

There is a very good overlap of the dark saturation current density between the sj µc-Si:H device and the 3t bottom subcell. On the other hand, the ideality factor of the subcell is found to be higher at every measurement temperature. This would normally indicate that there is more recombination occurring in the intrinsic layer than for the sj cell [12], but in this case it could also be caused by the increased series resistance. A higher R_s increasingly lowers the dark current density for higher applied voltage and therefore the slope of the dark JV curve is shallower. This leads to a larger value for ideality factor obtained from the least-squares fit.

The mobility gap of the 3t µc-Si:H bottom subcell was determined at 1.08 ± 0.01 eV, again using a thermal ideality factor of 2. This mobility gap is significantly smaller than the determined value of 1.19 eV by Pieters *et al.* [22]. The fit with this value is also included as a dashed line in figure 4.13.

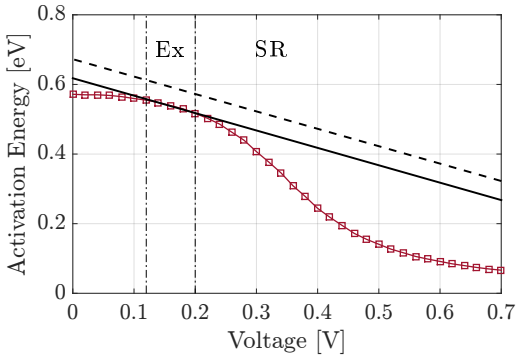

Figure 4.13: Voltage dependent activation energy of the 3t µc-Si:H bottom subcell, including a least-squares fit to obtain the mobility gap energy $E_{mob} = 1.08 \pm 0.01$ eV (solid line) and the activation energy fit with a mobility gap value of $E_{mob} = 1.19$ eV (dashed line) as found by Pieters *et al.* [22].

In contrast with the activation energy curve for the 3t a-Si:H top subcell in figure 4.6, the bottom subcell is not affected by current spreading in the low forward voltage region.

The mobility gap value of 1.08 ± 0.01 eV is significantly lower than the sj µc-Si:H cell, with a mobility gap of 1.17 ± 0.01 eV. Again both cells where processed in the same deposition run. This implies that apart from a measurement error by the increased series resistance, only the substrate morphology could be the origin of the lower observed mobility gap. The crystallinity of the µc-Si:H material is known to depend on substrate morphology [51], which in turn affects the mobility gap. Pieters *et al.* [59] report a mobility gap of 1.07 eV for highly crystalline solar cells.

After removal of the *n*-layer for both the 3t µc-Si:H bottom subcell and the sj µc-Si:H cell with reactive ion etching, the crystallinity of both intrinsic layers was determined with Raman spectroscopy. The crystallinity of the 3t bottom subcell was measured at 62.7 ± 0.5% and the crystallinity of the sj cell was measured at 58.8 ± 1.0 %. This indeed indicates that, although both cells were processed in the same deposition run, the substrate morphology led to an increased crystallinity of the 3t µc-Si:H subcell. However, the difference in crystallinity is not significant enough to explain the obtained decrease in mobility gap [51, 59], since a crystallinity of 62.7% is not reported as highly crystalline [59]. Pseudo *JV* curve measurements could again be used to obtain the mobility gap without influence of series resistance.

4.1.3 Micromorph tandem

For the micromorph three-terminal tandem cell with an a-Si:H intrinsic layer thickness of 200 nm and a µc-Si:H intrinsic layer thickness of 2500 nm, the dark *JV* curves at different temperatures including least-squares fits to the single diode equation are shown in figure 4.14 (a). Measurements were taken over a voltage range of 1.5 V to −1.0 V in steps of 0.020 V, starting at the highest positive value and were repeated at different temperatures over a range of 100 °C to 30 °C in steps of 10 °C, starting at the highest temperature.

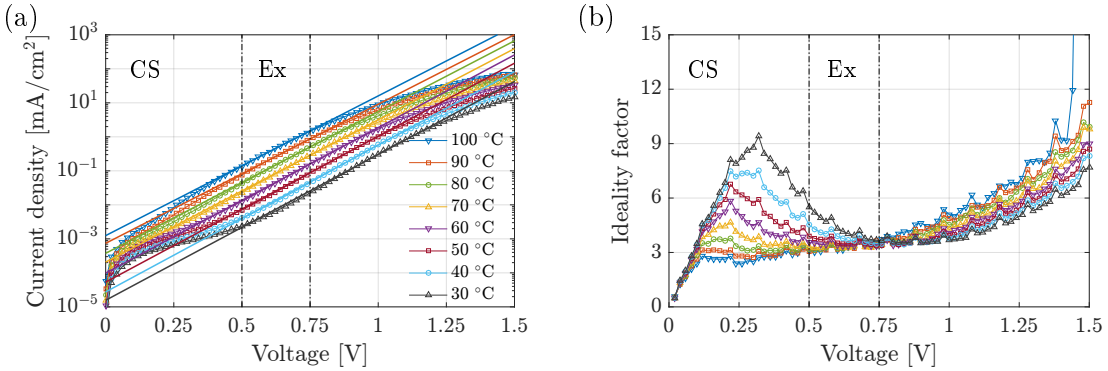

Figure 4.14: Dark current-voltage curves for a 3t micromorph tandem cell with an a-Si:H intrinsic layer thickness of 200 nm and a µc-Si:H intrinsic layer thickness of 2500 nm measured at different temperatures (a). Least-squares fits to the single diode equation are included as straight lines with shifting voltage region for each measurement temperature. The fitting interval for the 100 °C curve is included between vertical dashed lines and indicated with Ex (exponential). The region influenced by current spreading (CS) is also indicated for the highest temperature curve. Figure (b) shows the voltage-dependent ideality factors calculated from the dark *JV* curves in (a).

In the low forward voltage region each curve shows current spreading, up to a voltage of 0.5 V for the lowest temperature curve. Since the *n*-layer at the back contact was removed

with RIE, this effect is caused by the n-type layer of the a-Si:H subcell. The p-layer of the bottom cell is not the source of the current spreading, as it has a much lower conductivity, in the order of $2 \cdot 10^{-4}\,\mathrm{S\,cm^{-1}}$ compared to $2 \cdot 10^{-2}\,\mathrm{S\,cm^{-1}}$ for the n-type a-Si:H layer. The current spreading effect conceals the first exponential region of the tandem dark JV curve, as this is normally controlled by recombination in the bulk of the a-Si:H cell. While AZO can also be used as a mask for reactive ion etching, it might be worth attempting to remove the top subcell n-layer prior to the deposition of the µc-Si:H bottom subcell, at the cost of the normal tandem comparison cells on the same substrate.

In the higher forward voltage region the curves increase more slowly, which could indicate non-ideal operation of the TRJ [31]. In order to sustain the dark current density, the TRJ will have to operate at a reverse bias in an attempt to thermally generate enough e-h pairs. This causes a significant voltage drop over the TRJ and at the same time reduces the voltage drops over each of the subcells.

The voltage-dependent ideality factor is shown in figure 4.14 (b). Again the effect of current spreading is clearly visible in the low forward voltage region. The shape of the curves are comparable to the 3t a-Si:H top subcell curves in figure 4.4 (b) with a gradually increasing voltage-dependent ideality factor in the high forward voltage region and current spreading in the low forward voltage region. From this figure we can also tell that the least-squares fit to the dark JV curve should have a different voltage range for each temperature measurement. The temperature dependency of the dark saturation current density and the ideality factor obtained from the least-squares fits is shown in figure 4.15.

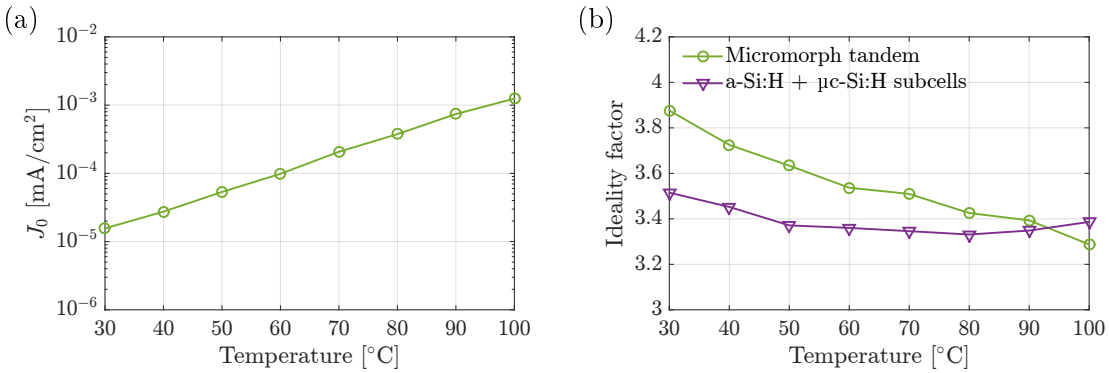

Figure 4.15: Dark saturation current density (a) and ideality factor (b) versus temperature for a 3t micromorph tandem cell with an a-Si:H intrinsic layer thickness of 200 nm and a µc-Si:H intrinsic layer thickness of 2500 nm. The sum of the subcell ideality factors is included in figure (b).

Similar to the a-Si:H and µc-Si:H cells, there is an exponential increase with temperature visible for the dark saturation current density. The value increases roughly two orders of magnitude over the measured temperature range of 70 °C. The ideality factor decreases from approximately 3.91 to 3.34, which is more than expected from the sj cell ideality factors. Sturiale *et al.* [39] states that the ideality factor of a micromorph tandem cell in the second exponential region is equal to the sum of the ideality factors of both subcells. The sum of the subcell a-Si:H and µc-Si:H ideality factors is included in figure 4.15 (b). Given that these ideality factors where indeed derived from the exponential region, it is likely that non-ideal operation of the TRJ and the current spreading effect influenced the ideality factor of the micromorph tandem cell.

Pseudo JV curves are obtained at a temperature of 25 °C with variable intensity measurements (VIM), where the evolution of J_{sc} versus V_{oc} is determined. These curves will resemble the dark JV measurement curves without the influence of series resistance as explained in section (2.2.5). The voltage range of the pseudo JV curves will reach from V_{oc} at almost dark conditions to V_{oc} at AM 1.5. These measurements are taken on the light JV setup, where the samples are illuminated with a solar simulator.

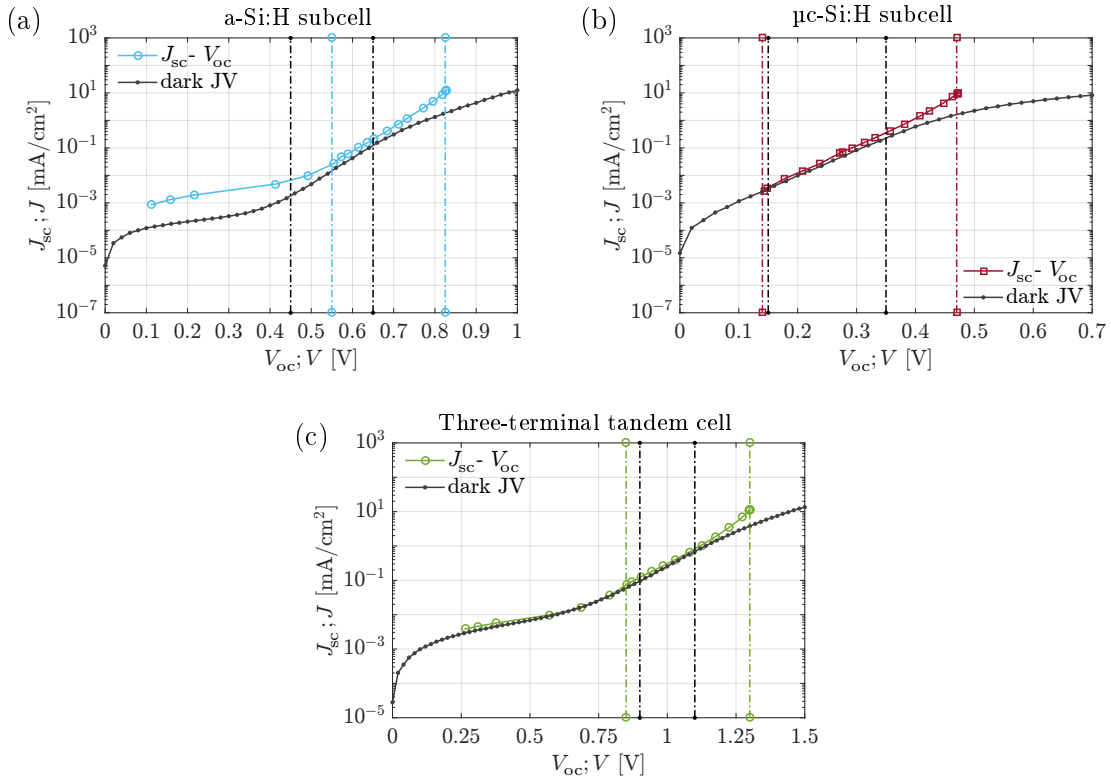

Figure 4.16: Pseudo JV curves compared to dark JV curves measured at $T = 25$ °C of (a) the 3t a-Si:H top subcell, (b) the 3t µc-Si:H bottom subcell and (c) the 3t micromorph tandem cell. Least-squares fits to the single diode equation between the vertical dashed lines for each curve resulted in an ideality factor of (a) 1.79 ± 0.02 and 1.82 ± 0.04, (b) 1.64 ± 0.01 and 1.84 ± 0.04 and (c) 3.51 ± 0.03 and 3.90 ± 0.08 for the pseudo JV curves and dark JV curves respectively.

Similar to the dark JV curves, the exponential region of each pseudo JV curve is fitted to the single diode equation with a least-squares method, resulting in ideality factors that are not influenced by series resistance. A value of 1.79 ± 0.02 is obtained for the 3t a-Si:H top subcell, 1.64 ± 0.01 is obtained for the 3t µc-Si:H bottom subcell and together this adds up to 3.53 ± 0.02. This is indeed very close to the value of 3.51 ± 0.03 obtained for the 3t micromorph tandem cell, which confirms the statement by Sturiale *et al.* that the ideality factor in the second exponential region of the dark JV curve for the micromorph tandem cell, see figure (2.4), is equal to the sum of both subcell ideality factors. The same measurements and analysis was performed on the sj a-Si:H and µc-Si:H cells and the normal micromorph tandem cell, which can be found in appendix 6.4. Here again the ideality factors of the sj cells add up to the ideality factor of the micromorph tandem cell. This result also supports the assumption that the ideality factor of the 3t micromorph tandem cell obtained through dark JV is increased by series resistance, as the ideality factors obtained from the subcell dark JV curves add up to 3.66 ± 0.06 in stead of the

3.90 ± 0.08 obtained from the three-terminal dark JV curve at 25 °C.

Activation energy as a function of voltage was again derived from the dark JV curves by fitting the current density for various temperatures at a specific applied voltage to equation (2.2.8). For the 3t micromorph tandem cell this mobility gap was determined at 1.77 ± 0.01 eV, using a thermal ideality factor of 2. The mobility gap energy of the 3t

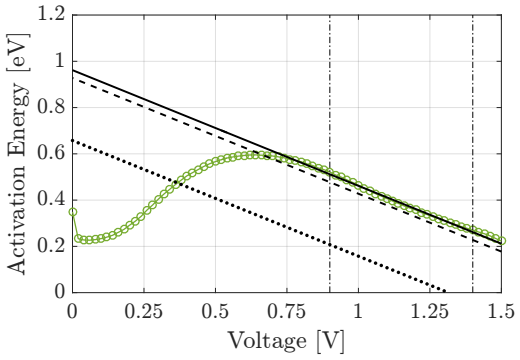

Figure 4.17: Voltage dependent activation energy of the 3t micromorph tandem cell, including a least-squares fit to obtain the mobility gap energy of E_{mob} = 1.77 ± 0.01 eV (solid line). The figure includes the activation energy fit for the sj a-Si:H cell with a mobility gap of E_{mob} = 1.70 ± 0.01 eV (dashed line) and the fit for the sj µc-Si:H cell with a mobility gap of E_{mob} = 1.17 ± 0.01 eV (dotted line).

micromorph tandem cell is very close to the mobility gap of the sj a-Si:H cell of 1.70 ± 0.01 eV, which is plotted as a dashed line in figure 4.17. The dotted line represents the mobility gap of 1.17 ± 0.01 eV for the sj µc-Si:H cell. One could argue that the temperature dependence of the recombination current is therefore dominated by the a-Si:H top subcell rather than the µc-Si:H bottom subcell. However, since the mobility gap is determined in the higher voltage region between 0.90 V and 1.4 V, where a slowly levelling-off current density was observed (figure 4.14), it is more likely that this mobility gap is dominated by the tunnel recombination junction. This is supported by the findings of Willemen *et al.* [31], where a mobility gap for the TRJ between 1.7 and 2.0 eV was used to model light JV curves of a-Si:H based tandem solar cells. Depositing *n-i-p* structures of the TRJ and measuring dark JV curves of these structures could be a method to validate this observation [39].

Voltage distribution of subcells

The distribution of the applied voltage over the a-Si:H and the µc-Si:H subcell will depend on the potential current density that can be generated in each of the cells, where the distribution will be such that the total current density through both of the cells is equal. Sturiale *et al.* determined the voltage drops over the a-Si:H top cell, the µc-Si:H bottom cell and the TRJ with computer simulations [39]. Their result is shown in figure 4.18.

The parameter F_0 originates from the field-dependent effective carrier mobility in the TRJ, where F_0 represents the strength of the field dependence [31, 39]. A strong field dependence will lead to a more reverse biased TRJ, resulting in a significant voltage drop over the TRJ and reduced voltage drops over the top and bottom subcell. This will only

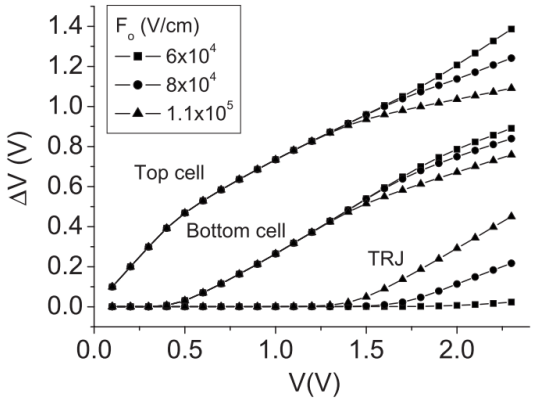

Figure 4.18: Voltage drop ΔV on the top subcell, on the bottom subcell, and on the TRJ of the micromorph tandem cell with respect to the total applied voltage and for different values of the parameter F_0. The intrinsic layer thicknesses are 200 and 1500 nm. The voltage drop on the TRJ is plotted in absolute value [39].

occur at a higher applied voltage where the TRJ should thermally generate more e-h pairs to sustain the dark current density of the micromorph tandem cell.

A larger fraction of the applied voltage will drop over the a-Si:H top subcell. This is caused by the lower conductivity and therefore lower dark current density than the µc-Si:H cell at the same voltage drop. The onset voltage for the µc-Si:H bottom subcell will define the end of the first exponential region of the micromorph tandem dark JV curve, after which the current will be controlled by recombination in both the top and bottom subcell intrinsic layers.

Device temperature will influence the dark JV curve as was demonstrated in previous sections. It is therefore also likely that it will influence the voltage drop profile shown by Sturiale *et al.*, since a-Si:H and µc-Si:H cells both have a different temperature dependency. The voltage drops over the top and bottom subcell could be determined from experimental data of the sj a-Si:H and µc-Si:H cells, which was taken in a smaller applied voltage region than figure (4.18) due to current limitation of the dark JV measurement setup. Exponential interpolation of the current densities was performed to add the voltages of the sj a-Si:H cell and the sj µc-Si:H cell at the same current density to obtain the dark JV curve of a possible tandem cell as the addition of the single-junction cells. Ultimately this can be used to retrieve the voltage drops ΔV as a function of the applied voltage for the "added" tandem cell. Figure 4.19 (b) reveals voltage drops over the top cell and bottom cell, assuming that the voltage drop over the TRJ is not present in this voltage region. The addition of the sj a-Si:H and the sj µc-Si:H cell is shown in figure 4.19 (a.)

As expected from the sj dark JV curves, a micromorph tandem cell curve as the series connection of both a-Si:H and µc-Si:H will show two exponential regions, as defined by Sturiale *et al.*. The first region originates from the a-Si:H cell, where the recombination current is not high enough to cause a voltage drop in the µc-Si:H cell. This exponential region was concealed by current spreading in the measurement of the 3t micromorph tandem cell. The voltage drop ΔV over the a-Si:H top cell will increase equally to the applied voltage in the first exponential region, as there will be no voltage drop over the µc-Si:H bottom cell. The onset voltage for the bottom cell varies with device temperature, for higher temperatures the onset voltage will decrease. This indicates that the increase of

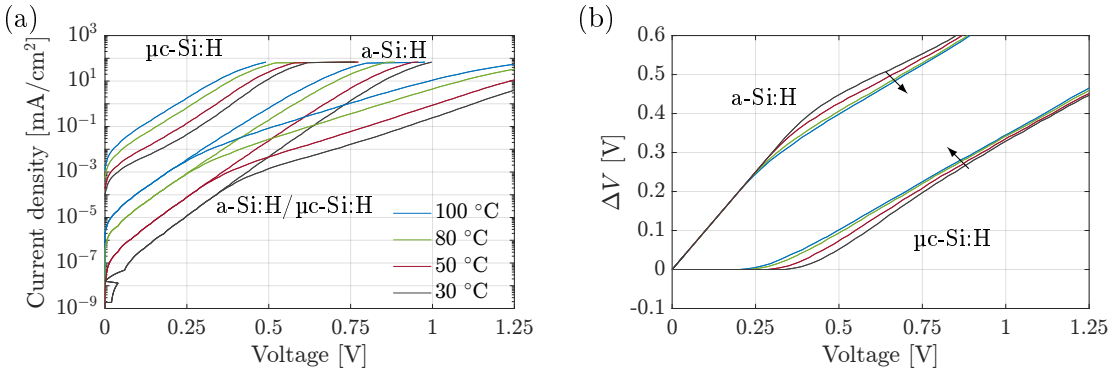

Figure 4.19: (a) The addition of dark JV curves of a sj a-Si:H and µc-Si:H cell, with an intrinsic layer thickness of 200 nm and 2500 nm respectively, by exponential interpolation of the current density. (b) Voltage drop ΔV over the top a-Si:H and bottom µc-Si:H subcell as a function of the tandem cell voltage. Selected temperatures are plotted for clarity, the direction of the arrows indicate increasing measurement temperature.

dark current density as a function of temperature is higher for a-Si:H cells than for µc-Si:H cells in this voltage region. For higher tandem cell voltages, the effect of temperature on the voltage distribution becomes smaller again.

The same analysis was done for the 3t a-Si:H and µc-Si:H subcell curves, measured through the middle AZO contact. Similar to the measured dark JV curves of the 3t

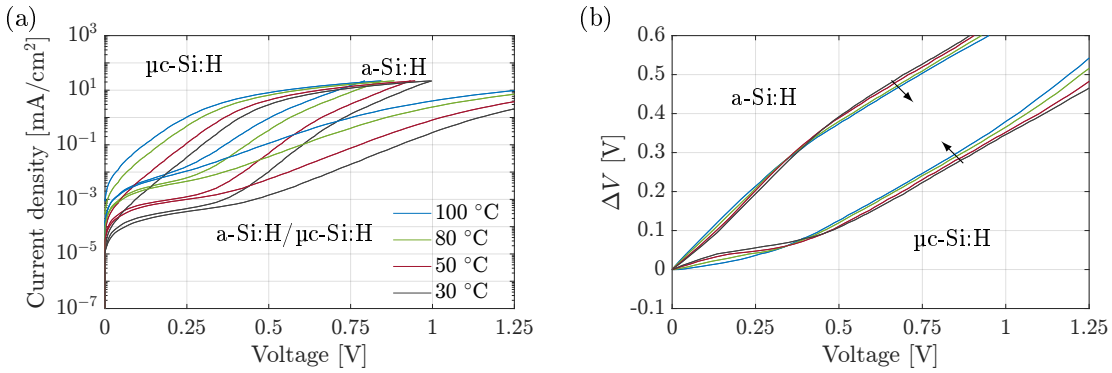

Figure 4.20: (a) The addition of dark JV curves of te 3t a-Si:H and µc-Si:H subcells, with an intrinsic layer thickness of 200 nm and 2500 nm respectively, by exponential interpolation of the current density. (b) Voltage drop ΔV over the top a-Si:H and bottom µc-Si:H subcells as a function of the tandem cell voltage. Selected temperatures are plotted for clarity, the direction of the arrows indicate increasing measurement temperature.

micromorph tandem cell in figure 4.14, the calculated tandem curves in figure 4.20 (a) shows current spreading in the low forward voltage region. It is clear that this effect indeed originates from the a-Si:H top cell. This effect, however, also changes the obtained voltage drop over the 3t a-Si:H and µc-Si:H subcells. It is therefore not possible to draw conclusions from this analysis.

4.2 Three-terminal device performance

The electrical performance of the fabricated devices, with a set of normal tandems and three-terminal solar cells, was determined with light current-voltage and external quantum efficiency measurements. Light JV measurements are used to compare the performance of the 3t micromorph tandem cells to the normal tandem cells, as well as to characterise the individual subcells and their parameters. The EQE curves were used to find the level of current-matching between the subcells, since the solar simulator for *JV* measurements has some spectral mismatch with AM 1.5. On top of that it also prevents problems with accurately defining the active solar cell area and possibly current collection through conductive layers other than the back contact [20]. A closely current-matched three-terminal tandem cell was chosen to demonstrate the operating conditions of a tandem cell. The thickness of the absorber layers were 200 nm for the intrinsic amorphous silicon and 2500 nm for the intrinsic microcrystalline silicon layers, respectively.

4.2.1 Light JV measurements

Light current-voltage measurements at standard test conditions are performed to find the external parameters of the normal tandem and three-terminal cells. Figure 4.21 shows the performance difference between a normal and a three-terminal solar cell with the same deposition parameters.

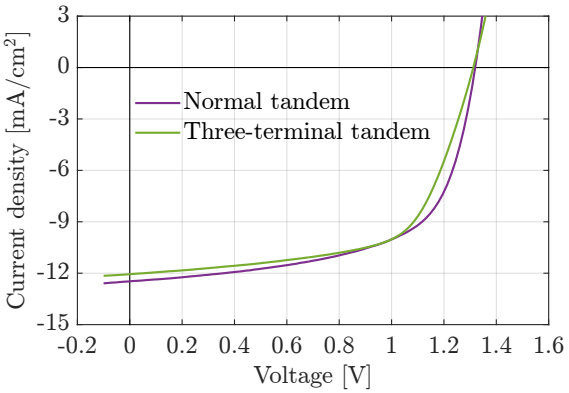

Figure 4.21: Light *JV* measurements of a closely matched three-terminal solar cell in comparison with normal tandem cell with the same deposition parameters.

Table 4.1: The photovoltaic performance at STC of the normal tandem and three-terminal solar cells. Standard deviations are included over the 15 equal solar cells of each type on the substrate. Note that the given efficiencies are the initial values.

Cell type	V_{oc} [mV]	J_{sc} [mA/cm^2]	FF	Effi. [%]	R_s [Ω·cm^2]	R_{sh} [Ω·cm^2]
Normal	1315 ± 4	12.3 ± 0.4	59.1 ± 2.3	9.60 ± 0.59	10.4 ± 0.9	860 ± 122
3-Terminal	1290 ± 28	11.3 ± 0.6	61.6 ± 1.3	8.99 ± 0.72	19.6 ± 2.9	922 ± 89

One important point on the *JV* curve, the open-circuit voltage V_{oc}, shows that there is only a very small loss of V_{oc} by introducing the middle contact. However, in the voltage region close to V_{oc} the curve shows a more shallow slope, indicating a slight increase of

series resistance. Table 4.1 gives an overview of the external parameters for the normal tandem and three-terminal cells. The largest difference between the cells can indeed be found in the series resistance R_s, where the middle contact has increased the value with an average of $9.20\,\Omega\,cm^2$. There is also a small decrease in J_{sc} for the three-terminal device, since this structure is bottom cell limited as will be shown with EQE measurements. Removing the middle AZO layer from the structure will change the cell to top cell limited which ultimately increases the J_{sc} by allowing more current collection in the top cell.

Overall, the three-terminal cell shows no record-breaking efficiency with $8.99 \pm 0.72\%$, but the electrical performance is comparable to the normal tandem cell. Note that the intrinsic layer thickness is optimised for current-matching of the three-terminal devices. A thicker a-Si:H top cell would lead to higher efficiencies for the normal tandem cells, but that is not the purpose of this study. In comparison, a record initial efficiency of 14.8% and a stabilised efficiency of 12.5% for a monolithic micromorph tandem cell was achieved by H. Tan *et al.* in 2015 [60]. The efficiency values in table (4.1) are initial values, taken before degradation of the a-Si:H top cell by the Staebler-Wronski effect.

The 3t a-Si:H top subcell and µc-Si:H bottom subcell were characterised individually through the middle AZO contact. The obtained fill factor for both subcell curves was substantially lower than expected. Looking at the solid lines in figure 4.22, one can observe an increased series resistance for both subcells, indicated by the shallower slope of the curves in the higher voltage region close to V_{oc}. Table 4.2 shows a comparison between the 3t subcells and the sj devices with the same deposition parameters.

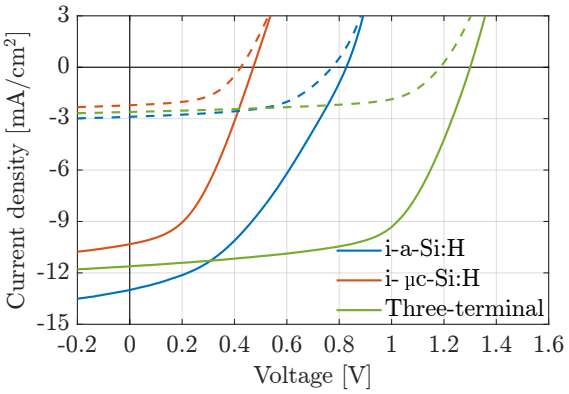

Figure 4.22: Light JV measurements of a closely matched three-terminal solar cell with separate curves measured through the intermediate contact. Solid lines represent AM1.5 light intensity, dashed lines are measured through a neutral density filter.

For the 3t a-Si:H top subcell, both the series resistance (R_s) and the shunt resistance (R_{sh}) are affected by measuring the cell through the middle contact. R_s is increased by lateral resistance of the AZO middle contact itself, since the current has to be collected perpendicular to the device flow direction. The sheet resistance of the layer is $46.2\,\Omega/\square$, which was determined with a four-point probe measurement. Together with the middle contact geometry shown in figure 3.7, the lateral resistance of the entire contact is estimated to be $42.5\,\Omega\,cm^2$. This follows from the 4 mm by 4 mm square cell area and the 1 mm wide by 3 mm long current path to the metal dot of the middle contact. It results in a value of 4 times the sheet resistance, divided by the area of the solar cell. A small correction has to be made since the total current will not have to travel through the en-

Table 4.2: The photovoltaic performance at STC of the three-terminal subcells compared to sj cells with the same deposition parameters. The intrinsic layer thicknesses are 200 nm for the a-Si:H and 2500 nm for the µc-Si:H cells. Standard deviations are included over the equal solar cells of each type on the substrate. Note that the given efficiencies are the initial values and that the values in red are not accurately describing the light JV characteristics of the individual three-terminal subcells.

Cell type	V_{oc} [mV]	J_{sc} [mA/cm^2]	FF	Effi. [%]	R_s [Ω·cm^2]	R_{sh} [Ω·cm^2]
3T i-a-Si:H	830 ± 17	11.6 ± 0.5	39.4 ± 1.8	3.79 ± 0.42	34.3 ± 6.8	265 ± 46
SJ i-a-Si:H	854 ± 5	12.7 ± 0.5	63.7 ± 3.1	6.88 ± 0.61	5.5 ± 0.7	713 ± 111
3T i-µc-Si:H	475 ± 6	9.30 ± 0.4	45.0 ± 4.0	1.97 ± 0.20	22.7 ± 2.6	354 ± 70
SJ i-µc-Si:H	504 ± 5	19.9 ± 1.2	64.1 ± 0.7	6.40 ± 0.40	3.3 ± 0.3	285 ± 20

tire contact, but only from the point where it is collected to the metal dot of the middle contact. The contribution to the resistance of the square 4 mm by 4 mm area is therefore assumed to be halved. This results in a final estimated value for the added series resistance of 37.2 Ω cm^2. The measured value for the series resistance of the a-Si:H subcell, derived from the slope of the JV curve close to the V_{oc}, has increased with 28.8 ± 6.8 Ω cm^2. This is in the same order of magnitude and comparable to the estimated value for the series resistance added by the middle AZO contact.

The R_{sh} of the 3t a-Si:H top subcell is decreased, which indicates that the light-generated current can follow alternative paths more easy. One possible explanation to this is that by forcing the current through the high resistive middle contact and out of the cell structure, it could find shunts between the n-a-Si:H layer and the front TCO closer to the edges of the substrate. Near the edges of the substrate there is a higher chance for shunts caused by a more inhomogeneous deposition quality [31]. On top of that, damage could be inflicted to the a-Si:H top cell by sputtering the middle AZO contact on to the tunnel recombination layer. This might also be the reason why for the 3t µc-Si:H bottom subcell the increase in series resistance is substantial, whereas the drop in shunt resistance is not observed. Both an increase in series resistance and a decrease in shunt resistance ultimately influence the maximum power point operation, which results in a lower fill factor and efficiency.

By reducing the light-generated current, the effect of series resistance on the operation of the solar cell and particularly the fill factor can be reduced, since the added resistance losses of the AZO contact will be lower. On the other hand, the effect of the decreased shunt resistance of the 3t a-Si:H top subcell on the JV characteristic will be moderately stronger for lower light-generated current, since the leakage current caused by shunts is subtracted from the light-generated current. The dashed lines in figure 4.22 represent measurements with reduced light intensity through a neutral density filter. The fill factor for the top cell was increased from 39.4 to 55.5, for the bottom cell it increased from 45.0 to 53.9. This indicates that the added series resistance significantly affects the obtained JV measurement through the middle AZO contact. The external parameters obtained from these measurements, except for V_{oc} and J_{sc}, are therefore not accurately describing the light current-voltage characteristics of the individual three-terminal subcells.

When designing the three-terminal device structure and determining the required thickness for the middle contact, the purpose was only to collect current through this contact

in the external quantum efficiency setup. Collection of a light-generated current at STC conditions would require a much thicker contact than the 200 nm in this design, in the order of 5 µm. This would, however, make it more complicated to fabricate a current-matched three-terminal cell [28]. Furthermore the shape of the middle contact can be improved by widening and/or shortening the current path towards the metallic dot, as this contributes most to the series resistance. A shorter path is favourable since a wider path would increase the active cell area even more than the design used in this study.

4.2.2 External Quantum Efficiency

The middle contact allowed for separate characterisation of the top and bottom subcell of the tandem structure. This way the subcells could be measured at short-circuit conditions without applying any bias voltage or bias illumination to saturate the non-measured subcell. Figure 4.23 (a) shows the EQE curves for the top and bottom subcell, including the sum that represents the overall EQE for the three-terminal structure. To assess the effect of the middle contact, figure 4.23 (b) shows the EQE for a normal tandem cell with the same deposition parameters, deposited on the same substrate. The subcells of the normal tandem device were measured by saturating the non-measured subcell with a high intensity bias illumination and by applying the approximate open-circuit voltage of the non-measured subcell. This method is regularly used to characterise multi-junction solar cells under short-circuit conditions [42, 45].

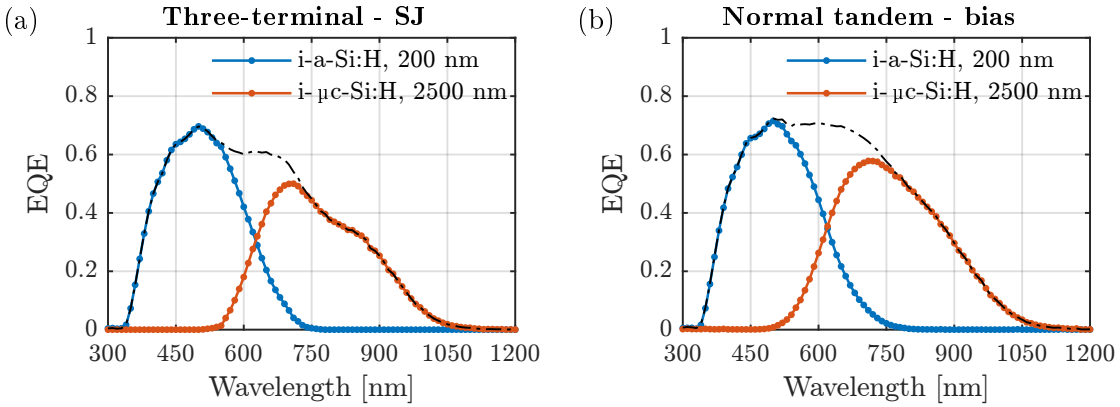

Cell type	a-Si:H top	µc-Si:H bottom	Summed
(a) Three-terminal - SJ	9.66 mA cm^{-2}	9.35 mA cm^{-2}	19.01 mA cm^{-2}
(b) Normal tandem - bias	9.57 mA cm^{-2}	11.35 mA cm^{-2}	20.92 mA cm^{-2}

Figure 4.23: EQE measurement of (a) a closely matched three-terminal solar cell, measured as sj cells through the intermediate contact without bias illumination or bias voltage and of (b) a normal tandem solar cell deposited on the same substrate as the closely matched three-terminal cell, measured as tandem cell with aid of bias illumination and bias voltage.

Looking at the dashed black line in figure 4.23 (a), which represents the sum of the top and bottom subcell curves, there is some decrease in EQE visible for the three-terminal cell when compared to the EQE of the normal tandem cell shown in figure 4.23 (b). The total short-circuit current density of the bottom cell is decreased with 2.00 mA cm^{-2}, compared to the normal tandem cell. The wavelength range where this current is lost reaches from about 500 nm to 900 nm. The loss of current can be attributed to the intermediate AZO

layer, as this is the only difference between the two cells. Light can either be reflected back to the top cell or be absorbed in the AZO layer. Both effects result in a decreased bottom cell EQE. Reflection of light would, however, also result in an increased top cell EQE and this is only marginally visible with 9.66 mA cm^{-2} for the three-terminal top cell and 9.57 mA cm^{-2} for the normal tandem top cell. Optical simulations with ASA and GENPRO4 reveals the absorption region of the middle contact AZO layer, see figure 4.24, which starts from approximately 650 nm. The simulation of the current-matched three-terminal structure demonstrates that the middle contact reflects light towards the a-Si:H top cell and absorbs light in the red to IR wavelength region. This results in an increased top cell absorption, although the i-µc-Si:H absorber layer should be more than twice as thick than the normal tandem cell in order to be current-matched with the top cell.

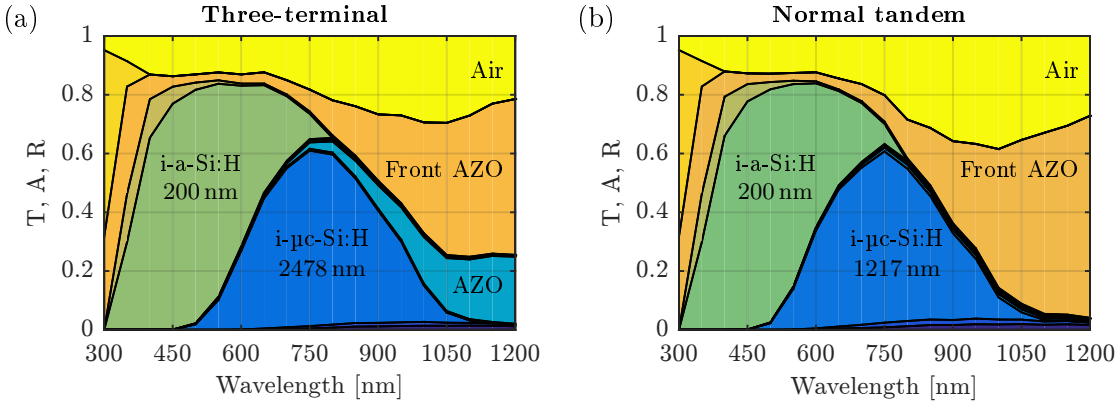

Figure 4.24: Optical simulation of transmittance (T), absorptance (A) and reflectance (R) versus wavelength of a three-terminal (a) and a normal tandem cell (b) with ASA and GENPRO4. Intrinsic layers of both cells are current-matched, with 11.87 mA cm^{-2} for the normal tandem cell and 12.46 mA cm^{-2} for the 3t tandem cell. The middle AZO layer absorbs photons from about 650 nm and increases the top cell absorption with 0.59 mA cm^{-2}.

The three-terminal cell EQE curves in figure 4.23 (a) are measured in dark conditions, with a low intensity probing light source. Voltage losses through series resistance of the middle AZO contact are therefore negligibly small as the highest current through the cell during the measurement is in the order of $1 \cdot 10^{-2}$ mA cm^{-2}. In order to distinguish between optical losses of the middle AZO contact and a possible measurement error by applying the bias illumination and bias voltage, the three-terminal cell was also measured with the same bias illumination and bias voltage conditions that where used to measure the normal tandem cell. These results are shown in figure 4.25 (b).

It is clear that the measurement method with bias illumination and bias voltage influences the spectral response of the top cell and to a minor extent also the bottom cell. Both three-terminal subcells in figure 4.25 (b) clearly show an increased EQE compared to the subcells shown in figure 4.25 (a). The different outcome of directly measuring the subcells through the middle AZO contact and measuring the three-terminal cell as a tandem structure is most probably caused by applying a bias voltage that was not accurate enough to put the measured subcell in short-circuit conditions. As discussed in section 2.3, the electric field distribution in the solar cell is affected by both applied voltage and bias illumination. The EQE must be measured at 0 V applied voltage and 1 sun illumination, otherwise the conversion from EQE to J_{sc} is invalid and the measurement should be referred to as apparent quantum efficiency (AQE) [44]. Often the 1 sun light intensity

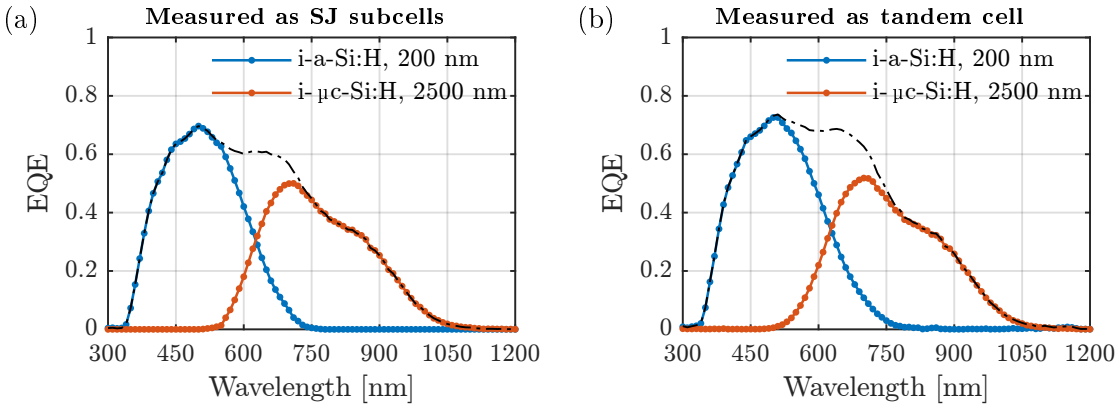

Cell type	a-Si:H top	µc-Si:H bottom	Summed
(a) Three-terminal - SJ	9.66 mA cm^{-2}	9.35 mA cm^{-2}	19.01 mA cm^{-2}
(b) Three-terminal - bias	10.03 mA cm^{-2}	9.48 mA cm^{-2}	19.51 mA cm^{-2}

Figure 4.25: EQE measurement of a closely matched three-terminal solar cell, measured as (a) sj subcells through the intermediate contact without bias illumination or bias voltage and (b) as tandem cell with aid of bias illumination and bias voltage. Note that figure (a) is a copy of figure 4.23 (a) for comparison.

requirement is relaxed, since the error that results from measuring at low light intensity compared to maximum power point operation is negligible [42]. In order to evaluate if the applied voltage could have caused the increased EQE of both subcells, a series of measurements was performed applying a range of different bias voltages across the 3t tandem cells' front and back contact. This bias range is chosen around the V_{oc} of the non-measured subcell, taking both lower and higher values.

Table 4.3: Applied bias voltage range to the 3t tandem cell and obtained short-circuit current densities for both top and bottom subcell measurements. For comparison, the obtained short-circuit current densities of the EQE measurements through the middle AZO contact are included.

Applied bias voltage	a-Si:H top
0.30 V	10.2 mA cm^{-2}
0.40 V	10.1 mA cm^{-2}
0.50 V	10.0 mA cm^{-2}
0.60 V	9.91 mA cm^{-2}
0.70 V	9.77 mA cm^{-2}
SJ subcell - no bias	9.66 mA cm^{-2}

Applied bias voltage	µc-Si:H bottom
0.70 V	9.80 mA cm^{-2}
0.80 V	9.66 mA cm^{-2}
0.90 V	9.48 mA cm^{-2}
1.0 V	9.20 mA cm^{-2}
1.1 V	8.49 mA cm^{-2}
SJ subcell - no bias	9.35 mA cm^{-2}

Figure 4.26 shows that increasing the applied voltage will decrease the spectral response of the measured solar cell, which can be explained by the internal electric field that is weakened. As described in section (2.3.1), the subcell that absorbs the bias illumination will operate at a forward bias that is approximately equal to its open-circuit voltage. Without applying any bias voltage, i.e. the measurement setup applies 0.0 V at the solar cell terminals, the measured subcell will operate at a reverse bias equal to the forward bias generated in the saturated (non-measured) subcell. The applied voltage should therefore

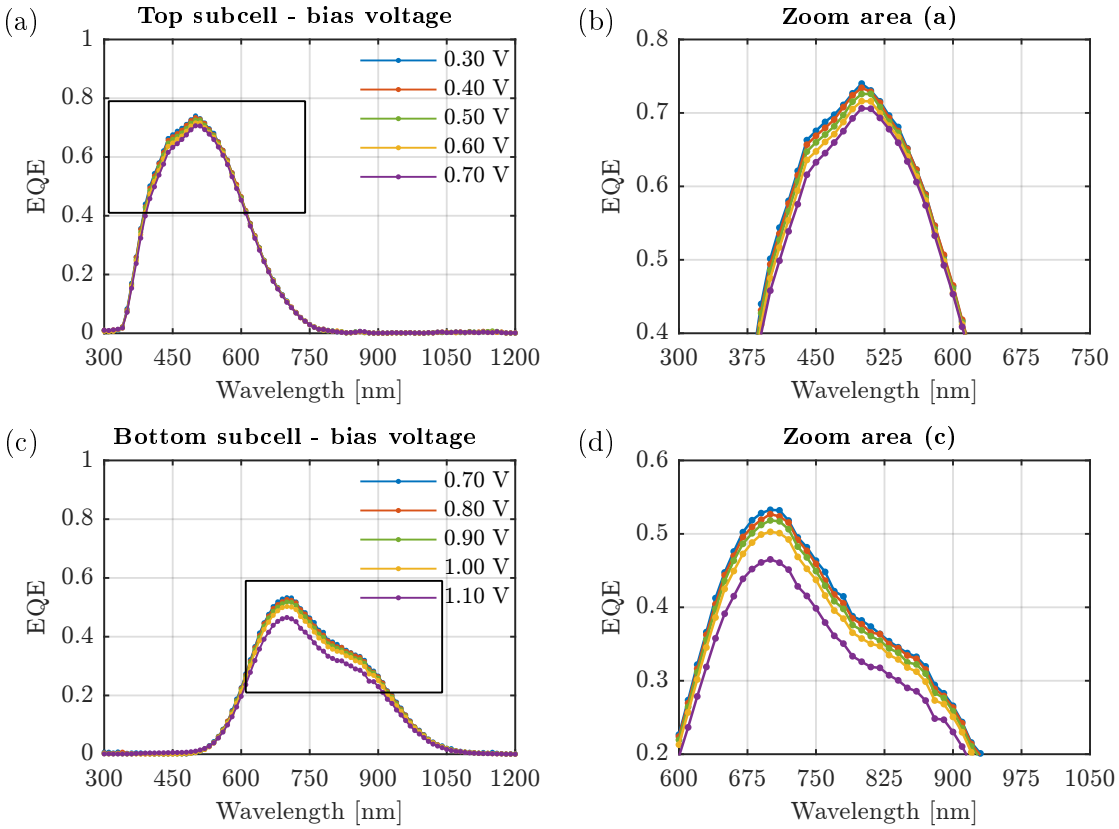

Figure 4.26: EQE measurements with varying bias voltage of (a) the 3t a-Si:H subcell with zoom area in figure (b), and (c) the 3t µc-Si:H subcell with zoom area in figure (d).

be equal to this forward bias in order to measure the subcell of interest at short-circuit conditions.

Given the open-circuit voltage of the 3t µc-Si:H bottom subcell is approximately 0.47 V, applying this voltage should in theory give the same EQE curve for the 3t a-Si:H top subcell as the one found by measuring through the middle AZO contact without bias voltage and illumination in figure 4.23 (a). Table 4.3, however, clearly shows that applying 0.70 V still results in a J_{sc} than what was found through the middle AZO contact, with 9.77 mA cm^{-2} at a bias voltage of 0.70 V compared to 9.66 mA cm^{-2} through the middle AZO contact without bias voltage.

The open-circuit voltage of the 3t a-Si:H subcell is approximately 0.83 V. Applying this voltage should in theory give the same EQE curve for the 3t µc-Si:H bottom subcell as the one found by measuring through the middle AZO contact without bias voltage and illumination in figure 4.23 (a). Table 4.3, however, clearly shows that this voltage should instead be between 0.90 V and 1.0 V.

We can conclude that the voltage distribution between the subcells of a tandem device during EQE characterisation is complicated. It has been demonstrated that the measurement method that includes bias illumination and bias voltage can not exactly reproduce the true EQE curve of the single junction subcells by applying the V_{oc} of the non-measured subcell.

5 | Conclusions and Recommendations

The results and discussions will be summarised and conclusions will be drawn for each separate section. The recommendations section will be divided into recommendations related to the performed experiments, the methods used and to future research.

5.1 Dark JV

5.1.1 Amorphous silicon

The three-terminal a-Si:H top subcell with an intrinsic layer thickness of 200 nm shows a lower mobility gap energy of 1.62 ± 0.02 eV compared to 1.70 ± 0.01 eV for a single-junction cell from the same deposition run. It is likely that thermal annealing of the i-a-Si:H layer occurred by the deposition of the middle AZO contact and bottom cell. If hydrogen is effused by thermal annealing of these further process steps, this would increase the defect density of the intrinsic a-Si:H layer, lowering its mobility gap. An increase in dark saturation current density and ideality factor further support this, since these indicate a higher recombination rate in the bulk intrinsic layer that could be caused by an increase in dangling bond density.

5.1.2 Microcrystalline silicon

The µc-Si:H subcell in the three-terminal tandem cell with an intrinsic layer thickness of 2500 nm demonstrates a dark saturation current density very close to the single junction cell from the same deposition run. A mobility energy gap of 1.08 ± 0.01 eV was determined, which is significantly lower than the value of 1.19 eV determined by Pieters *et al.* [22] and the obtained mobility gap of 1.17 ± 0.01 eV for the SJ µc-Si:H cell. The higher crystallinity of the three-terminal bottom subcell obtained with Raman spectroscopy, as compared with the SJ µc-Si:H cell, is not significant enough to explain the decreased mobility gap [51, 59].

5.1.3 Micromorph tandem

The three-terminal tandem cell shows a mobility gap energy of 1.77 ± 0.01 eV, which is close to the mobility gap of the SJ a-Si:H cell of 1.70 ± 0.01 eV. However, it is likely that this mobility gap belongs to the tunnel recombination junction, as it was determined in the high forward voltage region where the dark JV curve is suppressed by a non-ideal operation of the TRJ [39]. Pseudo JV curve measurements confirm that the ideality factor of a micromorph tandem cell in the second exponential region (see figure 2.4) is the sum of the subcell ideality factors in their respective exponential region. For this particular three-terminal cell the ideality factor determined from pseudo JV curves is 3.51 ± 0.03, the additions of the a-Si:H subcell (m =1.79 ± 0.02) and the µc-Si:H subcell (m =1.64 ± 0.01) yields a value of 3.53 ± 0.03. The same analysis did not hold for the dark JV measurements as the ideality factors were affected by series resistance in the higher forward voltage region of the subcells and an inefficiently operating TRJ for the tandem cell.

The temperature dependence of the applied voltage distribution over the subcells of a micromorph tandem cell was determined from the single-junction a-Si:H and µc-Si:H cell dark JV measurements. It has been demonstrated that the onset voltage for the µc-Si:H cell will decrease for increasing cell temperature. This observation indicates that the increase of dark current density as a function of temperature is higher for a-Si:H cells than for µc-Si:H cells in the low applied voltage region. It also revealed that the first exponential region on the dark JV curves of the three-terminal tandem cell was completely concealed by current spreading.

5.2 Three-terminal device performance

5.2.1 Light JV

The performance of the three-terminal tandem cells was compared to normal tandem cells on the same substrate. The initial conversion efficiency of $8.99 \pm 0.72\%$ is not record-breaking, but reasonably good for the purpose of this study. The most important observation was that only a small loss of V_{oc} (25 mV) was found after the introduction of the middle AZO contact. An increased series resistance was observed upon measuring the top and bottom cell through the middle contact. An estimated value for the added series resistance by lateral conduction through the middle contact resulted in $37.2\,\Omega\,cm^2$, which is very close to the observed increase in series resistance for the top a-Si:H subcell of $28.8 \pm 6.8\,\Omega\,cm^2$.

5.2.2 External Quantum Efficiency

Being measured in dark conditions without bias illumination, the effect of the added series resistance by the middle AZO contact was eliminated for the EQE measurements of the three-terminal top and bottom subcells. The obtained "true" EQE curves for the top and bottom subcells were compared with the curves obtained with the standard measurement method for multi-junction solar cells, which applies bias illumination and bias voltage. It has been demonstrated that applied voltage can easily introduce measurement artifacts, i.e. the spectral response of the measured subcell is affected by not being measured under short-circuit conditions, which ultimately changes the internal electric field and thereby the collection efficiency of charge carriers. It therefore remains an interesting research topic to monitor the voltage at the TRJ for various measurements, as the voltage distribution between the subcells clearly affects the tandem cell performance.

5.3 Recommendations

Regarding the performed experiments, the three-terminal device structure should be improved by eliminating most of the current spreading and series resistance effects in order to obtain more reliable and easily comparable dark JV curves. The n-layer of the a-Si:H top subcell could possibly be removed with reactive ion etching prior to deposition of the bottom cell. The design of the middle contact should also be adjusted to lower the added series resistance for measurements through the middle AZO contact substantially. This can either be accomplished by increasing the layer thickness or by changing the

aspect ratio of the current path to the metal dot of the middle contact. If it is possible to obtain dark JV curves for each of the subcells and tandem cell unaffected by series resistance or current spreading, the voltage drop across the TRJ could for instance be calculated. This can be accomplished by including the tandem cell dark JV curves to the voltage distribution calculation, which could potentially be a good method to determine the performance of the TRJ.

The lower mobility gap that was observed for both three-terminal subcells compared to the single-junction cells from the same deposition run requires further investigation. When the obtained values in this work are proven to be correct, it would potentially be a topic for studying the effect of bottom cell deposition on structural changes in the top a-Si:H cell. An attempt could be made to fabricate three-terminal tandem cells with reduced current spreading and series resistance. Another option is to obtain the mobility gap from series-resistance-free variable intensity measurements at different temperatures on the devices discussed in this study. However, the temperature range would be limited to 15 °C to 55 °C by limitations of the light JV measurement setup.

Correctly characterising the EQE curve for subcells of a multi-junction solar cell still proofs to be complicated. Further investigation on the effect of applied voltage on the three-terminal subcells is worthwhile to gain knowledge on applying the correct bias voltage to measure each individual cell under short-circuit conditions. Adjustments to the EQE measurement setup are required to actually monitor the voltage at the tunnel recombination junction (TRJ) when a measurement is performed. These adjustments include a software extension to the `LabVIEW` program that controls the setup. The voltage at the TRJ of the tandem solar cell should be measured as a DC signal with respect to either the front or back contact, since every light contribution to the change in voltage should be accounted for. This could ultimately be a good method to adapt the bias illumination intensity and applied bias voltage and check whether the measured subcell is under short-circuit conditions for the entire spectral range. EQE curves from normal tandem and three-terminal cells measured at the same bias illumination and bias voltage settings should then be compared, which could potentially improve the characterisation quality of multi-junction cells.

Lastly it might be interesting to model the current spreading effect more accurately with a square back contact on a rectangular substrate. This way a dark JV measurement curve that is influenced by this effect can be corrected to obtain the JV curve free from current spreading. This could particularly be interesting for multi-junction structures, where it is difficult to remove n-type layers located between subcells.

Bibliography

[1] United Nations. Adoption of the Paris Agreement. 21932(December):32, 2015.

[2] H. H. A. GmbH. Application of Nano- technologies in the Energy Sector. page 88, 2008.

[3] ITER. What is Fusion, 2016.

[4] National Renewable Energy Laboratory. Solar Spectral Irradiance: Air Mass 1.5, 2009.

[5] J. R. Hook and H. E. Hall. *Solid State Physics*. John Wiley & Sons, Chichester, second edition, 1991.

[6] A. H. M. Smets, K. Jäger, O. Isabella, R. A. C. M. M. van Swaaij, and M. Zeman. *Solar Energy*. UIT Cambridge Ltd, Cambridge, first edition, 2016.

[7] A. E. Becquerel. Recherches sur les effets de la radiation chimique de la lumiere solaire au moyen des courants electriques. *Comptes Rendus de L'Academie des Sciences*, 9:145–149, 1839.

[8] W. Shockley and H. J. Queisser. Detailed Balance Limit of Efficiency of p-n Junction Solar Cells. *Journal of Applied Physics*, 32(3):510, 1961.

[9] L. M. Peter. Towards sustainable photovoltaics: the search for new materials. *Philosophical transactions. Series A, Mathematical, physical, and engineering sciences*, 369(1942):1840–1856, 2011.

[10] E. A. G. Hamers, M. N. van den Donker, B. Stannowski, R. Schlatmann, and G. J. Jongerden. Helianthos: Roll-to-roll deposition of flexible solar cell modules. *Plasma Processes and Polymers*, 4 (3):275–281, 2007.

[11] L. Han, F. F. Abdi, R. van de Krol, R. Liu, Z. Huang, H. J. Lewerenz, B. Dam, M. Zeman, and A. H. M. Smets. Efficient Water-Splitting Device Based on a Bismuth Vanadate Photoanode and Thin-Film Silicon Solar Cells. *ChemSusChem*, 7(10):2832–2838, 2014.

[12] A. Shah. *Thin-Film Silicon Solar Cells*. EPFL Press, Lausanne, first edition, 2010.

[13] A. H. M. Smets, W. M. M. Kessels, and M. C. M. van de Sanden. Vacancies and voids in hydrogenated amorphous silicon. *Applied Physics Letters*, 82(10):1547–1549, 2003.

[14] M. Zeman. Introduction to Photovoltaic Solar Energy. *Solar Cells, collegemateriaal*, 2003.

[15] R. Kind, R. A. C. M. M. van Swaaij, F. A. Rubinelli, S. Solntsev, and M. Zeman. Thermal ideality factor of hydrogenated amorphous silicon p-i-n solar cells. *Journal of Applied Physics*, 110(10), 2011.

[16] A. Sturiale and F. A. Rubinelli. Evidences of the defect pool model in the dark current-voltage characteristics of hydrogenated amorphous silicon based p-i-n devices. *Thin Solid Films*, 516(21): 7708–7714, 2008.

[17] Y. Tawada, K. Tsuge, M. Kondo, H. Okamoto, and Y. Hamakawa. Properties and structure of a-SiC:H for high-efficiency a-Si solar cell. *Journal of Applied Physics*, 53(7):5273–5281, 1982.

[18] D. L. Staebler and C. R. Wronski. Reversible conductivity changes in discharge-produced amorphous Si. *Applied Physics Letters*, 31(4):292–294, 1977.

[19] J. Meier, S. Dubail, R. Flückiger, D. Fischer, H. Keppner, and A. Shah. Intrisnic Microcrystalline Silicon, A promising new thin film solar cell material. *1st WCPEC*, pages 409–412, 1994.

[20] G. Yang. *High-efficient n-i-p thin-film silicon solar cells Guangtao Yang*. Phd. thesis, Delft University of Technology, 2015.

[21] M. Python, O. Madani, D. Dominé, F. Meillaud, E. Vallat-Sauvain, and C. Ballif. Influence of the substrate geometrical parameters on microcrystalline silicon growth for thin-film solar cells. *Solar Energy Materials and Solar Cells*, 93(10):1714–1720, 2009.

[22] B. E. Pieters, H. Stiebig, M. Zeman, and R. A. C. M. M. van Swaaij. Determination of the mobility gap of intrinsic μc-Si:H in p-i-n solar cells. *Journal of Applied Physics*, 105(4):1–10, 2009.

[23] D. Fischer, S. Dubail, J. Selvan, N. Vaucher, R. Platz, C. Hof, U. Kroll, J. Meier, P. Torres, H. Kepp-

ner, N. Wyrsch, M. Goetz, A. Shah, and K.-D. Ufert. The "micromorph" solar cell: extending a-Si:H technology towards thin film crystalline silicon. *Conference Record of the Twenty Fifth IEEE Photovoltaic Specialists Conference - 1996*, pages 1053–1056, 1996.

[24] Y. S. Lin, S. Y. Lien, C. C. Wang, C. H. Hsu, C. H. Yang, A. Nautiyal, D. S. Wuu, P. Tsai, and S. J. Lee. Optimization of recombination layer in the tunnel junction of amorphous silicon thin-film tandem solar cells. *International Journal of Photoenergy*, 2011, 2011.

[25] J. K. Rath, F. A. Rubinelli, and R. E. I. Schropp. Effect of oxide treatment at the microcrystalline tunnel junction of a-Si : H / a-Si : H tandem cells. 269:1129–1133, 2000.

[26] L. Feitknecht. Evaluations on current-matching of multi-junction photovoltaics under outdoor conditions. *Energy Procedia*, 15(2011):396–402, 2012.

[27] M. Y. Feteha and G. M. Eldallal. The effects of temperature and light concentration on the GaInP/GaAs multijunction solar cell's performance. *Renewable Energy*, 28(7):1097–1104, 2003.

[28] J. Holovský, M. Bonnet-Eymard, M. Boccard, M. Despeisse, and C. Ballif. Variable light biasing method to measure component I-V characteristics of multi-junction solar cells. *Solar Energy Materials and Solar Cells*, 103:128–133, 2012.

[29] R. A. C. M. M. van Swaaij, R. Kind, and M. Zeman. Recombination efficacy in a-Si:H p-i-n devices. *Journal of Non-Crystalline Solids*, 358(17):2190–2193, 2012.

[30] P. Singh and N. Ravindra. Temperature dependence of solar cell performance - an analysis. *Solar Energy Materials and Solar Cells*, 101:36–45, 2012.

[31] J. A. Willemen. *Modelling of Amorphous Silicon Single- and Multi-Junction Solar Cells*. Phd. thesis, Delft Univeristy of Technology, 1998.

[32] K. Lips and W. Fuhs. Transport and recombination in amorphous p-i-n-type solar cells studied by electrically detected magnetic resonance. *Journal of Applied Physics*, 74(6):3993–3999, 1993.

[33] A. Cuevas. The Recombination Parameter J0. *Energy Procedia*, 55:53–62, 2014.

[34] A. Luque and S. S. Hegedus. *Handbook of Photovoltaic Science and Engineering*. John Wiley & Sons, Chichester, second edition, 2011.

[35] D. A. Neamen. *Semiconductor Physics and Devices: Basic Principles*. Mc Graw-Hill, New York, fourth edition, 2012.

[36] C. van Berkel, M. J. Powell, A. R. Franklin, and I. D. French. Quality factor in a-Si:H nip and pin diodes. *Journal of Applied Physics*, 73(10):5264–5268, 1993.

[37] M. A. Kroon and R. A. C. M. M. van Swaaij. Spatial effects on ideality factor of amorphous silicon pin diodes. *Journal of Applied Physics*, 90(2):994–1000, 2001.

[38] J. Deng and C. R. Wronski. Carrier recombination and differential diode quality factors in the dark forward bias current-voltage characteristics of a-Si:H solar cells. *Journal of Applied Physics*, 98(2), 2005.

[39] A. Sturiale, H. T. Li, J. K. Rath, R. E. I. Schropp, and F. A. Rubinelli. Exploring dark current voltage characteristics of micromorph silicon tandem cells with computer simulations. *Journal of Applied Physics*, 106(1):1–10, 2009.

[40] F. A. Rubinelli, H. Liu, and C. R. Wronski. A comparison of the hydrogenated amorphous Si schottky barrier and the hydrogenated amorphous Si p-i-n dark forward-bias current density-Voltage characteristics. *Philosophical Magazine Part B*, 74(4):407 – 426, 1996.

[41] J. Merten, J. M. Asensi, C. Voz, A. V. Shah, R. Platz, and J. Andreu. Improved equivalent circuit and analytical model for amorphous silicon solar cells and modules. *IEEE Transactions on Electron Devices*, 45(2):423–429, 1998.

[42] K. Emery. *Measurement and characterization of solar cells and modules*. John Wiley & Sons, Hoboken, second edition, 2011.

[43] S. S. Hegedus and R. Kaplan. Analysis of quantum efficiency and optical enhancement in amorphous Si p-i-n solar cells. *Progress in Photovoltaics: Research and Applications*, 10(4):257–269, 2002.

[44] S. S. Hegedus and W. N. Shafarman. Thin-film solar cells: Device measurements and analysis. *Progress in Photovoltaics: Research and Applications*, 12(2-3):155–176, 2004.

[45] C. J. Hibberd, F. Plyta, C. Monokroussos, M. Bliss, T. R. Betts, and R. Gottschalg. Voltage-dependent quantum efficiency measurements of amorphous silicon multi-junction mini-modules. *Solar Energy Materials and Solar Cells*, 95(1):123–126, 2011.

[46] K. Misiakos and F. A. Lindholm. Analytical and numerical modeling of amorphous silicon p-i-n solar cells. *Journal of Applied Physics*, 64(1):383, 1988.

[47] P. J. Kelly and R. D. Arnell. Magnetron sputtering: a review of recent developments and applications. *Vacuum*, 56(3):159–172, 2000.

[48] C. Smit, R. A. C. M. M. van Swaaij, H. Donker, A. M. H. N. Petit, W. M. M. Kessels, and M. C. M. van de Sanden. Determining the material structure of microcrystalline silicon from Raman spectra. *Journal of Applied Physics*, 94(5):3582–3588, 2003.

[49] Srs. About Lock-In Amplifiers. *Application Note*, (408):1–9, 2011.

[50] V. Jovanov, X. Xu, S. Shrestha, M. Schulte, J. Hüpkes, and D. Knipp. Predicting the interface morphologies of silicon films on arbitrary substrates: Application in solar cells. *ACS Applied Materials and Interfaces*, 5(15):7109–7116, 2013.

[51] D. Y. Kim, R. Santbergen, K. Jäger, M. Sever, J. Krč, M. Topič, S. Hänni, C. Zhang, A. Heidt, M. Meier, R. A. C. M. M. van Swaaij, and M. Zeman. Effect of substrate morphology slope distributions on light scattering, nc-Si:H film growth, and solar cell performance. *ACS Applied Materials and Interfaces*, 6(24):22061–22068, 2014.

[52] H. Askari, H. Fallah, M. Askari, and M. C. Mohmmadieyh. Electrical and optical properties of ITO thin films prepared by DC magnetron sputtering for low-emitting coatings. pages 1–8, 2014.

[53] M. Izzi, M. Tucci, L. Serenelli, P. Mangiapane, E. Salza, R. Chierchia, M. D. Noce, I. Usatii, E. Bobeico, L. Lancellotti, L. V. Mercaldo, and P. D. Veneri. TCO Optimization in Si Heterojunction Solar Cells on p-type Wafers with n-SiOx Emitter. *Energy Procedia*, 84:134–140, 2015.

[54] D. Dominé, J. Bailat, J. Steinhauser, A. Shah, and C. Ballif. Micromorph solar cell optimization using a ZnO layer as intermediate reflector. *Conference Record of the 2006 IEEE 4th World Conference on Photovoltaic Energy Conversion, WCPEC-4*, 2:1465–1468, 2007.

[55] S.-M. Park, T. Ikegami, and K. Ebihara. Growth of Transparent Conductive Al-Doped ZnO Thin Films and Device Applications. *Japanese Journal of Applied Physics*, 45(10B):8453–8456, 2006.

[56] R. Kind. *Dark Current Characteristics of Amorphous Silicon Solar Cells*. Msc thesis, Delft University of Technology, 2010.

[57] M. Legesse, M. Nolan, and G. Fagas. Revisiting the dependence of the optical and mobility gaps of hydrogenated amorphous silicon on hydrogen concentration. *Journal of Physical Chemistry C*, 117 (45):23956–23963, 2013.

[58] K. M. A. Rahman. Nanocrystalline Silicon Solar Cells Deposited via Pulsed PECVD at 150C Substrate Temperature. *Solar Cells*, 2010.

[59] B. E. Pieters, S. Schicho, and H. Stiebig. Characterization of the Mobility Gap in μc-Si:H Pin Devices. *MRS Proceedings*, 1066, 2011.

[60] H. Tan, E. Moulin, F. T. Si, J. W. Schüttauf, M. Stuckelberger, O. Isabella, F. J. Haug, C. Ballif, M. Zeman, and A. H. M. Smets. Highly transparent modulated surface textured front electrodes for high-efficiency multijunction thin-film silicon solar cells. *Progress in Photovoltaics: Research and Applications*, 23(8):949–963, 2015.

6 | Appendix

6.1 Dark JV

This part of the appendix will show the dark current-voltage figures including reverse bias characteristics for the single-junction cells, the three-terminal tandem cell and subcells measured through the middle AZO contact. The reverse bias characteristics are not further discussed in this study.

6.1.1 Single-junction cells

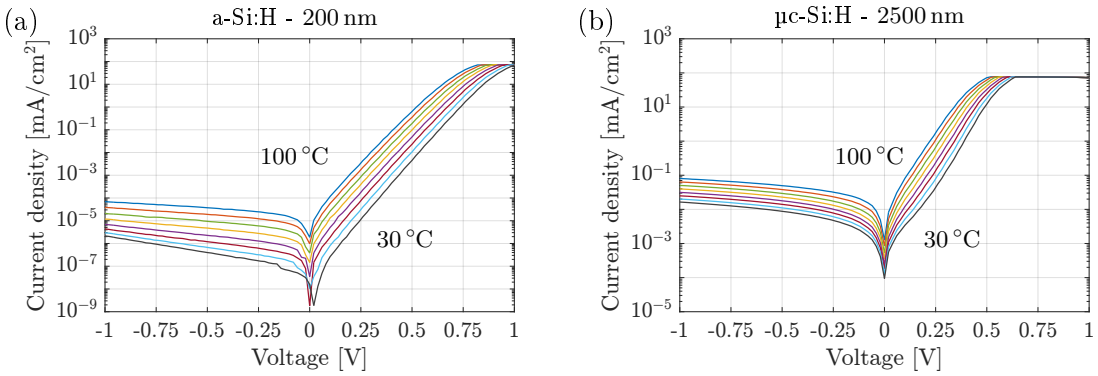

Figure 6.1: Dark current-voltage curves including reverse bias characteristics for (a) an a-Si:H and (b) a µc-Si:H single junction cell with intrinsic layer thicknesses of 200 nm and 2500 nm respectively, measured at temperatures ranging from 100 °C to 30 °C. Note that the y-axis ticks are different for both figures.

6.1.2 Three-terminal tandem and subcells

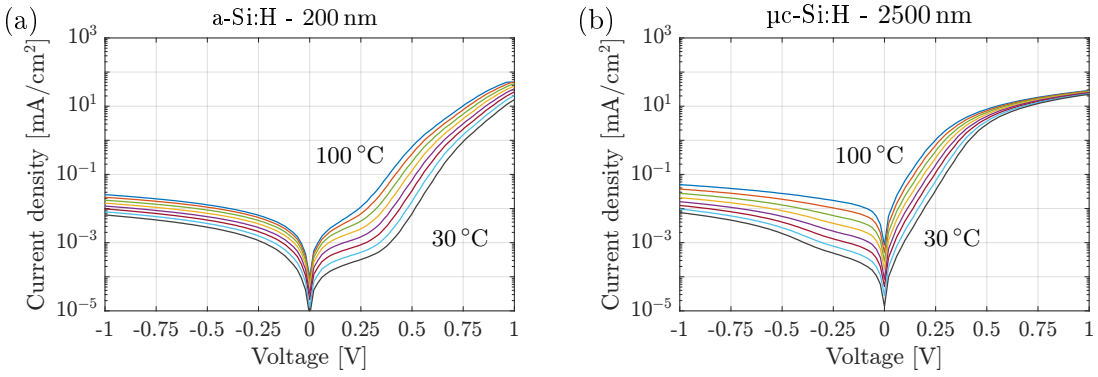

Figure 6.2: Dark current-voltage curves including reverse bias characteristics for (a) an a-Si:H and (b) a µc-Si:H three-terminal subcell with intrinsic layer thicknesses of 200 nm and 2500 nm respectively, measured at temperatures ranging from 100 °C to 30 °C.

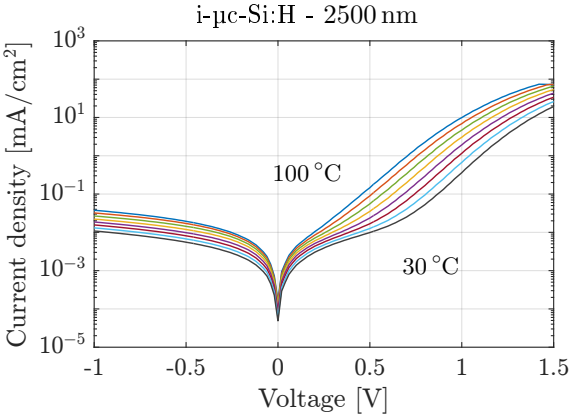

Figure 6.3: Dark current-voltage curves including reverse bias characteristics for the micromorph three-terminal tandem cell with varying, measured at temperatures ranging from 100 °C to 30 °C.

6.2 Standard deviation of Mobility energy gaps

The standard deviations of the mobility energy gaps are obtained by propagation of the dark *JV* measurement uncertainties. As explained in section (3.2.5), contributions to the measurement uncertainty are introduced by the temperature accuracy of ± 0.5 K, resulting in an error between 0.13% and 0.16% for the temperature range of 100 °C to 30 °C. Furthermore there are contribution of setting the voltage with an accuracy of 0.15% and reading the current with an accuracy better than 0.01%. The sum of squares of the measurement uncertainties was used to calculate the upper and lower bound voltage-dependent activation energy curves by a least-squares fitting method to equation (2.2.8), presented in figure 6.4. Note that the measurement uncertainty is increased on purpose for this figure to clearly show the different curves. After the standard deviations derived from

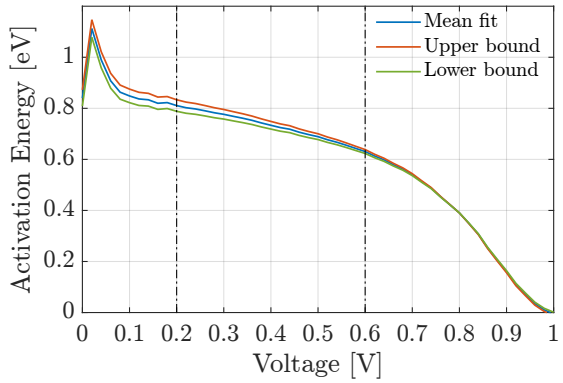

Figure 6.4: Mean, upper and lower bound fit to the dark *JV* measurement data for an a-Si:H single-junction solar cell.

the 95% confidence intervals were included to the obtained upper and lower bound data, each curve was fit to the analytic equation for the voltage-dependent activation energy as proposed by Pieters *et al.* (equation 2.2.10). The mobility energy gap values for the upper and lower bound curves were used to obtain the propagated standard deviation from the mobility gap value obtained from the measurement data (mean fit). Note that a similar

method was used to obtain the standard deviations to the ideality factors obtained from dark JV and pseudo JV curves.

6.3 Current spreading

The current spreading effect was modelled for a single-junction a-Si:H cell based on the ideality factors and dark saturation current densities obtained from the SJ a-Si:H cell with intrinsic layer thickness of 200 nm in figure 4.1. The cell was modelled as a circular contact dot with a radius of 2 mm as the centre of a circular shaped substrate with a radius of 12.5 mm. The n-layer below the metal contact has a thickness of 20 nm and a conductivity of $2 \cdot 10^{-2}\,\mathrm{S\,cm^{-1}}$. Section (2.2.2) describes the equations used for calculating the voltage drop ΔV over the n-layer and the resulting lateral current collection. Figure 6.5 shows the obtained JV curves for varying temperatures in comparison with the single diode curves with the same ideality factor and dark saturation current density based on equation (2.2.3).

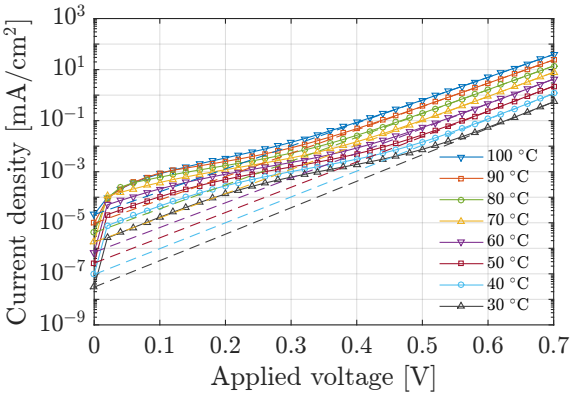

Figure 6.5: Dark current-voltage curves including reverse bias characteristics for the micromorph three-terminal tandem cell with varying, measured at temperatures ranging from 100 °C to 30 °C.

The modelled JV curves reveal the current spreading effect in the low forward voltage region, being more present for the lower temperature curves. Here the effect will be limited by the geometrics of the entire substrate. In order for the model to fit experimental data, the substrate and the location of the back contact will need to be modelled more accurate, which might be quite difficult for a rectangular shaped substrate and a square contact dot.

6.4 Pseudo JV

The pseudo JV curves obtained through variable intensity measurements for the single-junction a-Si:H and µc-Si:H cells and the normal tandem cell are shown in figure 6.6, together with the dark JV curves measured at 25 °C. There is a very good overlap between the dark JV and pseudo JV curves in the measured voltage region for the single-junction cells and the tandem without middle AZO contact. Even the effect of current spreading is clearly visible and overlapping in figure 6.6 (c). The ideality factors obtained from the pseudo and dark JV curves are very close for each of the cells.

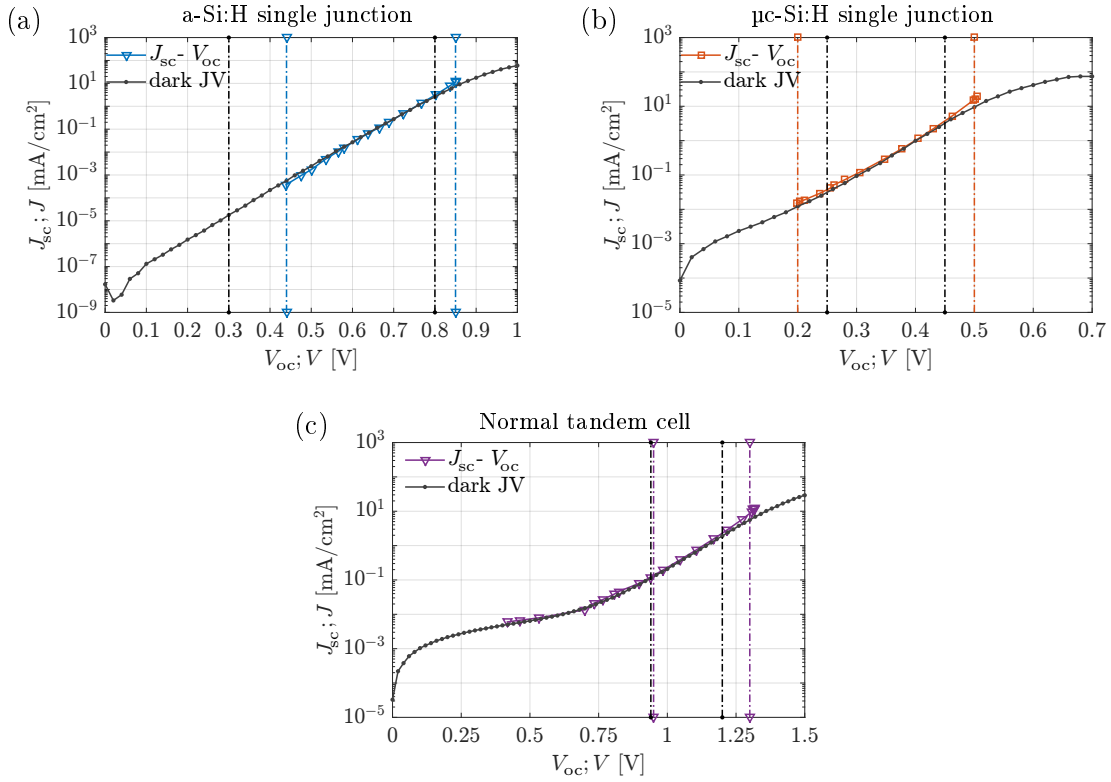

Figure 6.6: Pseudo JV curves compared to dark JV curves measured at $T = 25\,°C$ of (a) the a-Si:H SJ cell, (b) the µc-Si:H SJ cell and (c) the normal tandem cell. Least squares fits to the single diode equation between the vertical dashed lines for each curve resulted in an ideality factor of (a) 1.58 ± 0.01 and 1.63 ± 0.03, (b) 1.71 ± 0.02 and 1.67 ± 0.03 and (c) 3.31 ± 0.02 and 3.56 ± 0.07 for the pseudo JV curve and dark JV curve respectively.

6.5 List of figures

6.6 List of tables